ČESKÉ VYSOKÉ UČENÍ TECHNICKÉ V PRAZE

FAKULTA JADERNÁ A FYZIKÁLNĚ INŽENÝRSKÁ
KATEDRA FYZIKÁLNÍ ELEKTRONIKY

DIZERTAČNÍ PRÁCE

Large surface functionalization by laser-induced micro and nanostructures

Praha 2020   Ing. Petr Hauschwitz

Bibliografický záznam

Autor	Ing. Petr Hauschwitz, České vysoké učení technické v Praze, Fakulta jaderná a fyzikálně inženýrská, Katedra fyzikální elektroniky
Název práce	Velkoplošná funkcionalizace povrchů pomocí laserem vytvořených mikro a nanostruktur
Studijní program	Aplikace přírodních věd
Studijní obor	Fyzikální inženýrství
Školitel	Ing. Tomáš Mocek, Ph.D., Akademie věd České republiky, Fyzikální ústav, v.v.i., Centrum HiLASE
Školitel specialista	Ing. Petr Gavrilov, CSc., České vysoké učení technické v Praze, Fakulta jaderná a fyzikálně inženýrská, Katedra fyzikální elektroniky
Akademický rok	2020 – 2021
Počet stran	121
Klíčová slova	laser, mikroobrábění, nanostrukturování, velkoplošné obrábění, interferenční strukturování, SLM, superhydrofobicita, vakuové opracování

Bibliographic ent

Author	Ing. Petr Hauschwitz, Czech Technical University in Prague, Faculty of Nuclear Sciences and Physical Engineering, Department of Physical Electronics
Title	Large surface functionalization by laser-induced micro and nanostructures
Degree programme	Application of Natural Sciences
Field of study	Physical Engineering
Supervisor	Ing. Tomáš Mocek, Ph.D., Academy of Sciences of the Czech Republic, Institute of Physics of the Czech Academy of Sciences, HiLASE Centre
Supervisor specialist	Ing. Petr Gavrilov, CSc., Czech Technical University in Prague, Faculty of Nuclear Sciences and Physical Engineering, Department of Physical Electronics
Academic year	2020 – 2021
Number of pages	121
Keywords	laser, micromachining, nanostructuring, large scale processing, interference patterning, SLM, superhydrophobicity, vacuum processing

Abstrakt

Výrobě funkčních povrchů je v posledních letech věnována velká pozornost, zejména díky možnosti změnit povrchové vlastnosti nad rámec samotného materiálu. Lze tak dosáhnout například superhydrofobicity, antibakteriálních, ledofóbních, samočistících, antikorozních vlastností, či snížení tření u široké škály materiálů. Inspirovány přírodou jsou povrchy těchto materiálů často tvořeny kombinací mikro a nanostruktur. Pro výrobu takových struktur je vhodné laserové mikroobrábění umožňující tvorbu široké škály mikro a nanostruktur pro různé funkční povrchy. Procesní rychlosti při klasickém opracování jediným svazkem („bod po bodu") se však pohybují pouze v řádu minut na čtvereční centimetr, což omezuje průmyslové využití při opracování velkých ploch. K efektivnímu využití vysokého výkonu nové generace laserových systémů pro opracování s vysokou kvalitou v blízkosti prahu ablace je potřeba hledat nové procesní strategie. Tato práce obsahuje rešerši optimálních struktur vhodných pro výrobu funkčních povrchů, zejména pak superhydrofóbních, ledofóbních a antibakteriálních povrchů. Následně jsou diskutovány vhodné procesní strategie, kde je detailní pozornost věnována laserovému mikrotexturování. V následující kapitole jsou rozebrány nejslibnější metody pro rychlé opracování velkoplošných povrchů laserem, zahrnující polygonální skener, interferenční obrábění a několikasvazkové skenovací přístupy využívající DOE nebo SLM. Tyto znalosti jsou pak zúročeny v experimentální části pro vývoj technologie výroby funkčních mikro a nanostruktur, psané formou souboru komentovaných publikací v mezinárodních časopisech.

Abstract

Fabrication of functional surfaces has drawn a lot of attention in recent years since it allows to reach surface properties which go well beyond the properties of the bulk material. For instance, superhydrophobicity, anti-bacteria, anti-icing, self-cleaning, anti-corrosion or friction reduction properties have been demonstrated on a wide range of materials. Inspired by nature, functional performances often arise from hierarchical structures composed of a combination of micro and nanoscale features. Laser micromachining is a suitable method for fabrication of various micro and nanostructures providing a different kind of functionality to treated surfaces. However, the fabrication speeds of commonly used point to point approach - direct laser writing (DLW), is in a range of minutes per square centimetre, which limits the use of DLW for large-scale surfaces often required by industrial end-use. Moreover, a new generation of high-power laser system requires new processing strategies to effectively use the full laser potential for high-quality close-to-threshold processing ablation. In this work, a review of optimal topography for the fabrication of functional surfaces is given with a focus on superhydrophobic, anti-icing and anti-bacterial surfaces. Suitable fabrication methods are listed with a detail focus on laser surface microtexturing. In the next chapter, the most promising rapid large-scale techniques are depicted, including polygonal scanning systems, direct laser interference patterning and multi-beam scanning approaches using DOE or SLM plate. This know-how is applied for the development of processes for the fabrication of functional micro and nanostructures. Results are presented in the experimental section which is written in a form of scientific papers published in international journals.

Prohlášení

Potvrzuji, že podíl kandidáta Ing. Petra Hauschwitze na tvorbě publikací předkládaných v rámci jeho dizertační práce „Large surface functionalization by laser-induced micro and nanostructures" odpovídá podílu uvedenému v odstavci „Author contribution", který je uváděn před prezentací těchto publikací v kapitole 5.

....
Ing. Petr Hauschwitz

....
Radhakrishnan Jagdheesh, Dr.

....
Ing. Jan Brajer, Ph.D.

Sabri Alamri
Digital unterschrieben von Sabri Alamri
Datum: 2020.09.28 08:58:15 +02'00'
....
Sabri Alamri, Ph.D.

Tim Kunze
Digital unterschrieben von Tim Kunze
DN: c=DE, o=Fraunhofer, ou=IWS, ou=People, cn=Tim Kunze
Datum: 2020.09.29 17:38:36 +02'00'
....
Tim Kunze, Ph.D.

....
Ing. Martin Cimrman

....
Ing. Antonio Lucianetti, Dr.

....
Ing. Tomáš Mocek, Ph.D.

....
RNDr. Jaromír Kopeček, Ph.D.

....
Ing. Michael Písařík, Ph.D.

....
Bc. Dominika Jochcová

....
Ing. Jana Houdková

....
Bohumil Stoklasa, Ph.D.

....
RNDr. Hana Turčičová, CSc.

....
Danijela Rostohar, Dr.

....
Ing. Martin Smrž, Ph.D.

....
Ing. Jiří Mužík

....
Ing. Petr Jiříček

....
Ing. Martin Duda

....
Jiří Kuchařík, Ph.D.

Contents

1 Introduction

Tremendous research efforts have been invested in recent years into the fabrication of functional surfaces. The functionality of many industrial parts and products depend on how their surfaces interact with the surroundings. The choice of material used for a certain application is usually limited by required mechanical properties. The intrinsic material properties often limit surface functionality. Therefore, surface functionalization is a suitable method to maximize the value of a product and enable new properties for common materials. For example, the value of a motorcycle helmet can be improved if it is more aerodynamic or if it repels dirt better. A glass surface can act as self-cleaning superhydrophobic surface dramatically improving visibility during heavy rain when used as a car windshield. Another example may include anti-corrosion, drag reduction, anti-ice, anti-bacteria or friction reduction surfaces fabricated on common metal and plastic surfaces.

There are two commonly used techniques for surface functionalization. The first is to use another type of material in a thin layer (surface coatings) to change the surface chemistry without affecting the bulk properties. This work is focused on the second technique, which is surface structuring (texturing). Eventually, both of these methods can be combined for better results. The inspiration in the design of functional surfaces often comes from nature by replicating surface micro/nanostructure geometry. A common example is the famous lotus leaf when the combination of chemistry (wax coating) and hierarchical surface micro/nanostructures results in extremely water repellent surface [1]. Another example can be shark's skin microtexture which improves hydrodynamic properties [2], or adhesive nanostructures on gecko feet, which allows the gecko to climb on a vertical glass sheet or antireflective texture of Moth-eye [3].

A large variety of fabrication methods have been developed for fabrication of functional surfaces including chemical vapour deposition [4], chemical etching [5], sol-gel [6], plasma treatments [7], thermal embossing [8], lithography [9], electrodeposition [10] or laser microstructuring [11]. However, most of these techniques are too slow to be implemented in an industrial environment or they require chemicals and thus are not environmentally

friendly. Among these, laser surface texturing offers a flexible, fast and environmentally friendly method for high-quality fabrication of desired micro and nano geometries with high precision and on a large variety of materials.

The size of functional structures is usually in a range of a few tens of microns to hundreds of nanometers. Therefore, it makes a great challenge to optimize laser and processing parameters. Usually, ultrashort laser systems (picosecond laser pulses and shorter) are applied due to minimal heat input into the surroundings of the interaction zone. However, if a larger heat-affected zone is acceptable, longer pulses are often applied due to generally higher processing rates.

Recent progress in the development of high power and high pulse energy laser systems reveals new challenges for laser microstructuring and surface functionalization. High precision which is necessary for the fabrication of micro and nano-scale functional structures often limits maximum pulse energy and power to be close to the ablation threshold. As a result, only a small portion of laser power is used during processing. There are several methods that can be used to optimize microstructuring with high power laser systems. Ultrafast polygon scanning systems can be utilized with high power high repetition rate (> 1 MHz) laser systems. Contrarily, multi-beam approaches including interference processing and multi-beam scanning techniques are much more suitable for high-energy pulsed laser systems. These techniques can significantly increase productivity compared to common direct laser writing (DLW) while keeping sufficient quality.

Aim and motivation of this work

Rapid development in the field of high power short and ultrashort laser systems is a promising step for rapid large-scale surface micro and nanostructuring. However, methods which can effectively use the full power of these laser systems for precise fabrication near the ablation threshold are still lacking. The aim of this work is to develop methods for surface functionalization by laser induced micro and nanostructures with the focus on superhydrophobic surfaces due to many potential applications in science and industry including for example self-cleaning, anti-icing, anti-bacteria, anti-corrosion surfaces. In the

next step, surface functionalization is scaled up by means of rapid large-scale approaches suitable for high-power high-energy pulsed HiLASE laser systems.

To fulfil this goal, work presented contains a review of suitable microstructure geometry for superhydrophobic, anti-icing and anti-bacteria surfaces. Suitable fabrication methods are presented with the focus on laser micro/nanotexturing with optimal parameters and state-of-the-art fabrication techniques for rapid-large scale laser microstructuring. The experimental section then uses this knowledge for fabrication of functional surfaces and is presented in a form of scientific papers published in international journals

2 Functional surfaces

The inspiration of functional surfaces often comes from inexhaustible nature examples such as lotus or rice leaf, mosquito eye, shark skin, butterfly wings, cicada wings, red rose petals, fish scales, gecko feet, spider silks [12,13]. Biological systems had billions of years to develop strategies ensuring their survival. Their functional performances often arise from hierarchical structures composed of multiple macro, micro and nanoscale features assembled into a complex structure. The discovery of their advantageous structure-property-performance relations inspired extensive efforts for study and replication of naturally occurring functional structures. A high effort has been invested into developing strategies for multi-scale structure fabrication. However, the controlled assembly of multiple-length scale features remains a challenging task [13-15]. In this chapter, a brief review of suitable surface topographies is presented with an emphasis on superhydrophobic, anti-ice and anti-bacterial surfaces.

Other applications of functional surfaces based on surface micro and nanostructures include holographs for goods protection, security elements and decoration, friction reduction, self-cleaning, anti-corrosion, drag-reduction surfaces and enhanced heat transfer, refractive index changes in transparent materials [16].

2.1 Superhydrophobicity

Among a plethora of natural examples, superhydrophobic biological systems attract a lot of attention due to many potential applications of superhydrophobicity including anti-icing, anti-corrosion, self-cleaning or drag-reduction surfaces [17], lab-on-chip devices [18], control of cellular attachment and bacterial adsorption [19]. Wettability of a given surface is characterized by the static contact angle (CA) which is the visually measurable angle that a liquid makes with a solid. The surface is hydrophilic for a CA below 90°, hydrophobic above this value. The surface can be called superhydrophobic, when CA exceeds 150°. Another condition has to be fulfilled to call surface superhydrophobic and that is either contact angle hysteresis (CAH) or sliding angle (SA) below 10°. CAH is the difference between advancing

and receding angle of a water droplet. It reflects contact angles which the water droplet inhibits during the motion. The advancing angle reveals the hydrophobicity while receding angle hydrophilicity [20].

In general, the wetting conditions are described by the two factors: the chemical composition and the surface roughness, which both affects the surface free energy (SFE) – the work that would be necessary to increase the surface area of a solid phase.

The wettability of an ideal flat surface is described by Young-Laplace equation [21]:

$$\gamma_{SA} = \gamma_{SL} + \gamma_{LA} \cdot \cos \theta \tag{1}$$

Where γ_{ij} is the surface tension between neighbouring surfaces. Subscripts i,j denotes S, L, A – solid, liquid and air phase, respectively (see Figure 1). The γ_{SA} is responsible for the spreading of a liquid, while γ_{SL} and γ_{LA} resist the spreading due to an increase of surface tension between the two surfaces [22].
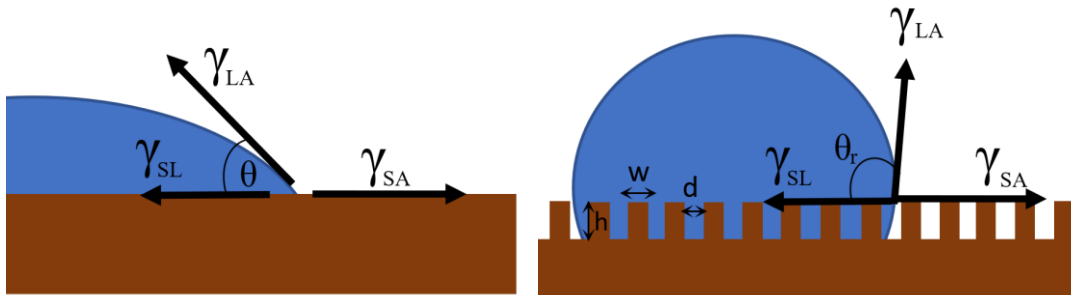

Figure 1: Schematics of surface tensions on a flat surface – Young model (left) and on a rough surface – Wenzel model (right).

If the surface is ideally flat, the wettability is determined by the chemical nature of the different phases. In this case, the maximum CA is limited to ~ 120° [23,24]. However, suitable topography of a rough surface can increase the CA over this value due to increased surface area. The ratio between the apparent and actual surface area which is in a contact with the liquid is expressed by a roughness factor r and can be used in a Wenzel equation [25]:

$$\cos \theta_r = \frac{r(\gamma_{SA} - \gamma_{SL})}{\gamma_{LA}} = r \cos \theta \qquad (2)$$

As expressed by the equation, roughness impacts the apparent contact angle θ_r, which is often different from the one expected from the Young equation. A droplet on a rough surface spreads until it reaches an equilibrium state characterized by Wenzel equation.

Roughness and surface geometry are main leading factors responsible for wetting of microstructures since they affect the surface energy. As an example, we can take a rectangular groove with a width α and depth β (Figure 2). Then the following equation expresses the change in surface energy during liquid progress through the groove by a distance dx:

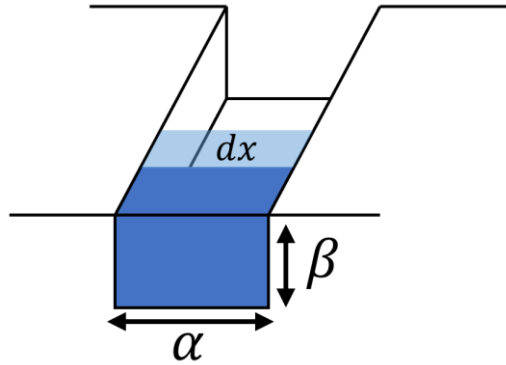$$dE = (\gamma_{SL} - \gamma_{SA})(2\beta + \alpha)dx + \gamma_{LA}\alpha dx \qquad (3)$$

Figure 2: Schematics of the wetting of microgroove surface.

The liquid moves by a distance dx when $dE < 0$. Therefore, there is a critical Young angle $\theta_c = \arccos\left(\frac{\alpha}{2\beta + \alpha}\right)$, which is the maximum Young angle θ when droplet wets the surface and progresses through the groove [24].

For a narrow and deep groove is $\theta_c = 90°$ which is the theoretical breakpoint between the hydrophilic and hydrophobic surface. For very shallow holes with β/α ratio close to 0 is $\theta_c \sim 0°$ resulting in a complete wetting similar to a flat solid.

However, the most common topography of the superhydrophobic surface is an array of micropillars. We assume a surface covered with an array of micropillars with following parameters (Figure 1): height h, hatch distance d, width w, number n. To simplify, we can assume unity of macroscopic surface: $nd+nw = 1$. Then for the actual substrate area, we can write $nw+nd+2nh = r$, where r is the roughness factor from equation (2). Now we can modify equation (3) for a change in the surface energy during spreading of the liquid between n pillars over a distance dx:

$$dE = (\gamma_{SL} - \gamma_{SA})(r - \varphi)dx + \gamma_{LA}(1 - \varphi)dx \tag{4}$$

Where $\varphi = nw$ is a micropillar density. Therefore, similarly to the previous case, the surface is wetted if:

$$\theta < \theta_c = \arccos\left(\frac{1 - \varphi}{r - \varphi}\right) \tag{5}$$

From equation (5) it can be concluded that wettability can be changed by controlling the roughness factor r and micropillar density φ. For example, large r and small φ lead to large θ_c, thus easy-to-wet surface.

The best natural examples of water repellent surfaces had microcavities which can entrap air bubbles and are not easily wetted. In such case, liquid drops are usually suspended only on the top of micro and nano rough features due to air trapped between the solid-liquid phases. Thus, apparent CA cannot be described by the Wenzel model.

The formation of an air trapped between microstructures is energetically favourable if in equation (4) $dE < 0$. Then:

$$\theta < \theta_c = \arccos\left(-\frac{1 - \varphi}{r - \varphi}\right) \tag{6}$$

In this case, the surface is hydrophobic ($\theta > 90°$) when $r > 1$.

The apparent static contact angle can be calculated for the static droplet using an energy balance equation [24]:

$$(\gamma_{SA} - \gamma_{SL})\varphi dx + \gamma_{LA}(1 - \varphi)dx + \gamma_{LA}\cos\theta^* dx \qquad (7)$$

where

$$\cos\theta^* = -1 + (1 - \varphi)\cos\theta \qquad (8)$$

Equation (8) is called the Cassie-Baxter equation describing contact angle on a rough surface able to keep air pockets when a droplet is deposited on the surface.

However, droplets in a Cassie-Baxter state are metastable and can switch to Wenzel state which is less energetic. Thus any perturbation or pressure to a Cassie drop can initiate droplet transition to Wenzel state, resulting in a decrease in CA and increase of CAH [24]. The size of a droplet is also important, the smaller is the droplet diameter compared to the distance between pillars the deeper is the penetration between pillars until it reaches critical diameter $R^* \sim d^2/h$ and switches from Cassie-Baxter to Wenzel state [26]. Therefore, the height and density of pillars are critical parameters for stable Cassie droplets.

As observed in nature, robust and stable Cassie-Baxter droplets can be formed on a surface with tall pillar-like arrays covered with nanoscale features. This double-scale design can be observed on already mentioned lotus leaf surface [12] or on the mosquito eye which can repel droplets larger than 100 nm thanks to an array of pillars with 100 nm high and 100 nm spacing ($R^* = 100$ nm) [27] (see Figure 3). Droplets of these sizes are vaporizing almost instantly, which allows mosquito eye to remain dry even in the foggy environment.
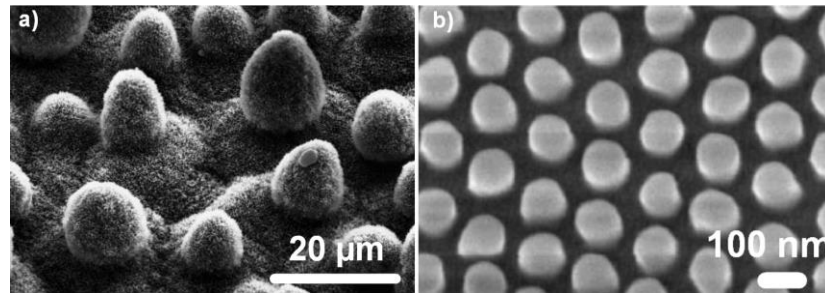

Figure 3: SEM images of lotus leaf (a) and mosquito eye (b) surface topography [27,28].

By optimizing the design of microstructured surface, it is possible to achieve superhydrophobic Cassie-Baxter state even for originally hydrophilic material with Young angle $\theta < 90°$. As shown in literature [29,30], overhang or re-entrant microstructures (e.g. T-shape, inverted triangle – see Figure 4) are able to resist a Wenzel transition by pressing on the liquid with the Laplace pressure [24] to hang a wetting liquid droplet and prevent it from penetrating into the air pockets. Thanks to the topography, these structures enable local minimum in surface energy even for wetting liquids with minimal surface tension like oils [30-32]. Moreover, double re-entrant nano/microstructures (e.g. re-entrant microstructures covered with nanoscale features) could provide sufficient wetting resistance even for $\theta = 0°$. In this case, omniphobic structures (repel all liquids) may be fabricated solely by suitable microstructure design without any chemical modification [22].

Figure 4: Illustration of overhand and re-entrant microstructures covered with nanoscale features [22].

However, it is worth to mention, that in the case of continuous wetting or surface fully immersed into a liquid the air pockets are depleted in time due to diffusion of air into water and surface is fully wetted afterwards [33].

In summary, wettability of a surface can be characterized by the CA. Surface with water CA < 90° is hydrophilic, with CA > 90° hydrophobic and for CA above 150° superhydrophobic. For superhydrophobicity also CAH or SA has to be < 10°. Several models can predict CA on a surface. Young model is suitable only for ideally flat surfaces with maximum possible CA ~120°. To improve wettability further, roughness has to be introduced on the surface. Wenzel and Cassie-Baxter theories explain wettability through the surface roughness. According to the Wenzel equation (2) describing a fully wetted surface, the originally hydrophilic surface will become more hydrophilic and originally hydrophobic more hydrophobic with the increase in surface roughness [34]. On the other hand, Cassie-Baxter equation (8) describes rough surface, which is able to trap air between

surface features when a droplet is deposited on the surface. In this case, water repellence can be enhanced for both, originally hydrophilic and hydrophobic surface. By optimal design of microstructures (re-entrant and overhang nano/microstructures) is possible to repel any kind of liquid without additional chemical treatment.

2.2 Anti-icing

Anti-icing surfaces have been studied since the 1950s [35]. However, the design of surfaces with the ability to delay ice formation is still a great challenge for science and industry. Ice formation may be dangerous and lead to accidents when ice is formed on helicopter blades or plane wings. It also decreases the performance of radars, antennas and complicates the maintenance of electric power lines [36,37]. Current anti-icing techniques including chemical treatments to decrease freezing point (salt, chemical sprays), mechanical vibration or Joule heating are focused on removing already formed ice while not preventing its formation. In addition, these techniques require toxic chemicals or intensive resources. For all these reasons, the development of anti-icing surfaces is devoted to passive anti-icing functional surfaces [38-40]. The most promising anti-icing surfaces are surfaces with superhydrophobic behaviour discussed in the previous section due to minimal contact between the liquid and solid surface [41,42].

There are many publications dealing with the optimal design of micro/nanostructures for anti-icing surface [38,43-46]. The findings can be summarized into the following points:

- Freezing time delay is mainly dependent on temperature and environmental conditions. Lower is the temperature or stronger is the wind, the less effect has the surface structure on the ice formation.
- Microscale structures provide high CA, low SA and CAH, therefore minimal contact between solid and liquid. They are resistant to freezing drop impacts and decreases ice adhesion. On the other hand, they are prone to mechanical damage during ice removal and can´t protect the surface from condensation freezing.

- Nanoscale features smaller than critical ice nucleus (temperature-dependent) prolongs freezing delay time. They may withstand several icing and de-icing cycles with stable Cassie-Baxter state.
- The most suitable structure design combines the effects of micro and nanostructures.

2.3 Anti-bacteria

Presence of bacterial biofilms causing infections limits the performance of medical tools and implants [47]. Currently, the most common causes of medical implant failure are due to formation of pathogenic bacteria biofilm, which may result in systemic infection and serious health damage [48]. For example, a study by Troidle [49] demonstrated biofilm formation of the most common pathogen bacteria (S. aureus, E. coli, P. aeruginosa) on all catheters removed from patients participating in the study. Investigation of the prevention of bacteria attachment to surfaces is an issue of great concern [50].

To prevent biofilm formation, antimicrobial agents are commonly used [51]. However, many bacteria developed resistance to common agents. An alternative may be metallic nanoparticles [52] or laser surface structuring [53]. The toxicity of metallic nanoparticles to both, the bacteria and surrounding human tissue is the limiting factor of this method [52]. On the other hand, roughness and surface topography of micro and nanosized features were shown to play an important role in cell adhesion, proliferation, differentiation, morphology and orientation [54].

The bacterial cell ability to attach on the surface relies on the interactions between the surface and cell wall functional groups [55]. It was shown that surface features smaller than bacteria cell size can limit its ability to attach on the surface due to the limited amount of attachment points [56]. Fine surface micro/nanostructures may be also more effective than extremely smooth surfaces [57]. Another factor influencing the cell attachment is wettability [53,58]. A minimum contact area between solid and liquid in a superhydrophobic Cassie-Baxter state may minimize the contact area between cells and surface [58]. On the other hand, superhydrophilic surface may also reduce bacteria adhesion due to larger repulsive force on

the proteins necessary for bacteria attachment [59]. For these reasons, laser surface structuring is a suitable tool for fabrication of antifouling surfaces preventing bacterial adhesion.

However, the number of parameters influencing bacteria behaviour is rather large making it difficult to optimize. Results presented in [55] shows change in bacteria attachment with different surface topography including mirror polished surface (Ra ~ 30 nm), microspikes (~ 20 µm), LIPSS (~ 500 nm) and nanopillars (~ 800 nm) for two common bacteria cells, E. coli (rod-like gram-negative) and S. aureus (spherical gram-positive), as depicted in Figure 5.
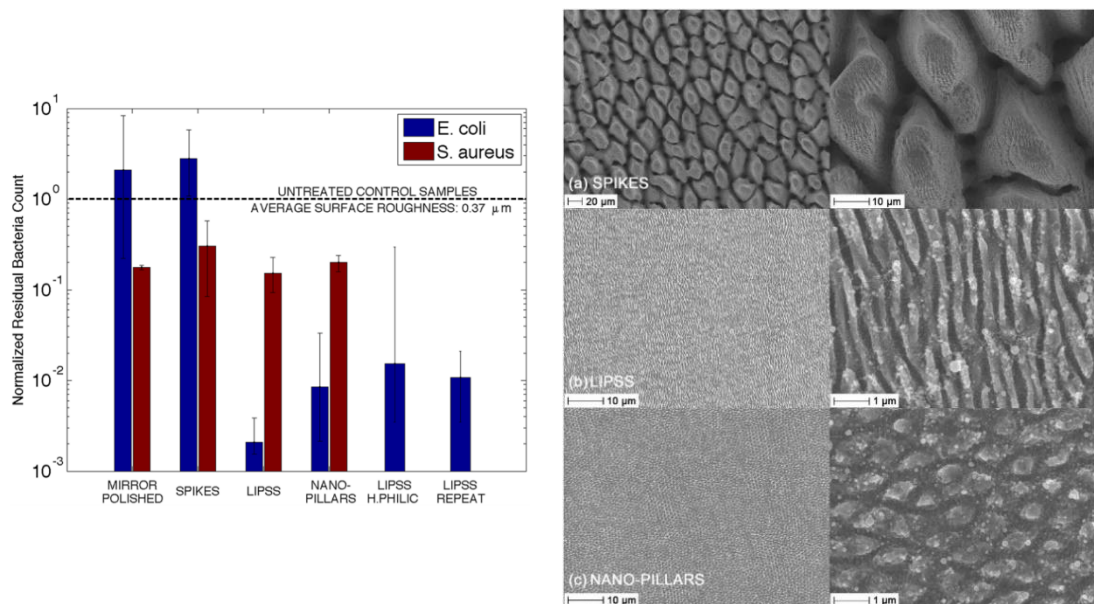
Figure 5: The geometric average of normalized residual E. coli and S. aureus bacteria counts for different surface geometries and corresponding SEM images [55].

These results demonstrate that anti-bacterial properties also depend on a cell type. Rod-shaped E. coli with typical dimensions of 0.5 µm x 2 µm occupy ~ 1 µm^2 whereas spherical S. aureus occupy ~ 0.25 µm^2. This was found as the main reason for much lower E. coli bacteria count on LIPPS (~ 0.5 µm) compared to the S. aureus. On the other hand, bacteria adhesion is smaller for S. aureus on the mirror-polished surface or superhydrophobic microspikes.

In conclusion, to prevent bacteria attachment to the surface, surface topography, chemistry and wettability play a major role. Anti-bacteria surface features should be smaller than particular bacteria cell size to decrease cell adhesion by minimizing the number of attachment points. Typical bacteria cell sizes are often below 1 µm, which is in favour of LIPSS and nanoscale features. Better results may be also achieved if these structures have superhydrophobic or superhydrophilic character. Thus, ultrashort pulsed lasers are a suitable tool to fabricate anti-bacteria surface topographies.

2.4   Summary

- Hierarchical structures combining micro and nanoscale features are the key factor for mentioned functionalities.

- Structure morphologies are similar - by tailoring the superhydrophobic surface structures additional functionalities may arise.

- Superhydrophobic surfaces can be considered as the base material for anti-icing surface. Moreover, superhydrophobic properties may also influence bacteria retention.

Hence from all these reasons, the experimental section will be mainly focused on the production of hierarchical micro and nanoscale structures with superhydrophobic properties.

3 Fabrication methods

A large variety of fabrication methods have been developed over the past years for the production of functional microstructured surfaces. Based on the previous chapter, selected methods able to produce suitable surface topographies which are applicable in industry environment will be briefly introduced as an alternative to laser nano/microstructuring which will be discussed in detail. These methods may include coating and deposition techniques, casting and electrospinning, which are scalable at large surfaces, fast and cost-effective. However, control over the structure formation is limited. And methods with good control over the structure formation such as lithography, etching and laser nano/microstructuring. Also, chemical treatments like chemical vapour deposition or plasma treatments may be used separately or in combination with microstructuring to decrease surface energy.

Electrospinning [60] may be used for fabrication of large-area superhydrophobic surfaces by introducing hydrophobic polymer solutions (e.g. polyvinylidene fluoride, polystyrene) on a surface forming a membrane of nanofibers. The average size of nanofibers can be controlled by solution flow rate and applied voltage allowing to tune the wettability. The produced structure geometry is random, unable to modify to the desired shape of microstructures.

Another large-area treatment is **spray coating** [61]. The polymer or nanoparticle solutions are sprayed on a substrate and solidify into a thin film. Usually, a glue layer is sprayed prior to nanoparticles to enhance adhesion with the substrate.

Dip coating [62] method is also commonly used as a fast and cheap method to functionalize the substrate surface. During the process, the sample is immersed into a solution to introduce roughness and low energy coating on the top surface.

Casting [63] is a cost-effective method for surface functionalization. This method uses suspensions of nanoparticles, crosslinkers or prepolymers which solidify into porous scaffolds onto the material surface.

Photolithography [64] is the most common technique for fabrication of an array of nanoscale features. Re-entrant omniphobic (repel all liquids) structures can be fabricated by photolithography with precise control over each individual structure. However, the fabrication speed is the main limiting factor for industrial use.

Etching [65] is widely used for complex micro/nanostructure fabrication. Material is removed by an etchant which is liquid (wet etching) or gas (dry etching). Dry etching with anisotropic material removal rate is suitable for the fabrication of asymmetric arrays of micropillars with high resolution or for the fabrication of omniphobic surfaces.

3.1 Laser surface structuring

Laser surface structuring is a non-contact, non-polluting and flexible alternative to the previous fabrication methods. With properly optimized parameters, it is possible to produce desired micro or nanostructure geometries on a large variety of materials with high precision, fabrication speed and minimal heat affected or damaged material.

For efficient micromachining process, precise ablation and high processing rates, it is necessary to understand basic laser and processing parameters and principles of laser-matter interaction.

Absorption

The wavelength of a laser source is a crucial parameter directly affecting the amount of radiation absorbed. According to the Lambert-Beer law, for incident radiation and minimal refraction, reflection or scattering, the absorbed intensity can be described as follows:

$$I(z) = I_0 \cdot e^{-\alpha z} \tag{9}$$

Where I_0 is incident intensity, $I(z)$ is intensity in depth z and α is the absorption coefficient.

By proper choice of laser wavelength is possible to improve process efficiency and quality. Metals have often high surface reflectivity at wavelength 1064 nm of Nd:YAG laser and thus small absorption (Figure 6a). Therefore, the use of lasers emitting in a green or UV

region may increase productivity and precision. Common plastics depicted in Figure 6b are transparent at 1064 nm and strongly absorbing in UV region [66].
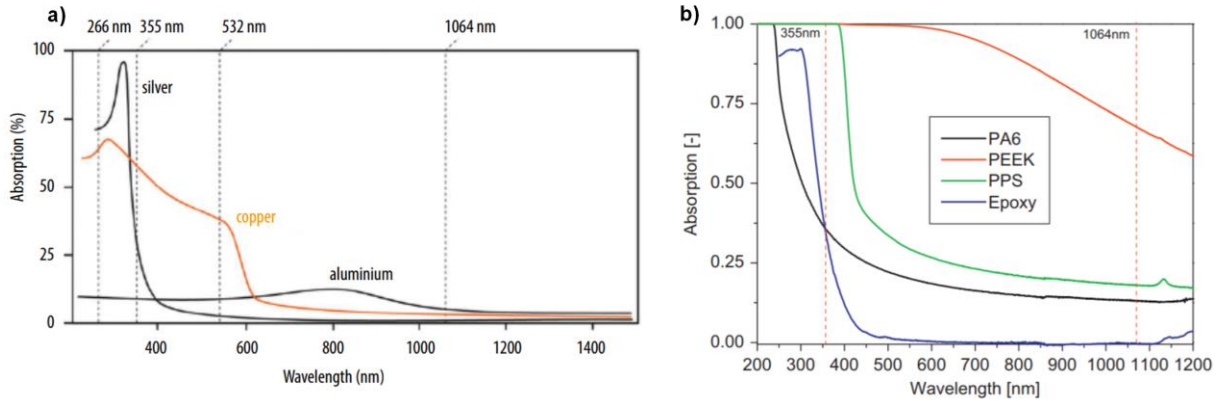

Figure 6: Example of radiation absorption in metals (a) and plastic (b) [66,67].

Moving towards lower wavelength, photon energy increases, and it is possible to observe strong linear absorption for materials with a wider bandgap (typically dielectrics). However, laser systems have usually fixed wavelength, or they are limited to high harmonic generation. Another technique which may be used to tune wavelength is the optical parametric generation (OPG) which has the advantage of continuous change in wavelength [68].

Considering intensity $> 10^{12}$ W/cm^2 a non-linear absorption, when the absorption coefficient is a function of intensity, may occur. At such high-intensity levels, it is possible to ablate almost any material, metals and dielectrics with a wide bandgap alike. However, major processes responsible for absorption in metals and dielectrics are different: The intra-band transitions comprise the electrons excitation and heating in metals. The inter-band transitions and electron excitation from the valence to the conduction band are important for absorption in dielectrics [69]. Metals are strongly absorbing even at the low laser intensity, while most of the dielectrics are transparent up to the optical breakdown threshold. Optical breakdown for dielectrics lies in the intensity range of a few TW/cm^2 [70] that corresponds to the fluence of 0.1 J/cm^2 for 100 fs laser pulse. At the optical breakdown, up to 10% of valence electrons

23

are transferred to the conduction band resulting in a strong increase of intra-band absorption with minor effect on other parameters [71]. This phenomenon can be observed in Figure 7, where absorbed energy density in a dependency on absorbed laser fluence for aluminium and silica is compared [72].
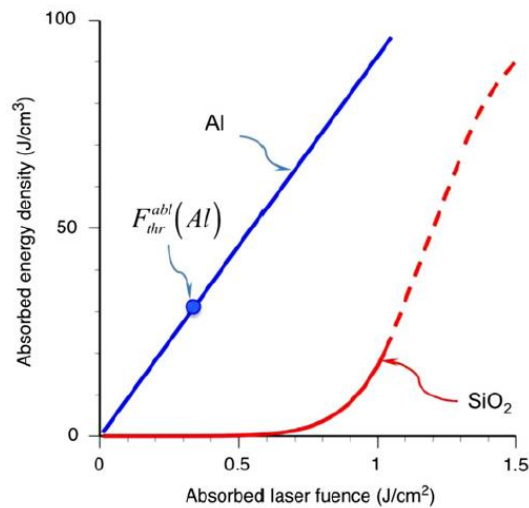

Figure 7: Absorbed energy density in a dependency on absorbed laser fluence for aluminium and fused silica. The ablation threshold for aluminium is marked on the blue aluminium curve [72].

Dielectrics are transparent at a low intensity for the laser wavelength down to the ultraviolet range, in other words, they have low absorption at low laser intensity. The increase in laser intensity leads to ionisation of the target in a skin layer. The ionisation occurs through single-photon ionisation, multi-photon ionisation, tunnel ionisation [73] or by avalanche ionisation [74]. Multi-photon processes are shorter than the pulse duration, therefore, material properties are modified during the pulse, affecting the interaction process. The absorption increases due to ionisation while the absorption depth decreases [69]. Higher energy absorption leads to acceleration of electrons in the valence band to energy exceeding the bandgap, resulting in ionisation and conversion of dielectric to metal-like state. Any dielectric converts to metal-like solid when the laser intensity approaches the ablation threshold [75]. Gamaly [69] concluded that at intensities above 10^{14} W/cm^2, the ionisation time for a dielectric is just a few femtoseconds. The electrons produced by ionisation in dielectrics then dominate the absorption in the same way as the free carriers do in metals,

and the characteristics of the laser-matter interaction become independent of the initial state of the target. As a result, the inverse Bremsstrahlung and resonance absorption become the major absorption mechanisms for both metals and dielectrics.

Absorption can be further controlled by surface modification – by increasing the roughness or by coatings. Surface properties are also often modified during multi-pulse irradiation. In this case, material absorption is increased during the first N pulses improving the ablation rate [76].

Pulse duration

Pulse duration is a very important parameter responsible for different ablation regimes and directly affecting the processing rate and thermal damage to the material. In the case of the continuous regime or long pulses down to µs, the material is heated up and melted. It is a purely thermal process which is suitable for laser welding, cladding or hardening, but cannot be used for laser microtexturing (Figure 8). With decreasing pulse duration down to ns (short pulses), the material can be removed by ablation. We can distinguish two ablation regimes by a pulse duration compared to the electron-lattice thermalisation time for a certain material. When the duration of a laser pulse is longer than the electron-lattice-relaxation time, which is of the order of picoseconds, the pulse hitting the sample surface will excite electrons. Their energy is then transferred to the lattice phonons and heats it up to the boiling and/or to vaporization temperature. After that, electrons and lattice are in thermal equilibrium [69,77,78].
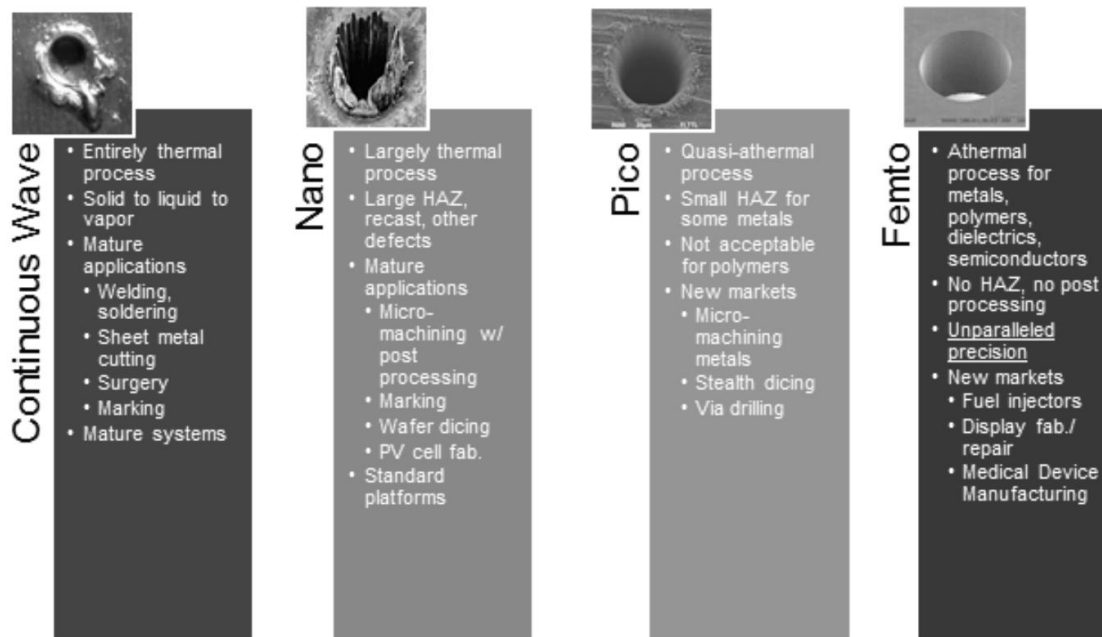
Figure 8: Comparison of the hole quality and potential applications of laser systems with different pulse durations [79].

For ultrashort femtosecond laser pulses, which are short compared to the electron-phonon relaxation time, an additional mechanism called Coulomb explosion was reported [80]. The fundamental processes can be described as follows. A sample surface is irradiated with ultrashort (ps, fs) laser pulses and the energy of the laser field is absorbed in the sample surface by electrons via inverse bremsstrahlung [81]. For energies above the ablation threshold, the energetic electrons escaping from the solid create a huge electrostatic field of charge separation, which pulls the ions out of a solid [69], therefore, no thermal load to the material occurs. For fs pulses, the electrons are excited instantaneously and thermalize on a time scale of ~100 fs [82]. During excitation and thermalization of the electronic system, the lattice stays "cold". On a much longer time scale in the order of a few ps, electron-phonon coupling, i.e., transfer of energy from the electronic system to the lattice takes place.

Therefore, despite the fact that quality is improved for ns pulses compared to the long ones (Figure 8), it is still a thermal process. Sample melting, melt expulsion due to vapour pressure and recoil pressure, as well as redeposition of aerosol onto the sample surface, greatly affect the accuracy and precision. "Cold" ablation regime of ultrashort pulses

(~ below 10 ps) is therefore favourable for precise micromachining. Moreover, heat diffusion length l_H, connected with pulse duration according to equation 10, limits the minimal achievable structure size [83]. When the structure resolution is below the heat diffusion length, structures may collapse into a melt pool due to insufficient distance between them. For example, the heat diffusion length of tungsten is 2,6 µm for 100 ns pulse and only 3 nm in case 100 fs (see paper E).

$$l_H = \sqrt{\frac{K \cdot \tau}{\rho \cdot c_p}} \tag{10}$$

where K is the thermal conductivity, ρ is the material density and c_p specific heat capacity.

Another difference between ultrashort and longer pulses is in the interaction with plasma. As can be seen in Figure 9, in fs case, plasma will be formed after the end of the pulse, whereas in ns case, plasma is formed during the laser pulse. This plasma plume can scatter and absorb energy (shielding effect) from laser radiation, reducing the ablation efficiency [84].
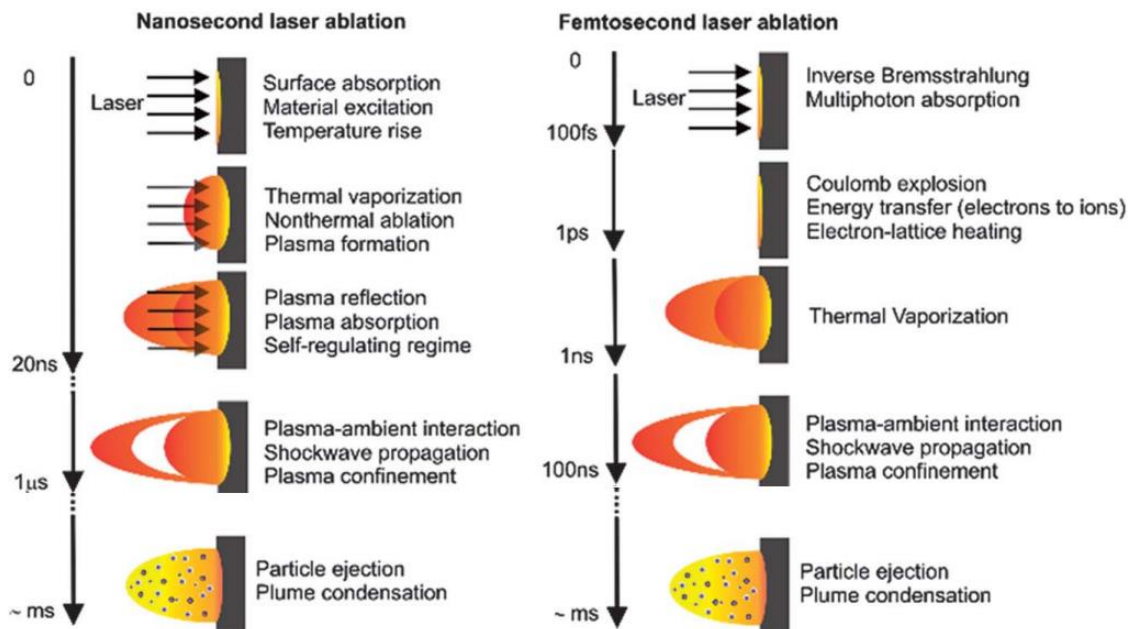

Figure 9: Approximate time scales of laser pulse absorption and ablation. along with the processes that accompany it [85].

Despite the better quality and cold ablation regime of femtosecond pulses, short penetration depth of ultrashort pulses results in a low ablation rate [69]. Thus, there is a trade-off in pulse duration and ablation rate, see Figure 10. Consequently, picosecond or even nanosecond pulses may be favourable with properly optimized parameters, as demonstrated in papers A and B.
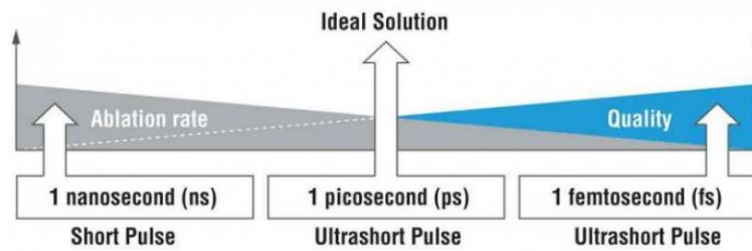

Figure 10: Illustrative drawing of trade-off in pulse duration and ablation rate for laser machining [86].

Repetition rate

Except for pulse duration, repetition rate may also greatly influence the quality of produced microstructures. If the repetition rate is too high the time between consecutive pulses may be shorter than the required cooling time which may lead to increase in local temperature between consecutive pulses and melting of the material (Figure 11) [87].
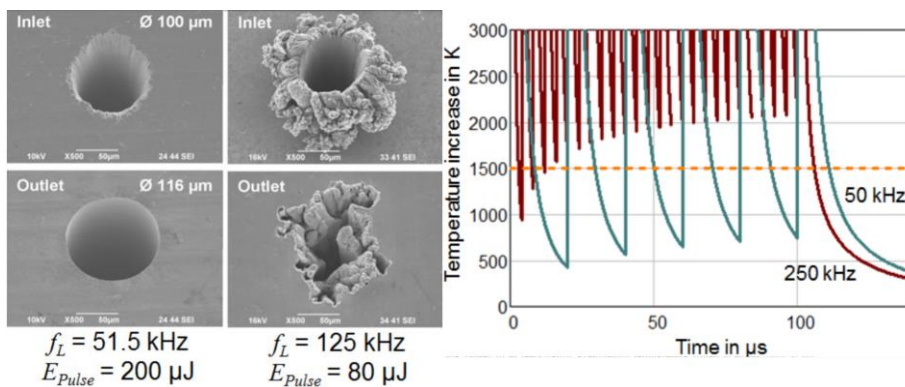

Figure 11: Example of a hole quality drilled using different repetition rates and graph demonstrating temperature increase between consecutive pulses [87].

High repetition rate in MHz regime can also decrease the ablation rate due to absorption of consecutive pulses in plasma and ejected particles, as depicted in Figure 9.

Beam parameters

In most cases, laser systems are generating Gaussian-like beams. The transverse profile of the optical intensity of fundamental (Gaussian) mode TEM_{00} of laser resonator can be represented by the following equation:

$$I(r,z) = I_0 e^{\left(-2\frac{r^2}{w(z)^2}\right)} \tag{11}$$

where $I_0 = \frac{P}{\pi w(z)^2/2}$ is the peak intensity and P is the power, $w(z)$ is the distance from the beam axis where intensity I_0 drops to $1/e^2$.

Beam propagates through space with a certain divergence θ (see Figure 12):

$$\theta = \lim_{n \to \infty} \left(\frac{w(z)}{z}\right) \cong \frac{\lambda}{\pi w_0} \tag{12}$$

where λ is laser wavelength and ω_0 is the beam waist, which is the beam size at the focus ($z = 0$).

Thus, beam radius is increasing with the distance z as follows:

$$w(z) = w_0 \sqrt{1 + \left(\frac{z}{z_r}\right)^2} \tag{13}$$

where $z_r = \pi w_0^2/\lambda$ is Rayleigh length (a distance from a waist where the area of the cross-section is doubled). In some cases, confocal parameter (or depth of focus) $b = 2z_r$ is used instead.
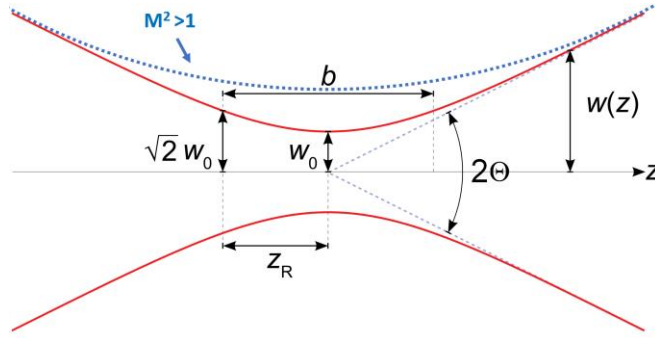
Figure 12: Caustic of laser beams with marked beam parameters.

To describe the quality of laser beam a beam parameter product (BPP) is applied as the product of beam radius and beam divergence. The higher BPP the worse quality is the beam.

$$BPP = M^2 \frac{\lambda}{\pi} = w_0 \theta \tag{14}$$

where factor M^2 quantifies the deviations from Gaussian beam, which has $M^2 = 1$ and thus smallest BPP. M^2 provides the "times diffraction limit" that a laser spot can be focused. Equation (14) also points out an essential relation between beam diameter and radius. The smallest is the beam radius, the bigger is the divergence and vice versa.

For laser micro and nanostructuring is important to reach small spot sizes. The focus spot size $D = 2w_0$ fulfils:

$$D = M^2 \frac{4\lambda f}{\pi D_0} \tag{15}$$

where f is the focal length of a lens. Therefore, shorter wavelength or shorter focal length can be used to decrease the spot size.

In some cases, also different intensity distributions are advantageous. For example, a top-hat beam with near-rectangular intensity distribution can improve ablation efficiency and quality by minimizing heat affected zone (HAZ) [88]. As depicted in Figure 13, top-hat beams are much more suitable for precise ablation and stitching, when shaped to rectangular

footprint. Another example may be Bessel beams which can be used for glass cutting due to smaller focal spot size and elongated depth of focus [89].
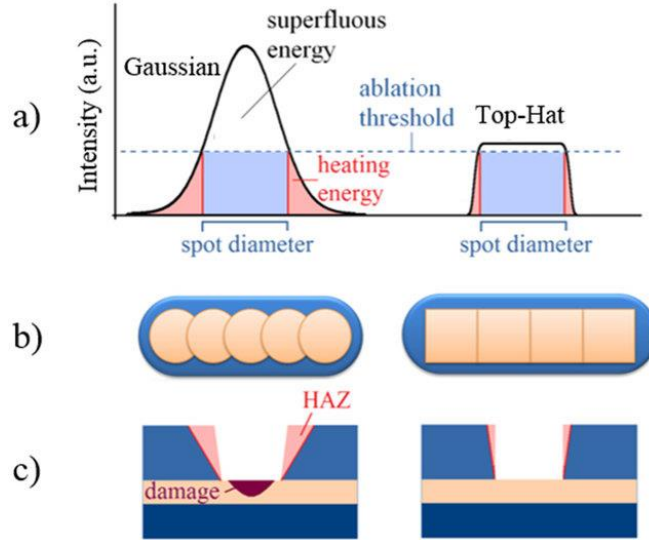

Figure 13: Comparison of Gaussian and top-hat beam distributions. (a) intensity profiles, (b) stitching footprint, (c) cross-section of processed material with marked HAZ [88].

Processing parameters

Fabrication of well-defined and melt free nano/microstructures requires optimization of processing parameters and processing strategies. Basic laser processing parameters include the spot to spot overlap o, scanning speed v_s, number of pulses per unit area N_p, number of overscans N.

Pulse to pulse overlap is an important parameter for stitching the pulses over larger areas. It is typically higher than 60% for a circular beam to ablate straight line. Overlap can be defined as follows:

$$o = 1 - \frac{l}{2w_0} = 1 - \frac{v_s}{f_r 2w_0} \tag{16}$$

where f_r is the laser repetition rate and l is the distance between the centres of two neighbouring spots. Using equation (16), scanning speed equals:

$$v_s = (1 - o)\, 2w_0 f_r \qquad (17)$$

For a number of spots per unit area (number of pulses per focal spot) we can write:

$$N_p = \frac{D f_r}{v_s} \qquad (18)$$

These parameters together with the number of overscans (number of process cycles) have to be optimized to prevent overheating of the sample and melting of the material close to the interaction zone due to heat accumulation.

Beam displacement over the sample is an important aspect for a proper scanning strategy, defining heat distribution and precision of microstructures. The simplest way is to use linear stages to displace the beam in two orthogonal directions. However, the maximum speed of state-of-the-art linear stages is ~ 2 m/s, which limits processing rates. In addition, the mass of sample and stages limits the acceleration and deceleration times and thus affecting the duty cycle significantly. Without these delay times, the overlap is increased at the beginning and at the end of scanned geometry making inhomogeneous ablation of desired geometry. When laser on and laser off delays are applied correctly to provide enough time to reach constant speed, the device is accelerating prior to making desired geometry (so called skywriting), which increases processing times but ensures constant overlap. In addition, synchronization of laser triggering is necessary to accurately define the starting position, see Figure 14.
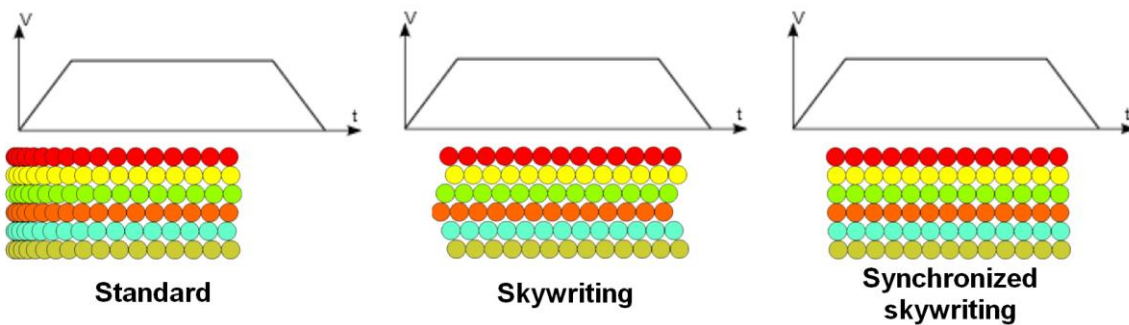

Figure 14: Example of different scanning modes [90,91]

To reach higher scanning speeds, galvanometric (galvo) scanners are commonly used. They are using two galvo scan mirrors to deflect an incident beam in X and Y direction (see Figure 15a) and F-theta lens. F-theta lenses are engineered to have a planar imaging field compared to simple spherical lenses which can focus deflected beam only on a spherical plane (Figure 15b). This issue can be addressed by flat-field scanning lens (Figure 15c) however the distortion of the focused spot on a flat focal plane is dependent on the product of focal length f and tangent of a deflection angle θ. F-theta lens is a flat field lens designed with built-in barrel distortion. The position of the focal spot is then dependent on the product of f and θ simplifying positioning algorithms (Figure 15d).
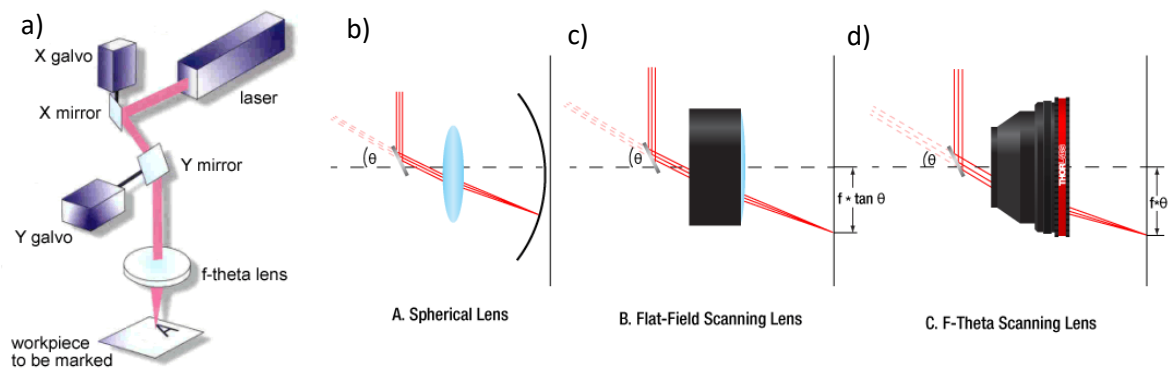

Figure 15: (a) Illustration of galvo scanner system [90]; Comparison of spherical (b), flat-field (c) and f-theta (d) lenses [92].

The maximum speed of commercially available galvo scanners reaches ~10 m/s [90,93]. However, the effective speed is reduced due to necessary laser on and laser off delays during acceleration and deceleration of galvo mirrors. For high-speed scanning, this delay times can increase the processing time up to more than 50% [91].

With processing of large areas, another issue has to be addressed. Scanning fields of galvo scanners is limited to tens of cm^2 depending on the mirror size and F-theta lens. Moreover, mirror size and thus scanning field is decreasing with higher scanning speeds due to obvious reasons. Therefore, working areas of galvo scanner have to be stitched to cover larger areas by means of stages. However, stitching errors and an increase in processing time are unavoidable. These stitching errors can be very small in the order of a few micrometres with

properly aligned and synchronized scanner and stages. However, even that is significant in micro and nanoprocessing. Recently, companies like Aerotech or Scanlab start to address this issue and presented synchronized continuous motion of stages and galvo scanner. In this case, stitching errors can be eliminated and the scanner working area extended over the whole range of stages. However, this technology is currently limited to 2D or 2.5D processing (2 axis + galvo scanner).

4 Rapid large-scale approaches of laser surface structuring

As discussed in the previous section, laser surface structuring is a suitable tool for fabrication of various micro and nanostructures providing different surface functionalities. However, the fabrication speed of commonly used point to point approach - direct laser writing (DLW), is in a range of minutes per square centimetre [1,94,95], which limits the use of DLW for large-scale surfaces often required by industry needs.

Development of new high-power laser systems with corresponding high pulse energies and repetition rates facilitate large area micromachining applications on macroscopic areas with high throughputs meeting industry requirements. For example, ultrashort laser systems developed at HiLASE centre can nowadays deliver up to 500 W with pulse duration < 2 ps and either high repetition rate up to 1 MHz (Perla C) or high pulse energy up to 0.5 J (Perla B) [96]. In contrast to high available laser power, high quality laser ablation with minimal thermal damage require processing close to damage threshold [97]. Thus, only a fraction of available laser power can be used for high quality single spot laser ablation. Hence, new methods for rapid large-scale processing are necessary to use the full potential of high-power laser systems. The most promising rapid large-scale techniques include polygonal scanning systems [90,98,99], direct laser interference patterning [100-102] and multi-beam scanning approaches using DOE or SLM plate [103,104]. However, each of these approaches have its limits and drawbacks as well as different requirements for the laser source. These will be addressed in the following text.

4.1 Ultra-fast scanning systems

Current state-of-the-art ultrashort laser systems can provide very high repetition rates in MHz range. This enables new strategies for rapid large-scale processing of materials, especially ultrafast scanning techniques.

As discussed in the laser surface structuring section, commercially available scanning systems reach maximum scanning speeds of ~10 m/s [90,93], which is still insufficient to keep up with repetition rates in order of tens of MHz. This issue can be solved by polygon scanning systems, which can reach scanning speed of a few hundreds m/s [105].

Instead of a classical flat mirror used by galvo scanners, polygon scanners are using multifaceted polygon mirror, as depicted in Figure 16. The polygonal mirror is rotating around a fixed mechanical axis and the beam is angularly deflected every time facing the flat facet of the polygon. Since the mirror is rotating continuously, a higher number of scanned lines per second can be realized, compared to the back and forward motion of mirror in galvo scanner. Consequently, the polygon scanner does not need laser on and laser off delay times necessary for mirror acceleration or deceleration. However, the incident laser beam has to be completely on the facet during processing, which reduces the duty cycle and average laser power to ~60% [93].
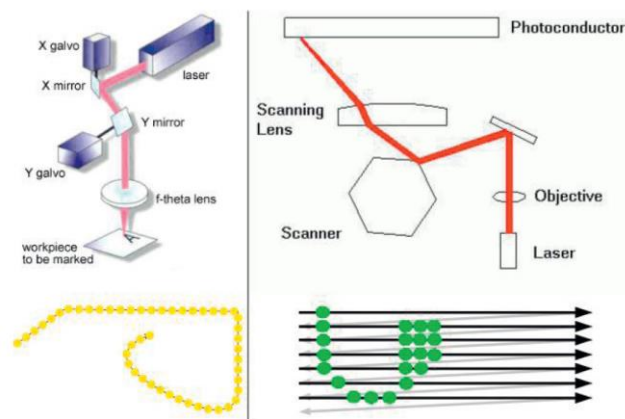

Figure 16: Scheme of classical galvo scanner (left) and polygon scanner (right) [90]. Galvo scanner can deflect the beam in X and Y plane, whereas polygon scanner is only one dimensional. The perpendicular direction to the polygon scanner direction has to be handled by stages.

Polygon systems have been successfully implemented for material processing such as texturing and engraving [105,106]. Comparing results already available in the literature, processing rates of 30 min/cm^2 have been reached for LIPSS formation on stainless steel with 2 MHz, 20 W, 400 fs laser system [98] and 1.3 min/m^2 for microstructuring of stainless steel with 76 W 20 MHz, 10 ps laser system [105].

However, the main disadvantage of this technology is the lack of flexibility. Processing solutions have to be tailored to fit the scanning technology since it is suitable only for flat surfaces. There is no time to adjust height during rapid scanning for the structuring of complex or 3D shapes. Another limitation lies in the line like (raster) or bitmap scanning

strategy. Polygon scanners are utilizing only one polygon mirror, therefore they are suitable only for 1D scanning. The second direction is usually handled by stages synchronized with the scanner. Consequently, not all applications are suitable for polygon scanning including, for example, trepanning, helical drilling or complex shape microstructuring. Therefore, polygon scanners are considered as a complementary technology to the existing galvo-based systems.

4.2   Direct laser interference patterning

Direct laser interference patterning (DLIP) is a technique when two or more coherent laser beams overlap on a surface in order to directly impose a periodic interference pattern on the material, see Figure 17. The geometry of the interference pattern can be controlled by the number of laser beams and their incidence angle as well as by wavelength, polarization, intensity and phase difference of these beams [100]. The DLIP technique demonstrated the capability of processing a wide spectrum of materials including metals, polymers and coated surfaces [34,83,107-109] with a processing speed up to 0.36 m^2/min for metals and 0.9 m^2/min for polymers [102]. It was shown that DLIP is capable of producing sub-wavelength structures not limited by a beam spot size and it became a fast and efficient way for laser micro-processing [101,110].
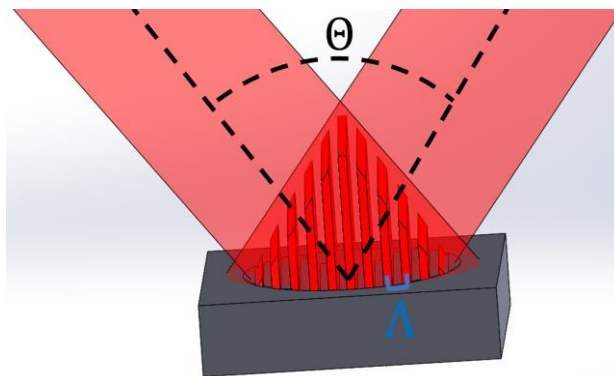

Figure 17: Illustration of two beam interference with incidence angle Θ and lateral period Λ.

The intensity profile of interfering beams in the interference area can be calculated using the formula [111]:

$$I(\vec{r}) \propto \left(\sum_{i=1}^{N} \vec{E}_i(\vec{r}, t) \right)^2 \tag{19}$$

where $\vec{r}$ is the coordinate vector, t is time, i is the index of interfering beams, N is the number of beams and $\vec{E}_i$ is the electrical field of i beam, which can be expressed as follows:

$$\vec{E}_i = \vec{E}_{0i} \cos (\vec{k}_i \cdot \vec{r} - \omega t + \varphi_i) \tag{20}$$

where $\left| \vec{E}_{0i} \right|$ is the amplitude of i wave, $\left| \vec{k}_i \right| = 2\pi/\lambda$ is the wave vector of i wave, λ is the laser wavelength, ω is the frequency of radiation and φ_i is the phase of i wave.

In the case that all interfering beams have the same frequency, periodical intensity field is formed and equations (19) and (20) can be simplified [112]:

$$I(\vec{r}) \propto \frac{1}{2} \sum_{i=1}^{N} \left| \vec{E}_{0i} \right|^2 + \sum_{j<1}^{N} \sum_{i=1}^{N} \vec{E}_{0i} \cdot \vec{E}_{0j} \cos (\vec{k}_i \cdot \vec{r} - \vec{k}_j \cdot \vec{r} + \varphi_i - \varphi_j) \tag{21}$$

As observed from equation (21), the interference period depends on the incident angle between the beams and on the wavelength. Therefore, the lateral dimensions of the interference pattern (spatial period Λ) can be controlled by the angle Θ between incident laser beams (see Figure 17) [113]:

$$\Lambda_N = \alpha_N \frac{\lambda}{\sin (\Theta/2)} \tag{22}$$

where $\alpha = 1/2$ for $N = 2$, $\alpha = 2/3$ for $N = 3$, $\alpha = \sqrt{2}/2$ for $N = 4$

Equation (12) shows the limit for minimal achievable periodicity, which can be smaller than the laser wavelength. Thus, it is possible to achieve sub-micrometre structures with common ~1 µm lasers which would not be otherwise possible without additional microscopic objectives. Moreover, this sub-micrometre resolution can be achieved in the whole

interference area. The size of overlapped beam region is reduced to several tens of micrometres in diameter by focusing lens with short focal length, which is necessary for high incidence angle Θ and thus small pattern periodicity according to equation 22. As an example, in paper C the overlapped beam region is reduced by focusing lens to 70 μm in diameter for two beam interference pattern and wavelength of 1064 nm. Inside this diameter, interference periods down to 2 μm were fabricated significantly increasing the fabrication speed compared to the single beam approach.

Higher throughputs can be reached by increasing the overlapped beam region. However, high enough pulse energy is necessary to be above the ablation threshold for larger areas and thus for a higher number of interference maxima. In addition, laser parameters like pulse duration, temporal and spatial coherence limits the maximal reach of interference area inside the overlapped beam region. Therefore, high quality and high pulse energy laser source is necessary for large-beam DLIP. The suitable pulse duration for a certain diameter of interference area d can be estimated by equation (23) for two beams overlapping at angle Θ [114]:

$$d \approx \frac{c\tau}{\sin(\Theta/2)} \tag{23}$$

where c is the speed of light, τ is the pulse duration.

Another important aspect of pulse duration is connected with heat diffusion length l_H (equation 10) which limits the minimal achievable structure size due to melting. Therefore, there is a trade-off between the interference area and heat diffusion length. The shorter the pulse duration, the finer the structures can be produced, but at the same time the smaller is the area of interference. Methods for increasing the diameter of the interference area above 1 mm and thus significantly increasing processing throughputs are presented in papers D, E.

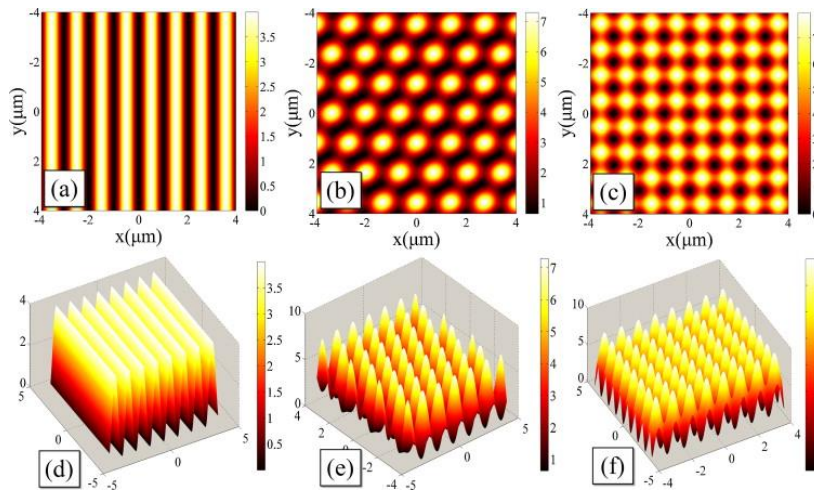The most common intensity distributions with N-beam interference are shown in Figure 18.

Figure 18: Simulations of 2D (a-c) and 3D (d-f) intensity distributions of two-beam interference (a,d), three-beam interference (b,e) and four-beam interference (c,f) [115].
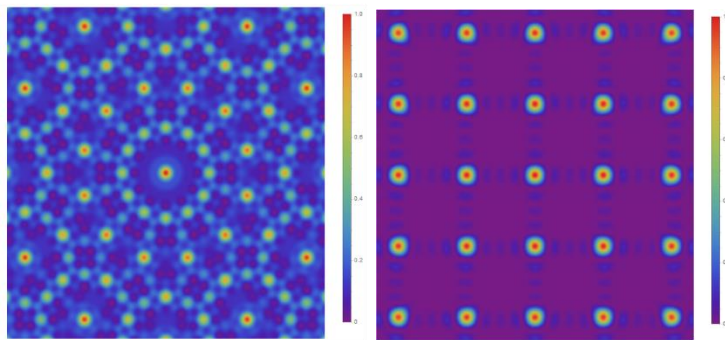

Figure 19: Exotic DLIP configurations: (a) Twelve beam interference pattern (b) 25 beam interference pattern [116].

Nevertheless, these intensities can be further tuned by different angle, polarization, intensity and phase difference of beams, the most reasonable patterns for microfabrication are a group of dots and lines. Thus, two, three and four beam interference (Figures 18) are the most appropriate. In some cases, a higher number of beams may be useful to get sharper intensity maxima or exotic patterns (Figure 19) [116].

These intensity distributions (Figure 18 and 19) are calculated with the assumption of an infinite monochromatic plane wave. However, the majority of laser systems are producing Gaussian-like beams. That results in higher intensity maxima in the centre of interference

area, which is dropping down to the edges following the Gaussian envelope, as pointed out by Alamri [117] (Figure 20).
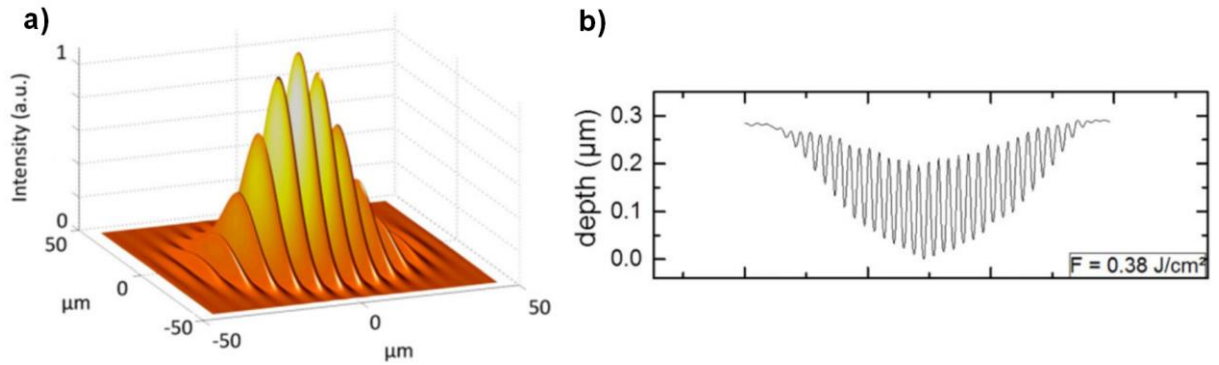

Figure 20: (a) Calculated intensity distribution obtained by overlapping two Gaussian laser beams ($\Lambda = 6$ µm); (b) Confocal microscope profile on polycarbonate foil ablated with the same intensity distribution [117].

As observed in Figure 20, except higher ablation depth in the centre of interference area, also unselective ablation (outside interference maxima) in the centre part occurs. All these reasons make stitching over larger area difficult and limiting hatch distance just to a few interference periods to reach homogeneous pattern distribution.

To obtain beams with the same parameters, splitting the initial laser beam is favourable compared to the higher number of laser sources. In this case, several beam-splitters may be used according to the desired number of beams. Moreover, when ultrashort pulses are applied, the setup has to be precisely aligned to achieve homogeneous pattern distribution in the whole interference area. The major challenge of multi-beam interference with ultrashort pulses is achieving temporal superposition of pulses [118]. Compensation of temporal delay is necessary in this case. It is usually based on nonlinear frequency conversion methods of second or third harmonic generation. Levels of difficulty and complexity increase exponentially with a higher number of beams. Therefore, there are no efficient ways to form more than 7 beam interference [119]. A possible solution for a simple and precise multi-beam DLIP setup and ultrashort pulses are diffractive optical elements (DOEs). DOE inclines the wavefront that it remains perpendicular to the common optical axis, it also splits the beam in a small angle making possible to use the same optics for all splitted beams. That also ensures the same optical path for all beams, making alignment simple even for

femtosecond pulses. More details about DOE splitting will follow in chapter 4.3. Illustration of a beam splitter based and DOE based setup is shown in Figure 21:
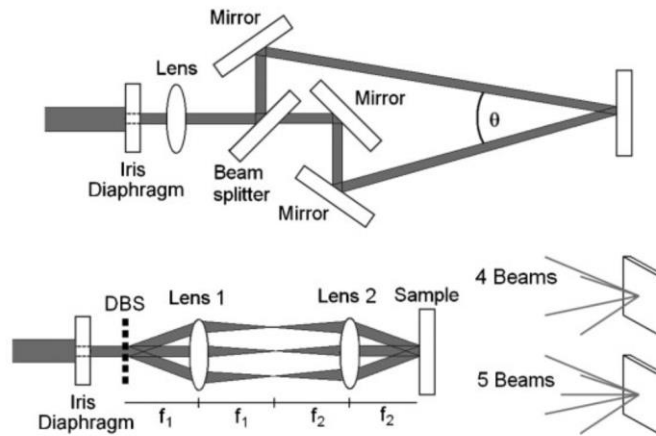

Figure 21: Interference setup based on beamsplitters (upper) and DOE (lower) [118].

In summary, among advantages of DLIP belong fast processing over a large area with sub-wavelength resolution. The speed of the fabrication process can be easily tuned by the size of the interference area. There is no need of special optics which may be damaged due to high pulse energies, fabrication speed can be scaled up to square meters per minute [102] with powerful enough laser source. Contrarily, the most significant drawbacks of DLIP are the limitations in shape control of the interference pattern. The reasonable pattern distributions are limited to the group of dots or lines. The separation distance between these shapes cannot be tuned independently of the period. Also, the formation of a uniform pattern is limited by the Gaussian spatial intensity distribution of the incident laser beam, resulting in higher intensity maxima in the centre of the interference area. Hence, it is also difficult to accurately overlap several interference areas for the highly uniform pattern over a large area.

4.3   DOE and SLM based multi-beam approaches

Beam splitting using Diffractive Optical Element (DOE) or Spatial Light Modulator (SLM) in a combination with high power ultrashort laser systems is a promising way to meet industry standards in high-speed processing of large areas. DOE beamsplitter distributes the incident laser beam intensity into a desired far field pattern, which is usually a 1D or 2D

array of M x N beams (see Figure 22), each splitted beam has the same characteristics as the original beam, except for pulse energy and angle of propagation. The number of beams, their location and propagation angle can be changed by DOE design. Also, as shown in Figure 22, it is possible to combine DOEs with each other.

DOE diffractive gratings, usually fabricated on fused silica substrates, enable to withstand high power damage thresholds around 10 J/cm^2 with common AR coatings [120]. The power efficiency (splitted beams to incident beam) is often > 70% for AR coated element and it can reach more than 95% [121]. The remaining power is distributed among the non-desired orders, mainly the 0th order of diffraction. Therefore, especially for high power cases, it is necessary to mechanically block the zero order to prevent undesirable damage of the sample.
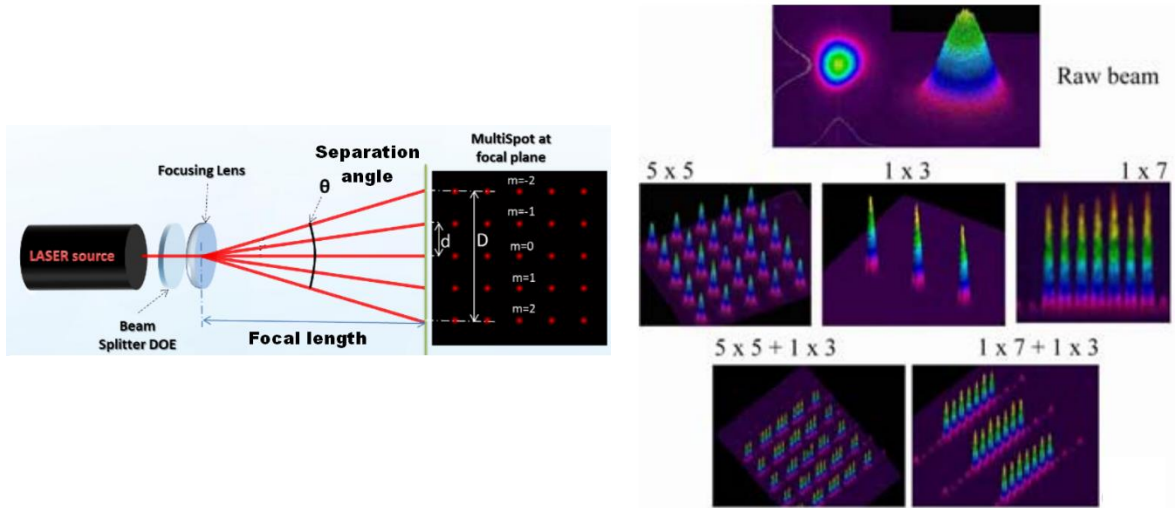

Figure 22: Illustration of DOE beam splitting (left) and DOE combinations (right) [120,121].

The DOE effectivity and uniformity of resulting pattern are mainly dependent on beam quality and in the case of multi-level high efficient DOEs also on the precise allignment. Computer-generated diffraction grating written in DOE body is usually calculated for a perfect gaussian beam. Therefore the effectivity and pattern uniformity may be decreased for M^2 > 1.2. Also, there is a requirement for minimum input beam size, which should be at least 3 times the size of the grating period Λ [121]:

$$\Lambda = \frac{m\lambda}{\sin \vartheta} \tag{24}$$

where Λ is a grating period of DOE, m is a diffraction order, λ wavelength, ϑ separation angle between beams.

It is worth to mention that capabilities of industry available DOEs are not limited to only beamsplitters, but continuous shapes like hollow rings, lines, squares and different intensity distributions can be generated.

The simplest DOE setup for rapid large-scale fabrication contains a laser source, DOE splitter, focusing lens and fast stages. The separation distance between spots on the sample can be controlled by the distance between DOE and focusing lens. DOE can also be fabricated to be compatible with F-theta lenses and thus to be used in a combination with a galvo scanner allowing much faster beam displacement. However, in this case, the separation angle between beams has to be small enough, or additional optics has to be placed after DOE to ensure that the pattern area fit the scanner mirrors. Example of drilling and cutting with DOE splitting the incident beam into 784 beams is reported in paper F.

Spatial light modulator (SLM)

Spatial light modulator (SLM) is a device that can modulate phase, amplitude or polarization of light waves. For laser beam shaping phase-only modulations are preferable due to energy reasons [122]. SLMs are usually based on liquid crystals controlled by a direct and accurate voltage, which can modulate a wavefront of the beam allowing high resolution, high speed reflective or transmissive phase modulation with individually addressable pixels to control beam shape, focus position and even intensity distribution [123]. It essentially works as a computer-controlled diffraction grating with each pixel introducing different phase delay. Consequently, SLMs are used for variable beam splitting and shaping applications [103,124,125]. Phase modulation is changed according to the alignment of liquid crystals, which may be controlled pixel by pixel. A difference in crystal tilt results in different refractive index, thus changing the optical path length and so causing a phase difference [126].

The diffractive patterns are generated in real-time by computer-generated holograms (CGHs), which can be calculated by appropriate algorithms [122,127]. Most algorithms for phase mask calculation are based on the fact that the phase mask and far field diffraction patterns are related through the Fourier transform [122,127]. For a good quality reconstruction of the calculated hologram, it is necessary to count with SLM parameters (for instance pixel distance, count, pixel geometry,…), reconstruction wavelength, beam quality and all other phase changes and aberrations introduced by optical system [128].

Examples of calculated phase masks uploaded on SLM and resulting patterns are shown in Figure 23. The grayscale tones correspond to the phase shift from 0 (white) to 2π (black). These phase masks form diffraction images on the sample.
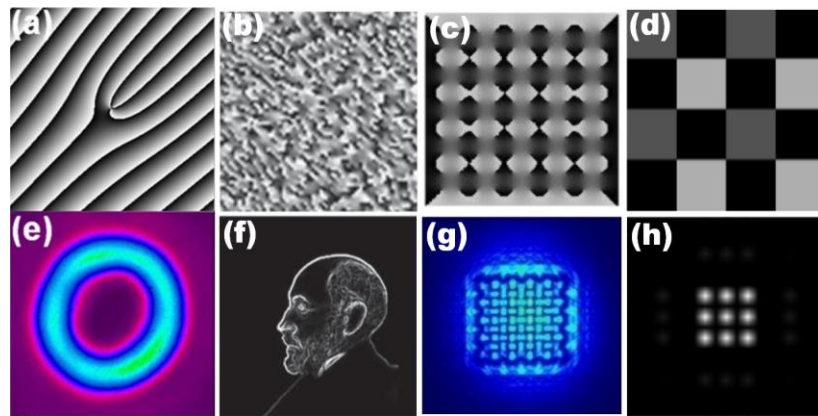

Figure 23: Calculated phase masks (a-d) and corresponding patterns (e-h) formed from a single incident Gaussian beam [123,129-131].

Another advantage of the SLM based systems is in a convolution of phase masks. For example, the focusing position of a diffraction pattern can be easily changed by convolving the phase mask of the desired diffraction pattern with a phase mask of a lens (Figure 24). Analogously, if optical aberrations of the whole system are known, they can be compensated by convolving with the appropriate phase mask.
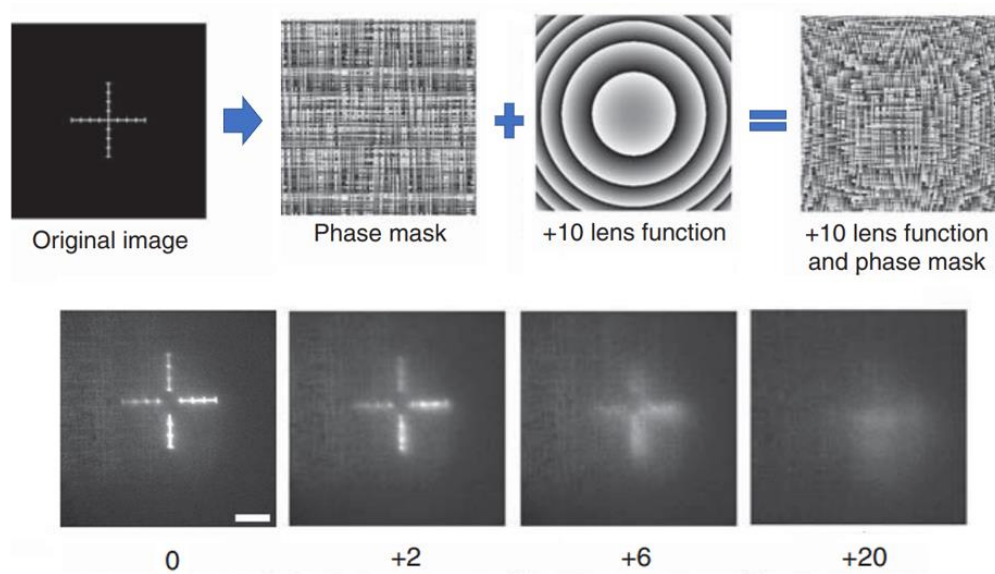
Figure 24: Example of a convolution of a phase mask of a cross with lens phase mask used for focus change. Observation of the defocused image is shown in the lower row [123]. Numbers represent the focal length of the imaginary lens.

For all these reasons, SLM has a great potential in multi-beam laser micromachining for speeding up the processing rate. The straightforward application is beam-splitting, where spacing and intensity of each beam can be changed independently, which is not the case of DOEs. Moreover, beam shaping, change in focus and compensation of aberrations of the optical system and the laser beam can be incorporated into the final phase mask. For rapid large-scale processing, pattern distribution over the sample is necessary. It can be done either by fast stages or galvo scanner (Figure 25).
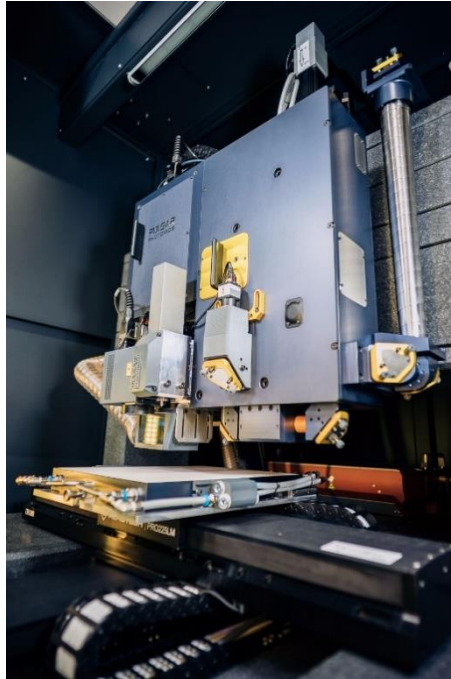
Figure 25: Industry ready SLM based micromachining station combined with galvo scanner and 3 axis linear stage system (Pulsar Photonics GmbH).

In conclusion, DOE based systems are easy to use, cheap and able to withstand high pulse energies necessary for multi-beam processing. The disadvantage is a fixed configuration of DOE generated pattern. Contrarily, SLM based system offers programable patterns which can be changed in tens of ms providing the freedom to the operator in design and optimization of pattern distribution according to the final application needs. Advantage of the SLM approach is also the possibility to compensate optical system aberrations and poor beam quality of laser source. However, the LIDT limit of SLM of ~ 0.5 mJ and 100W of average power is a significant drawback of this device.

4.4 Summary

Surface functionalities can be tuned by suitable microstructure geometry and impose new properties like superhydrophobicity, anti-ice or anti-bacteria to common materials. Laser is a suitable tool to fabricate such microstructures on a large variety of materials ranging from metals to dielectrics and composite materials.

Several laser and processing parameters had to be optimized for high-quality micro and nanostructure fabrication. The complexity of parameter combinations increases when state-of-the-art high-power laser systems are applied. To utilize the potential of these systems for the close-to-threshold fabrication of micro and nanostructures, new ultrafast scanning or multi-beam approaches had to be applied. Most promising approaches are polygon scanning systems, DOE based scanning systems, direct laser interference processing and programable SLM holographic processing coupled with galvo scanner.

Polygon scanning system is still only complementary technology to classic scanning approaches due to lack of flexibility and limitation to raster-only (or bitmap) scanning strategy of plane surfaces. Polygon scanner-based systems require very high repetition rate laser systems (> 10 MHz). These systems often had to generate ultrashort pulses in order to minimize heat accumulation due to a very short time between consecutive pulses.

Multi-beam approaches are much more suitable for higher freedom in microstructure geometry. DOE based systems are splitting the incident beam into the desired array of beams or another diffraction pattern, which is static and can be further displaced over the sample by means of scanner or stages. Interference based systems have an advantage in more freedom in pattern change by adjusting the periodicity and shape of inference pattern. Both methods are suitable for high pulse energies, therefore it is possible to generate a large number of beams to increase throughputs.

SLM based scanning systems have the highest degree of freedom in pattern generation. Except for simple splitting, SLM can further change intensity distribution and shape the beam. The disadvantage is a lower damage threshold (in the means of pulse energy and also average power). Therefore, the use with high average power laser systems is limited.

As a conclusion, all approaches have their advantages and limitations depending on the final application and available laser source. The optimal solution for rapid-large scale micromachining laboratory would be a combination of SLM-based scanning system to develop optimal diffraction pattern and process parameters and DOE-based scanning system with DOE manufactured according to final parameters found by SLM while providing much

higher LIDT to be able to use a maximum of a laser source. High-energy pulsed laser systems can also benefit from interference processing, which is a less expensive and more compact solution, easily scalable to structure large area in resolutions below the diffraction limit of common lenses while fully utilizing available pulse energy.

5 Experiment

The first step in the development of rapid large-scale surface functionalization by laser induced micro and nanostructures is the development of the fabrication process with optimal laser and processing parameters. Then in the following step, a process can be scaled up to higher processing speeds which require further optimization of processing parameters due to challenges connected with the processing technique and high-power input into the material.

As discussed in the previous section, superhydrophobicity has great potential for many scientific and industrial applications. The development of the fabrication process of superhydrophobic surfaces using a single beam in a combination with a galvo scanning system was developed at HiLASE Centre. Both, ultrashort laser system (1030 nm, 1.8 ps, 100 kHz) and nanosecond fibre laser source (1062 nm, 3 ns, 10 - 1000 kHz) were optimized for dual-scale (micro and nano) hierarchical structure fabrication on the top of aircraft aluminium alloy 7075, as depicted in paper A (ps laser source) and paper B (ns laser source). Despite the different physical phenomena during ablation with 1.8 ps and 3 ns laser pulses, it was possible to fabricate a dual-scale pillar-like array of microstructures covered with nanoscale features, which have a great potential for superhydrophobicity.

In the following step, interference processing was investigated, as it was found to be the most suitable for high-energy pulsed ultrashort laser systems available at HiLASE. In the first step, functional superhydrophobic microstructures were fabricated on carbon fibre reinforced composite plates in cooperation with Fraunhofer Institute for Material and Beam Technology using commercial nanosecond laser sources (Paper C). Based on this experience, an advanced interference processing station was designed and build at HiLASE, demonstrating two (Paper E) and four-beam (Paper D) interference processing with enlarged interference area for higher throughputs. Ultrashort pulsed laser system (1030 nm, 1.7 ps, 10 mJ) was used to generate interference patterns combining micron-scale interference pattern with nanoscale structures resulting in superhydrophobic surface properties and a change in structural colour.

Nevertheless, the direct laser interference patterning was identified as the most fitting to HiLASE laser sources, other approaches were proved to be useful for specific applications. Such an example is rapid parallel microdrilling and microcutting of several hundred microholes at once with exact dimensions and spacing. DOE splitter combined with galvo scanner was identified as the most suitable method in this case. As a result, the author successfully delivered a solution for microstructuring with 784 beamlets at the same time, significantly improving productivity (Paper F).

5.1   Journal article A. Non-fluorinated superhydrophobic Al7075 aerospace alloy by ps laser processing

In this publication, a technique for surface functionalization of aircraft aluminium alloy 7075 using 1030 nm picosecond laser source Perla 500 with 1.8 ps pulse duration and repetition rate of 92 kHz was reported. Nanoscale ripples (LIPSS), also in a combination with micropillars were successfully fabricated on the top surface. A novel method of post-treatment – vacuum processing, was applied to laser processed samples in order to speed up transformation time from originally hydrophilic to superhydrophobic state. This transition time was successfully reduced from a couple of days to only 4 hours. Corresponding chemical processes were analysed with the conclusion that synergic effects of hierarchical micro and nanostructures together with non-polar elements are responsible for superhydrophobic behaviour.

Author contribution
In the work related to the production of this journal article, the author contributed to the sample preparation. The author designed and performed experiment together with R. Jagdheesh, analysed results with J. Kopeček, P. Jiříček and both the author and R. Jagdheesh contributed to the final version of the manuscript drafted by R. Jagdheesh. Detail authors individual contributions are shown in table 1.

Term	Authors' individual contributions
Conceptualization	R. Jagdheesh, P. Hauschwitz
Methodology	R. Jagdheesh, P. Hauschwitz
Software	P. Hauschwitz, R. Jagdheesh
Validation	R. Jagdheesh, P. Hauschwitz, D. Rostohar
Investigation	R. Jagdheesh, P. Hauschwitz
Resources	T. Mocek, J. Mužík, J. Brajer, J. Kopeček, P. Jiříček
Writing - Original Draft	R. Jagdheesh
Writing - Review & Editing	R. Jagdheesh, P. Hauschwitz, D. Rostohar
Visualization	R. Jagdheesh
Supervision	R. Jagdheesh, J. Brajer, D. Rostohar
Project administration	Petr Hauschwitz, Jan Brajer
Funding acquisition	T. Mocek

Table 1: Credit author statement - Non-fluorinated superhydrophobic Al7075 aerospace alloy by ps laser processing.

Full length article

Non-fluorinated superhydrophobic Al7075 aerospace alloy by ps laser processing

R. Jagdheesh[a,*], P. Hauschwitz[a,1], J. Mužík[a], J. Brajer[a], D. Rostohar[a], P. Jiříček[b], J. Kopeček[b], T. Mocek[a]

[a] Hilase Centre, Institute of Physics, Academy of Sciences of the Czech Republic, Za Radnici 828, 25241, Czech Republic
[b] Institute of Physics of the Czech Academy of Sciences, Na Slovance 2, Prague, Czech Republic

A B S T R A C T

The metallic surfaces with low affinity or high repellence towards water molecules are extremely desirable. The present investigation reports the development of non-fluorinated super or ultrahydrophobic aerospace aluminum alloy (Al7075) surface by laser patterning and high vacuum process for 4 h. Lamellar and lotus leaf papillae like structures covered with nanoscale protrusions are found to be formed depends on the laser fluence and spatial shifts of laser scans. The fresh laser processed hydrophilic surface was vacuum processed to create layer of hydrocarbon to reduce the surface free energy for the wetting property transformation. The analysis of the results shows the synergistic effect of hierarchical structures and dominant presence of non-polar elements is critical for superhydrophobic property. The surface geometry is primarily responsible for the wetting property transformation by entrapping μ-volume of air to generate a composite interface of solid-gas-liquid. Micro and nanoscale (dual scale) surface structures are essential for the durable and consistent superhydrophobic property with high degree of water repellence for bigger volume of water droplets. Further, sole presence of nanoscale structures on inherent hydrophilic aluminum alloy surface with predominant presence of non-polar elements can yield only near superhydrophobic surface due to random spacing of nanoscale protrusions.

1. Introduction

Water droplets rolling and jumping away from the superhydrophobic surface has drawn substantial interest among the researchers as well as automotive and aerospace industries. In nature, *Morpho Deidamia* (butterfly) makes advantage of micro/nano ratchet-like structures on the wings for the detachment of water droplets [1]. Lotus leaf shows extreme water repellence and self-cleaning ability from the roughness of their surfaces and this phenomena is referred as "Lotus effect" [2]. This self-cleaning property has been derived from the combined effects of the hierarchical surface structures (μ-scale papillae covered by nanoscale protrusions) and the hydrophobic wax-crystal coating on it, as the first layer of defense to water droplets [3–5]. To understand the water repellence property of natural species, hierarchical rose petal structures were developed by ultra violet nano molding technique [6]. In recent past, plethora of techniques have been applied to fabricate water repellent or superhydrophobic metallic surfaces [7–12].

Inspired by the natural water-repellent surfaces, different kinds of wetting surfaces such as super hydrophilic/hydrophobic and under-water super hydrophilic/hydrophobic surfaces were successfully fabricated [13–15]. In common, metals and metal oxides are hydrophilic due to high surface free energy. Simply modifying the surface roughness or patterning on the surface does not improve the wetting behavior, rather deteriorates to ultrahydrophilic condition [16]. However, water repellence or hydrophobic surfaces can be created on metals by the combination of patterning with appropriate geometry and low surface energy material coatings [16,17]. Laser ablation technique can be exploited to create hydrophilic surfaces for biomedical applications. Laser surface patterning was effectively applied to increase the surface wettability of polymers, which promotes the cell adhesion and spreading of cells [18]. Tailoring of surface structure and the chemical modification can alter the wetting property of metals. The surface structure of copper was modified by fs laser processing and chemical treatment for tuning the wetting property. The tuning was realized by varying the geometrical parameters [19].

Multifunctional stable aluminum (Al) surface was created by electrochemical machining method by Xu et al. [20]. However, the

* Corresponding author.
 E-mail addresses: r.jagdheesh@hilase.cz, jagdheesh@fzu.cz (R. Jagdheesh).
[1] Faculty of Nuclear Sciences and Physical Engineering, Czech Technical University in Prague, Brehova 7, 115 19 Prague, Czech Republic.

53

complicated preparation method and time consuming process cannot be implemented in industrial environment. Superhydrophobic Al surface was also created by femtosecond (fs) laser patterning and treated with Penta deca fluorooctanoic acid to transform wetting property from hydrophilic to superhydrophobic [21].

This process takes few hours and involve the use of fluorine compound. Low adhesion and reliable superhydrophobic millimeter scale surface structures were developed by combining electrical discharge machining and solution immersing technique [22]. Nevertheless, these techniques involve chemical treatment with fluorine compounds, which is considered to be hazardous for the environments. Eco friendly aging technique as well as the exposure to different environments were successfully demonstrated and the process periods varies between few hours to several days [23–26]. Gianvito Caputo [12] et al. has applied the moderate vacuum (3×10^{-3} mbar) for the improvement of wetting properties of TiO_2 nanocrystals on thin films. However, the process time is 40 h and the reported static contact angle (SCA) value is 90°. Similar effects were reported by Long et al. [27] for the sample aged in vacuum at a pressure of 5 Pa for 8 days and the contact angle was in hydrophobic range, which can be considered as rose petal effect.

In this work, we report the fabrication of picosecond (ps) laser patterned non-fluorinated superhydrophobic Al7075 aerospace alloy surface by creating nano/micro scale surface structures. The hierarchical surface structures were subject to wetting property tests and chemical analysis to determine the influential factors for the dewetting character after vacuum process.

2. Materials and methods

An infrared (IR) ultrafast laser source (HiLASE Centre, PERLA 500) with pulse width of 1.8 ps was employed to create hierarchical surface structures on Al 7075 aerospace alloy (chemical composition Si: 0.4; Cr: 0.18; Cu: 1.5; Fe: 0.5; Zn 5.1; Ti: 0.2; Mg:2.2; Mn:0.3; Balance: Al; all in wt%) plates of size $10 \times 10 \times 5$ mm. The surface roughness of the as received samples were about Ra: 450 nm. The laser source can deliver 500 W average power at frequency of 92.2 kHz. The beam passes through 5 bending mirrors, $\lambda/2$ plate, beam expander and a Galvo scanner with F-θ lens of 120 mm focal length before striking the sample surface. A combination of $\lambda/2$ plate and polarizer was used to manipulate laser power. The micromachining experiments were realized in atmospheric conditions with apparent spot size of 80 μm with a scan rate of 300 mm/s for three power levels such as 1, 2 and 4 W. μ-pillar geometries were produced by bidirectional scanning and varying the spatial shift of laser beam from 20 to 150 μm. The spatial shift would be referred as pitch "P" for future citation throughout text. Detailed experimental parameters are shown in Table I. The laser patterned samples were ultrahydrophilic immediately after processing. The samples were stored in high vacuum chamber for 4 h, within few minutes of laser processing to create non-polar elements on the dual scale microstructures.

The sub-micron scale structures were examined with scanning electron microscope (SEM) (Tescan FERA 3) and geometrical parameters were studied by laser scanning microscope (Olympus OLS5000). The wetting behavior of the samples were analyzed by measuring the static contact angle by the sessile drop technique using the Video-based optical contact angle measuring device (OCA 15EC, Data Physics Instruments). Further, the samples were tested for sliding angle (SA) to understand the rolling effect.

Static contact angles (SCA) measurements were made at ambient pressure and temperature with distilled deionized water droplet of volume 8 μL. An average of 3 SCA measurements at various points of laser patterned region has been reported. The transformation in the surface chemistry after the high vacuum [7] has been analyzed by X-ray photoelectron spectroscopy (XPS) technique (Kratos analytical, AXIS Supra). ESCApe data acquisition software was used for the detailed analysis of observed peaks.

3. Results

Lamellar structures have been fabricated with two directional laser scans with pulse-to-pulse overlap of 99%. Fig. 1 shows the lamellar structures generated by ps laser sources with different number of laser pulses/spot ranging from 24 to 122 pulses. A and B series samples have been processed with 0.21 J/cm² and 0.43 J/cm² respectively. For all the specimens, the periodicity of lamella is found to be 1 μm, comparable with the wavelength (1030 nm) of laser beam used for structuration. The laser processed lamella structures were completely covered with random nanoscale protrusion and nanowire like structures. It is evident from the SEM analysis, the amount of nanoscale features increases with respect to number of pulses as well as with increase in incident energy. At lower fluence, pulse to pulse overlap of 99% and spatial shift of 20 μm, the surface experience partial melting leads to lamella structures without physical separation. The increase in incident energy by a factor of two induces more physical separation and promotes the formation of random nanoscale protrusions on the lamella structures. The abundant presence of nanoscale structures reduces the effective fractional area of contact between the solid and liquid phases.

Fig. 2 shows the laser fabricated nanoscale structures along with the micron scale pillars at regular intervals. Different levels of P, from 20 to 150 μm have been experimented to mimic the lotus leaf's papillae structures [2]. The increase in fluence caused the disappearance of lamellar or micro ripples structure and favored formation the domes of nanoscale size. The micro pillars start appearing at higher fluence P ≥ 100 μm, with troughs between the pillars are covered with nanoscale protrusions. Like the lotus leaf papillae, the μ-pillars are completely covered with nanostructures. This is due to the low power density distribution of the Gaussian beam profile. Moreover, the entire laser patterned surface has nanoscale protrusion in addition with micro scale features resulting in dual scale hierarchical structures.

Laser patterned surface clearly shows the presence of dual scale surface structures after laser ablation. Fig. 3 demonstrates the relation between the surface roughness (Ra) and number of pulses/spot with different P values. The surface roughness improves with respect to the number of pulses/spot as well for the increase of P values. According Wenzel's equation [28], surface roughness improves the intrinsic wetting property of materials.

$$\text{Cos } \theta = R_f \text{ Cos } \theta_0 \tag{1}$$

$$R_f = \frac{A_{SL}}{AF} \tag{2}$$

θ: contact angle of a rough surface; θ_0: contact angle of a plane surface; R_f: ratio of the solid–liquid area A_{SL}, and protrusion on a plane surface AF. As per the Eq. (1), roughness improves the static contact angle only if $\theta_0 > 90°$ and if $\theta_0 < 90°$ then the contact angle for the rough

Table I
Laser process parameters.

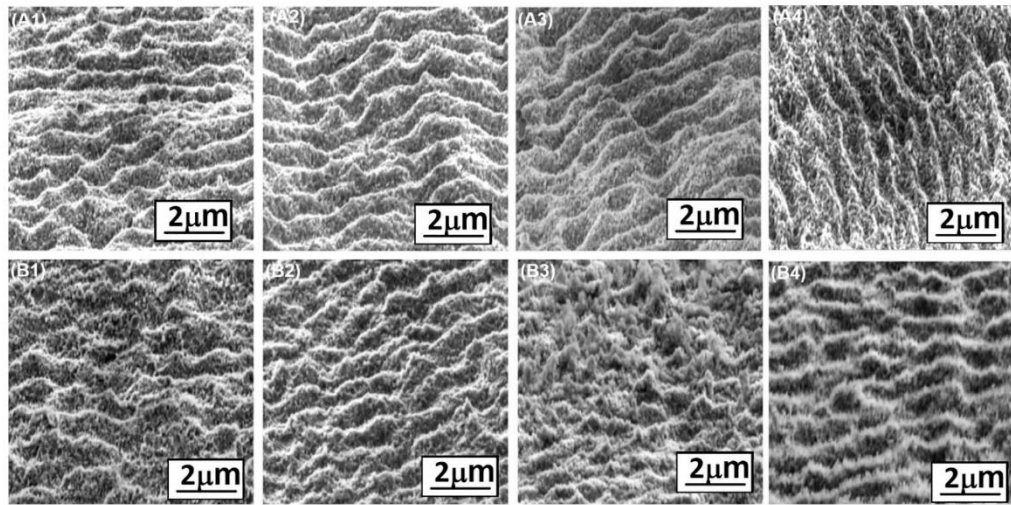| Sample name	Laser power (W)	Energy/pulse (μJ)	Apparent spot size (μm)	Fluence (J/cm²)	Number of pulses/spot	Pitch (μm)
A1-A4	1	10.86	80	0.21	24–122	20
B1-B4	2	21.73		0.43	24–122	20
C1-C5	4	43		0.86	240	20–150

Fig. 1. Scanning electron microscope of lamella structures fabricated by ps laser at different fluences and pulse/unit area. A1: 24 pulses; A2: 48 pulses; A3: 96 pulses; A4: 122 pulses with the fluence of 0.21 J/cm^2; B1: 24 pulses; B2: 48 pulses; B3: 96 pulses; B4: 122 pulses with the fluence of 0.43 J/cm^2.

surface will decrease with increasing Rf. Hence, Wenzel model is not appropriate for the intrinsically hydrophilic materials. Therefore, it requires post-processing technique to create a layer of low energy materials covering the dual scale microstructure.

Non-fluorinated eco-friendly robust superhydrophobic surface has been fabricated by vacuum process [7,16] of laser patterned samples for 4 h at high pressure of 10^{-4} Pa. Fig. 4(A) represents the static contact

angle measured for 0.21 and 0.43 J/cm^2 with respect to number of pulses/spot. The highest SCA obtained is about 143 ± 3° for 0.43 J/cm^2 at 122 pulses/spot. Due to high spatial overlaps (20 μm), the average depth of the microstructure is in the range of micron. However, all the samples are hydrophobic and the value of SCA depends on the depth of the microstructures. The highest SCA is recorded for the samples processed with the fluence of 0.43 J/cm^2.
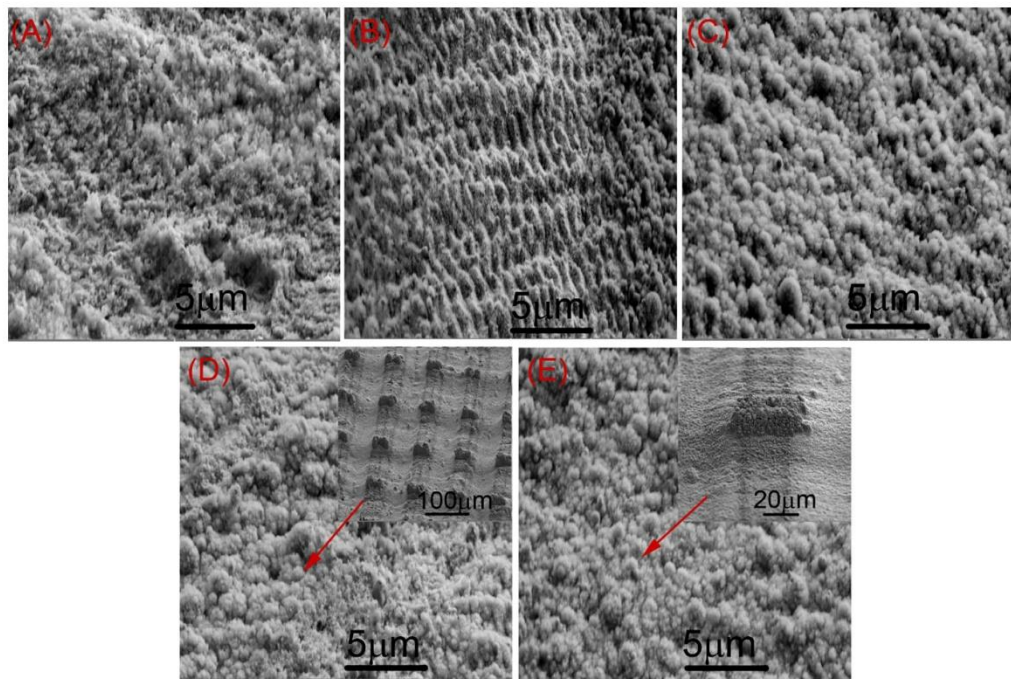

Fig. 2. Scanning electron microscope of submicron scale structures fabricated by ps laser at different pitch (P), with 240 pulses/spot; C1: 20 μm; C2: 40 μm; C3: 60 μm; C4: 100 μm; C5: 150 μm, with the fluence of 0.86 J/cm^2.
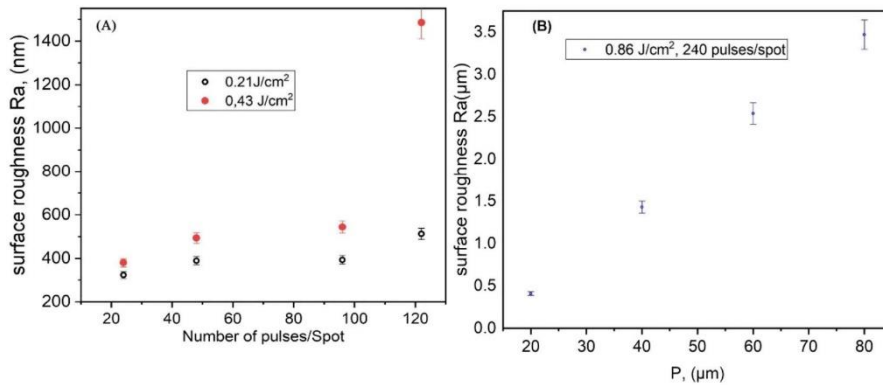
Fig. 3. Roughness measurements as a function of number of pulses/spot for fluence value of 0.21 J/cm^2 and 0.43 J/cm^2 (A); Roughness with respect to P for constant number of pulses/spot at fluence of 0.86 J/cm^2.

The samples processed with higher fluence (0.86 J/cm^2) and lower spatial overlap (higher P values), are extremely water repellent as depicted in Fig. 4(B). The lotus leaf papillae structures (P: 100 &150 μm) showed extreme water repellence with maximum value of 180°, which is termed as ultrahydrophobic [7]. Sliding angle measurements were performed on all the laser patterned samples with the water droplet volume of 8 μL. The samples which were fabricated with the fluence of 0.86 J/cm^2 and pitch distance of 100 and 150 μm has shown lotus effect with SA < 5°. Remaining samples with random spacing of the nanostructures have high SA values > 45°, which implicates non-existence of super or ultrahydrophobic property.

According to Young's equation, the static contact angle is the relation between the surface tension of the composite interface; $\gamma_{SA} - \gamma_{WS} = \gamma_{WA} \cos\theta$ (γ_{SA}- Interfacial tension between solid and Air; γ_{WS}- Interfacial tension between water and solid; γ_{WA}. Interfacial tension between water and solid). The outer layer of the laser patterned metal surface is covered with a layer of metal oxides [7,16], which has high γ_{SA} leads to complete wetting. As γ_{SA} decrease, the droplet tends to take hemispherical shape with a high SCA and dewets the surface.

3.1. Surface chemical analysis (XPS)

The difference between the wetting and the dewetting properties can be interpreted by the change in the chemistry of the laser patterned surface before and after vacuum processing [7,16]. Fig. 5A and B corresponds to XPS of plain surface and 4 h vacuum stored laser patterned sample (fluence: 0.86 J/cm^2 and P: 150 μm). This sample is selected as a representative since it demonstrated ultra-hydrophobicity after vacuum process for 4 h. Moreover, the difference in at.% of chemical constituents such as Al, C and O among all the samples are within 10%–15% as shown in Table II. The freshly prepared laser processed samples were hydrophilic and become super/ultrahydrophobic after vacuum processing for 4 h.

The prime constituents of the both XPS spectra are Carbon (C) and Oxygen (O), which are primarily responsible for hydrophilic and hydrophobic properties of laser-patterned surface. The two peaks at 531.6 eV and 285.2 eV corresponds to C 1s and O 1s respectively. The high intensity of C 1s peak in the untreated sample is due to the prolonged exposure of the sample to atmospheric condition. The laser treatment cleans the carbon contamination on the surface by ablation and creates metal oxides due to the reaction with oxygen in the atmosphere. Apart from the two major peaks, the laser-patterned surface has the presence of Al 2s and Al 2p peak at 119 and 74 eV respectively. As the oxides and carbon content determines the wetting property [16] of the laser patterned surface, the deconvolution of peaks are confined to O 1s and C 1s. The deconvolution of the O 1s peak for the plain surface indicates metal oxides, primarily Al$_2$O$_3$ and Al-OH with corresponding binding energies of 531.2 and 532.8 eV respectively [29]. The carbon peak is well pronounced for the plain surface due to the adsorption of airborne contaminants from the atmosphere and the probability of the carbon contamination from vacuum chamber cannot be denied (Fig. 5D). Moreover, this could also be related to the shorter
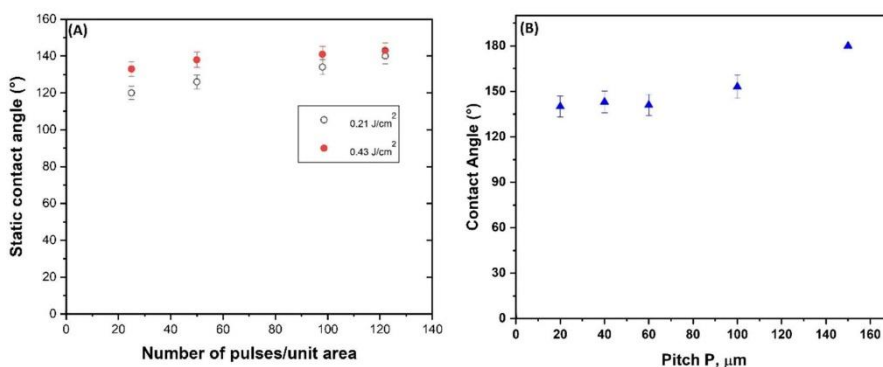

Fig. 4. (A) Static contact angle measurement (SCA) with respect to pulses/spot for the laser fluence of 0.21 and 0.43 J/cm^2. (B). SCA with respect to laser to P for laser fluence of 0.86 J/cm^2 for 240 pulses/spot.
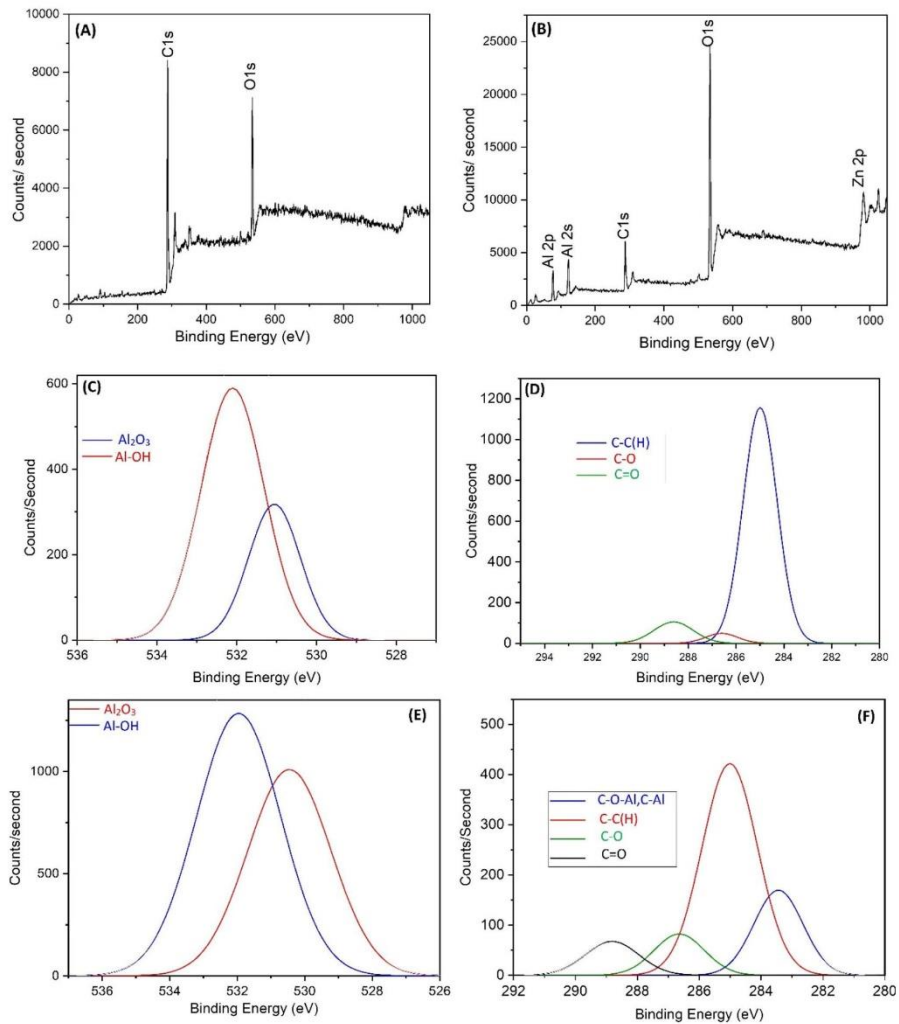
290

Fig. 5. XPS spectra for plain surface (A) and Deconvolution of O 1s and C 1s peaks (C & D); Vacuum processed laser patterned surface (B) and Deconvolution of O 1s and C 1s peaks (E & F).

Table II
The elemental analysis of the laser- patterned Al7075 after 4 h of vacuum processing.

Fluence J/cm^2	Pitch (μm)	No. of pulses/spot	C (at.%)	O (at.%)	Al (at.%)
0.21	20	24	40.29	31.74	14.51
		48	58.63	23.31	10.49
		96	39.18	31.64	19.01
		122	37.04	33.21	19.22
0.43		24	35.99	33.69	17.97
		48	38.26	32.28	18.25
		96	44.74	29.19	17.77
		122	37.64	33.17	19.79
0.86	20	240	26.11	38.12	26.18
	40		31.61	34.91	23.90
	60		33.00	36.57	21.72
	100		26.89	37.52	24.23
	150		26.45	38.8	25.69
Plain surface			70.80	18.77	3.32

penetration depth of photoelectrons, about 7 nm for C 1s compared to 8 nm for Al 2p in XPS analysis [24].

It is apparent that, the passivation of aluminum surface results in thin film of aluminum oxide. There is sharp decrease of C peak (Fig. 5(B)) for the laser patterned samples. This can be related to the surface material removal by ablation process. Further, the creation of micro and nanoscale features exposes pure aluminum to atmosphere at high temperature and it favors the formation of thick layer of Al_2O_3 over the surface structures. The deconvolution peaks for O 1s spectra for the vacuum stored samples results in two peaks, one at 530.3 eV corresponding to O^{2-} and second at 532.8 eV for hydroxyl groups OH^- as well as to the adsorbed organic compounds as carboxylates [30,31]. The high-resolution spectra of C 1s for the vacuum processed samples shown in Fig. 5(F) gives four peaks. The high intense peak at binding energy of 284.7 eV relates to graphitic structure or hydrocarbon chains (C-C(H)). The surface adsorption of ether/alcohols, ketones and carboxyl contribute to the peaks of C−O, C═O and C-C═O at 285.6, 287.5 and 289.6 eV respectively [25]. The polar block comprises metal oxides,
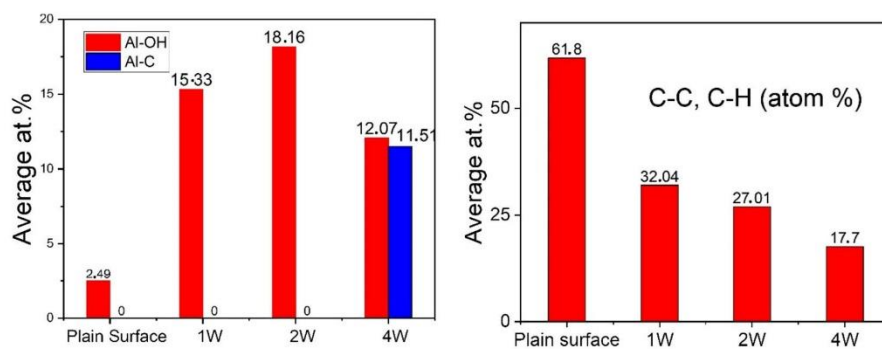
Fig. 6. Relative at.% of Al-OH & Al−C and C−C & C−H bond found from the high-resolution XPS spectra.

carboxyl molecules (O=C-O), carbonyl groups (C=O) and carbon-oxygen (C−O). Whereas, the nonpolar group has hydrocarbon chains (C−C (H)). The dominant presence of C−C (H) together with convenient geometry leads to the ultra and superhydrophobic surfaces.

4. Discussion

The multiscale structure fabrication of metals by ultrafast laser source has three phases: i) Formation of nano and micro scale roughness (precursor sites) ii) Development of precursors to large self-organized structures iii) Growth of self-organized structures [32]. Third phase of growth depends on the fluence value and number of pulses/spot. The nanostructures shown in Figs. 1 and 2 are in second phase of the multiscale structure formation due to the low fluence value and number of laser pulses applied on the surface. The random nanostructures generated by the primary laser pulses transform into micro ripples with the periodicity of 1 μm. Domes start appearing on top of the micro ripple structures as number of pulses reached 96 pulses/spot. The random density of the domes is more prominent for higher fluence values such as 0.43 and 0.86 J/cm^2.

The wetting property of materials depends on the total surface free energy or surface polarity. Depends on the dominance of polar or nonpolar sites on the laser patterned structures, the surface is considered to be wetting or non-wetting. Material removal by the ablation process in ambient conditions generates many fresh Al atoms in the form of Al^{3+} and O^{2-}, subsequently, it creates a passivation layer of Al$_2$O$_3$ on the surface [24]. However, there would be larger amount of unsaturated metallic cation (Al^{3+}) and anions (O^{2-}).Transition metal oxides would be formed due to unsaturated metal and oxygen atoms, which act as Lewis acid and base sites. These coordinately unsaturated cation-anion pairs favor the heterolytic dissociative adsorption of H$_2$O molecules from the atmosphere to stabilize the unsaturation [33]. The hydroxylation of oxide surface is realized by the adsorption of lone pair of O atom of H$_2$O molecule by the cations, so that remaining OH$^-$ is attached to cations and the remaining O is transferred to Lewis base as explained by Jagdheesh et al. [16].

This hydroxylated layer on the surface is prone to wetting by adsorbing second layer of H$_2$O by hydrogen bonding. The significant observation is the formation passive layer (surface hydroxides) on the laser patterned surface due to exposure to atmospheric conditions, which has water molecules. The presence of water molecules delays the development of non-polar hydrocarbons by carbonaceous contamination from airborne hydrocarbons [34,35]. It takes few days to weeks for the transformation of hydrophilic to superhydrophobic surface. However, the presence of surface hydroxyl group is significant for effective adsorption or reaction sites [36,37]. It has been proved that, the presence of hydroxyl group helps in chemisorption of organic molecules from airborne hydrocarbons such as acetic acids and formic acids in the

form of chemisorbed carboxylates [34,38–40]. The relative at.% of Al-OH, Al−C and C-C(H) for the fresh and vacuum processed samples are depicted in Fig. 6. The analysis of the elemental concentration shows there must be a balance between the surface geometry and chemistry to get an extremely water repellent surface.

Super/ultrahydrophobic surface was achieved for the sample processed with *P* value of 100 and 150 μm. The amount of hydrocarbon found in this sample is about 17.7 at.%, which is lower than the other laser processed samples, whereas the unpatterned samples shows a high concentration of hydrocarbons. The poor wetting properties can be related to lack of entrapped air pockets, leading to Wenzel state [28] of wetting behavior. By high vacuum process (Pressure: 10^{-4} Pa), the presence of water vapor is reduced to greater extend (partial water pressure inside the vacuum chamber: 10^{-6} Pa) and it promotes the chemisorption of hydrocarbon molecules inside the vacuum chamber by reducing the passivation of the surface as shown in Eq. (3) [24]. R refers to non-polar chain of C−C (H), which forms an outer layer of nm thickness, thus lowering the surface free energy. The majority of organic contamination comes from the mineral oil (constitute 20% hydrocarbon) which is used for oil rotary pump for the vacuum chamber. This is evident from the higher amount of C at.% (Table II) for those samples stored in vacuum for 4 h. It clearly suggests the predominant presence of non-polar elements reduce the surface free energy, which leads to superhydrophobic character.

$$Al - OH + RCOOH_{(g)} \rightarrow ROOC - Al + H_2O \qquad (3)$$
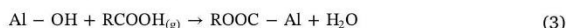
The elemental concentration shown in Table II clearly indicates the high presence of C at.% for all the samples processed for 4 h in high vacuum. Nevertheless, there is a huge difference in SCA across the different geometries and laser process parameters as represented in Fig. 4. The transformation from Wenzel state [28] to Cassie Baxter state [41] requires reliable surface geometry as well as dominant presence of non-polar sites. The surface with lone nanostructure (Fig. 1) recorded a near superhydrophobic (SCA: 130 to 145°) surface for droplet volume of 8 μL. The nanostructures with lack of homogeneity is likely to have lower stability of air-water interface compared to the dual scale microstructures. The observed lower SCA values can be due to the partial penetration of water droplet at the air blanket between the solid and liquid phase. The difference in wetting behavior is caused due to the random spacing of the nanostructures, even the difference in nanometers can induce large variations at the composite interface [42]. Therefore, the hierarchical structure provides a stable and durable superhydrophobic surface for practical applications.

5. Conclusion

The analysis of the surface geometry and chemistry suggests that, synergistic effect of hierarchical surface structures and an overlay of

292

58

non-polar elements is required for superhydrophobic metallic surface. The geometry plays a dominant role for the transformation by entrapping a small volume of air to create a composite interface. Dual scale (micro and nano) microstructures are essential for the durable and consistent superhydrophobic surface with high degree of water repellence. The natural hydrophobic property of air amplifies the apparent contact angle and reduces the fraction solid-liquid contact line, thus providing a non-wetting surface. Further, lone presence of nanoscale structures on inherent hydrophilic metal surface with predominant presence of non-polar elements can only yield near superhydrophobic surface for bigger droplet volume (8 μL), primarily due to random spacing of nanoscale protrusions. The vacuum process provides significant progress in acceleration of chemisorption in few hours compared to the aging technique, which is found to be reproducible with definite time. The laser patterning at atmospheric conditions create large amount of coordinately unsaturated Al-OH reaction sites which promotes the carboxylation by effective adsorption of airborne C-C(H) at short interval of time in very low water vapor pressure. The samples processed with P of 100 and 150 μm pitch exhibited lotus effect and rest of the samples were in rose petal state.

Acknowledgements

References

[1] C. Liu, J. Ju, Y. Zheng, L. Jiang, Asymmetric ratchet effect for directional transport of fog drops on static and dynamic butterfly wings, ACS Nano 8 (2014) 1321–1329.

[2] W. Barthlott, C. Neinhuis, Purity of the sacred lotus, or escape from contamination in biological surfaces, Planta 202 (1997) 1–8.

[3] L. Feng, S. Li, Y. Li, H. Li, L. Zhang, J. Zhai, Y. Song, B. Liu, L. Jiang, D. Zhu, Superhydrophobic surfaces: from natural to artificial, Adv. Mater. 14 (2002) 1857–1860.

[4] V. Zorba, E. Stratakis, M. Barberoglou, E. Spanakis, P. Tzanetakis, S.H. Anastasiadis, C. Fotakis, Biomimetic artificial surfaces quantitatively reproduce the water repellency of a lotus leaf, Adv. Mater. 20 (2008) 4049–4054.

[5] J. Yong, F. Chen, Y. Fang, J. Huo, Q. Yang, J. Zhang, H. Bian, X. Hou, Bioinspired design of underwater superaerophobic and superaerophilic surfaces by femtosecond laser ablation for anti- or capturing bubbles, ACS Appl. Mater. Interfaces 9 (2017) 39863–39871.

[6] S. Choo, H.-J. Choi, H. Lee, Replication of rose-petal surface structure using UV-nanoimprint lithography, Mater. Lett. 121 (2014) 170–173.

[7] R. Jagdheesh, M. Diaz, S. Marimuthu, J.L. Ocaña, Hybrid laser and vacuum process for rapid ultrahydrophobic Ti-6Al-4 V surface formation, Appl. Surf. Sci. 471 (2019) 759–766.

[8] C.-V. Ngo, D.-M. Chun, Laser printing of superhydrophobic patterns from mixtures of hydrophobic silica nanoparticles and toner powder, Sci. Rep. 6 (2016) 36735.

[9] V. Dichiarante, M.I. Martinez Espinoza, L. Gazzera, M. Vuckovac, M. Latikka, G. Cavallo, G. Raffaini, R. Oropesa-Nuñez, C. Canale, S. Dante, S. Marras, R. Carzino, M. Prato, R.H.A. Ras, P. Metrangolo, A short-chain multibranched perfluoroalkyl thiol for more sustainable hydrophobic coatings, ACS Sustain. Chem. Eng. 6 (2018) 9734–9743.

[10] D.-M. Chun, C.-V. Ngo, K.-M. Lee, Fast fabrication of superhydrophobic metallic surface using nanosecond laser texturing and low-temperature annealing, CIRP Ann. 65 (2016) 519–522.

[11] R. Nishimura, K. Hyodo, H. Sawaguchi, Y. Yamamoto, Y. Nonomura, H. Mayama, S. Yokojima, S. Nakamura, K. Uchida, Fractal surfaces of molecular crystals mimicking lotus leaf with Phototunable double roughness structures, J. Am. Chem. Soc. 138 (2016) 10299–10303.

[12] G. Caputo, R. Cingolani, P.D. Cozzoli, A. Athanassiou, Wettability conversion of colloidal TiO2 nanocrystal thin films with UV-switchable hydrophilicity, Phys. Chem. Chem. Phys. 11 (2009) 3692–3700.

[13] L. Wen, Y. Tian, L. Jiang, Bioinspired super-wettability from fundamental research to practical applications, Angew. Chem. Int. Ed. 54 (2015) 3387–3399.

[14] M. Liu, S. Wang, L. Jiang, Nature-inspired superwettability systems, Nat. Rev. Mater. 2 (2017) 17036.

[15] B. Su, Y. Tian, L. Jiang, Bioinspired interfaces with superwettability: from materials to chemistry, J. Am. Chem. Soc. 138 (2016) 1727–1748.

[16] R. Jagdheesh, M. Diaz, S. Marimuthu, J.L. Ocana, Robust fabrication of μ-patterns with tunable and durable wetting properties: hydrophilic to ultrahydrophobic via a vacuum process, J. Mater. Chem. A 5 (2017) 7125–7136.

[17] R. Jagdheesh, B. Pathiraj, E. Karatay, G.R.B.E. Römer, A.J. Huis int'Veld, Laser-induced nanoscale superhydrophobic structures on metal surfaces, Langmuir 27 (2011) 8464–8469.

[18] A. Riveiro, A.L.B. Maçon, J. del Val, R. Comesaña, J. Pou, Laser surface texturing of polymers for biomedical applications, Front. Phys. 6 (2018).

[19] J. Long, P. Fan, D. Gong, D. Jiang, H. Zhang, L. Li, M. Zhong, Superhydrophobic surfaces fabricated by femtosecond laser with tunable water adhesion: from lotus leaf to rose petal, ACS Appl. Mater. Interfaces 7 (2015) 9858–9865.

[20] W. Xu, J. Song, J. Sun, Y. Lu, Z. Yu, Rapid fabrication of large-area, corrosion-resistant superhydrophobic Mg alloy surfaces, ACS Appl. Mater. Interfaces 3 (2011) 4404–4414.

[21] Y. Song, C. Wang, X. Dong, K. Yin, F. Zhang, Z. Xie, D. Chu, J.a. Duan, Controllable superhydrophobic aluminum surfaces with tunable adhesion fabricated by femtosecond laser, Opt. Laser Technol. 102 (2018) 25–31.

[22] H. Yu, Z. Lian, Y. Wan, Z. Weng, J. Xu, Z. Yu, Fabrication of durable super-amphiphobic aluminum alloy surfaces with anisotropic sliding by HS-WEDM and solution immersion processes, Surf. Coat. Technol. 275 (2015) 112–119.

[23] R. Jagdheesh, M. Diaz, J.L. Ocaña, Bio inspired self-cleaning ultrahydrophobic aluminium surface by laser processing, RSC Adv. 6 (2016) 72933–72941.

[24] J.T. Cardoso, A. Garcia-Girón, J.M. Romano, D. Huerta-Murillo, R. Jagdheesh, M. Walker, S.S. Dimov, J.L. Ocaña, Influence of ambient conditions on the evolution of wettability properties of an IR-, ns-laser textured aluminium alloy, RSC Adv. 7 (2017) 39617–39627.

[25] Z. Yang, X. Liu, Y. Tian, Insights into the wettability transition of nanosecond laser ablated surface under ambient air exposure, J. Colloid Interface Sci. 533 (2019) 268–277.

[26] P. Gregorčič, M. Conradi, L. Hribar, M. Hočevar, Long-term influence of laser-processing parameters on (super)hydrophobicity development and stability of stainless-steel surfaces, Materials 11 (2018).

[27] J. Long, M. Zhong, P. Fan, D. Gong, H. Zhang, Wettability conversion of ultrafast laser structured copper surface, J. Laser Appl. 27 (2015) S29107.

[28] R.N. Wenzel, Resistance of solid surfaces to wetting by water, Ind. Eng. Chem. Res. 28 (1936) 988–994.

[29] G.P. López, D.G. Castner, B.D. Ratner, XPS O 1s binding energies for polymers containing hydroxyl, ether, ketone and ester groups, Surf. Interface Anal. 17 (1991) 267–272.

[30] K.W. Wulser, M.A. Langell, Carboxylic acid adsorption on NiO(100) characterized by X-ray photoelectron and high resolution electron energy loss spectroscopies, Catal. Lett. 15 (1992) 39–50.

[31] S.A. Isa, R.W. Joyner, M.H. Matloob, M.W. Roberts, A study of the interaction of formic acid and propionic acid with oxidised lead and copper surfaces by photoelectron spectroscopy and LEED, Appl. Surf. Sci. 5 (1980) 345–360.

[32] C.A. Zuhlke, T.P. Anderson, D.R. Alexander, Formation of multiscale surface structures on nickel via above surface growth and below surface growth mechanisms using femtosecond laser pulses, Opt. Express 21 (2013) 8460–8473.

[33] H.H. Kung, Transition Metal Oxides: Surface Chemistry and Catalysis, 1st ed., Elsevier, 1989.

[34] M. Psarski, J. Marczak, J. Grobelny, G. Celichowski, Superhydrophobic surface by replication of laser micromachined pattern in epoxy/alumina nanoparticle composite, J. Nanomater. 2014 (2014) 11.

[35] A. Glisenti, G. Favero, G. Granozzi, Reactivity of simple alcohols on Fe2O3 powders an XPS and FTIR study, J. Chem. Soc. Faraday Trans. 94 (1998) 173–182.

[36] J.B. Peri, R.B. Hannan, Surface hydroxyl groups on γ-Alumina1, J. Phys. Chem. 64 (1960) 1526–1530.

[37] H.P. Boehm, Acidic and basic properties of hydroxylated metal oxide surfaces, Discuss. Faraday Soc. 52 (1971) 264–275.

[38] Z. Li, Y. Zheng, J. Zhao, L. Cui, Wettability of atmospheric plasma sprayed Fe, Ni, Cr and their mixture coatings, J. Therm. Spray Technol. 21 (2012) 255–262.

[39] J. van den Brand, S. Van Gils, P.C.J. Beentjes, H. Terryn, J.H.W. de Wit, Ageing of aluminium oxide surfaces and their subsequent reactivity towards bonding with organic functional groups, Appl. Surf. Sci. 235 (2004) 465–474.

[40] H. Knözinger, P. Ratnasamy, Catalytic aluminas: surface models and characterization of surface sites, Catal. Rev. Sci. Eng. 17 (1978) 31–70.

[41] A.B.D. Cassie, S. Baxter, Wettability of porous surfaces, Trans. Faraday Soc. 40 (1944) 546–551.

[42] A. Elbourne, M.F. Dupont, S. Collett, V.K. Truong, X. Xu, N. Vrancken, V. Baulin, E.P. Ivanova, R.J. Crawford, Imaging the air-water interface: characterising biomimetic and natural hydrophobic surfaces using in situ atomic force microscopy, J. Colloid Interface Sci. 536 (2019) 363–371.

5.2 Journal letter B. Nanostructure fabrication on the top of laser-made micropillars for enhancement of water repellence of aluminium alloy

In this letter, a two-step method for fabrication of superhydrophobic surface structures with common nanosecond fibre laser was developed. In the first step, well-defined melt-free micropillars were fabricated followed by a second step with a defocused laser beam to introduce nanoscale protrusions on the top of micropillars. To enhance water repellency and to shorter the transformation time, vacuum processing technique was used. It was demonstrated that wettability of the surface can be tuned by hatch distance, defocusing distance and a number of pulses per focal spot.

Author contribution

In work related to the production of this journal letter the author planned, designed and carried out all experiments. The author also analysed SEM data with J. Kopeček and XPS data with P. Jiříček. The author was responsible for data interpretation, drafting the manuscript and communication with the journal. Detail authors individual contributions are shown in table 2.

Term	Authors' individual contributions
Conceptualization	P. Hauschwitz
Methodology	P. Hauschwitz
Software	P. Hauschwitz
Validation	R. Jagdheesh, P. Hauschwitz, D. Rostohar
Investigation	P. Hauschwitz
Resources	T. Mocek, J. Houdková, J. Brajer, J. Kopeček, P. Jiříček
Writing - Original Draft	P. Hauschwitz
Writing - Review & Editing	R. Jagdheesh, P. Hauschwitz, D. Rostohar, J. Brajer
Visualization	P. Hauschwitz
Supervision	R. Jagdheesh, J. Brajer, D. Rostohar
Project administration	Petr Hauschwitz, Jan Brajer
Funding acquisition	T. Mocek

Table 2: Credit author statement - Nanostructure fabrication on the top of laser-made micropillars for enhancement of water repellence of aluminium alloy

Nanostructure fabrication on the top of laser-made micropillars for enhancement of water repellence of aluminium alloy

P. Hauschwitz [a,c,*], R. Jagdheesh [a], D. Rostohar [a], J. Brajer [a], J. Kopeček [b], P. Jiříček [b], J. Houdková [b], T. Mocek [a]

[a] Hilase Centre, Institute of Physics, Academy of Sciences of the Czech Republic, Za Radnici 828, Dolni Brezany 25241, Czech Republic
[b] Institute of Physics of the Czech Academy of Sciences, Na Slovance 2, Prague, Czech Republic
[c] Faculty of Nuclear Sciences and Physical Engineering, Czech Technical University in Prague Brehova 7, 115 19 Prague, Czech Republic

ABSTRACT

Fabrication of superhydrophobic surfaces is a popular topic in research and industry due to many potential applications including self-cleaning, anti-icing or drag reduction. Laser micro and nanostructuring is an efficient method to replicate lotus leaves double-scale structures to achieve superhydrophobicity without chemical treatment. Immediately after laser processing, samples are hydrophilic and become hydrophobic in a few days, exposed to atmospheric conditions. This time was significantly reduced by vacuum processing to only 4 h. Two-step fabrication method of superhydrophobic surfaces have been developed using nanosecond laser system. In the first step, large scale micropillars are fabricated and covered by nano-scale protrusions in the following step using defocused laser beam. The nanostructure formation increased the apparent contact angle from 149° to 175°.

© 2019 Elsevier B.V. All rights reserved.

1. Introduction

Extremely water repellent surfaces can be originally found in the nature, such as famous lotus leaf, covered with dual-scale micro and nanostructures [1]. Synergic effect of micropillars covered with nanostructures is responsible for very high contact angles together with minimal sliding angles [2]. Surfaces with high apparent contact angle and high roll off angle is termed as "rose petal effect" while surfaces with high contact angle and low roll off angle is termed as "lotus effect" [3]. Inspired by the lotus leaf dual-scale structures, laser surface texturing offers a non-polluting and flexible method for fast and efficient fabrication of micro and nanostructures on the top surface layer [4]. However, freshly prepared laser patterned sample is hydrophilic due to the formation of metal oxide layer on the top of the geometries and it takes several days to weeks for the development of perfect non-wetting surface [5]. In this study, two-step nanosecond laser fabrication of dual-scale (micro and nano) geometry is applied for superhydrophobic surface fabrication on aluminium alloy 7075, which is widely used in defence and aerospace industry due to high strength-to-weight ratio, machinability and relatively low cost [6]. The wettability properties are studied with respect to surface geometry and surface chemistry of laser patterned vacuum stored aluminium sample.

2. Materials and methods

Aluminium alloy 7075 plates were used as received (Ra $\sim$ 0.45 μm) for nanosecond laser processing (Ytterbium fiber laser Omron MX-MI20B, λ: 1062 nm, 3 ns). Tightly focussed and defocussed beam was used to create micro and dual scale (micro and nano) structures. In both cases, laser was operated at 200 kHz repetition rate with a power of 9 W. The scanning head (intelliSCAN 30, Scanlab) with 163 mm F-theta lens has been used for the patterning over the sample with a scan speed of 700 mm/s in a rectangular grid path with a hatch distance (*HD*) in the rage of 0.5 to 50 μm and up to 50 overscans (*N*). Primarily, μ-pillars were fabricated with the in-focus laser beam of 39 μm spot diameter and 50 μm hatch distance. Subsequently, defocused beam was applied to introduce nano-scale features on the top of these micropillars. Immediately after laser treatment, samples were placed for 4 h into high vacuum ($5 \cdot 10^{-6}$ Pa) to promote favourable chemical changes to enhance water repellency in a short time [7]. The surface wettability was evaluated by the Sessile drop technique with a droplet size of 10 μl as an average of 10 measurements on different regions using optical contact angle measurement device OCA 15EC (Data Physics Instruments). The geometry of fabricated structures was investigated with a scanning

* Corresponding author at: Hilase Centre, Institute of Physics, Academy of Sciences of the Czech Republic, Za Radnici 828, Dolni Brezany 25241, Czech Republic.
E-mail address: petr.hauschwitz@hilase.cz (P. Hauschwitz).

electron microscope (SEM) Tescan FERA 3 and laser scanning con-focal microscope Olympus OLS5000. Surface chemistry was anal-ysed by X-ray photoelectron spectroscopy (XPS) performed at the AXIS Supra photoelectron spectrometer (Kratos Analytical Ltd.).

3. Results and discussion

In the first step, focused laser beam with the fluence of 2.51 J/cm^2 and HD of 50 μm was used to fabricated 40-μm high μ-pillars. The top surface of the μ-pillars was covered with a recast

layer. The thick layer of recast is the result of melt ejection as well as redeposition of metal vapour (Fig. 1a). The wettability of such surface was evaluated after storing the sample in atmospheric con-ditions for 30 days and in high vacuum (5·10^{-6} Pa) for 4 h. The maximum contact angle of 138° and 149° was reached for atmo-spheric and vacuum stored sample respectively. The lack of dual scale geometry improves the wetting property to near superhy-drophobic with a roll of angle higher than 90°, leading to rose petal effect [3]. To enhance water repellence and improve high roll off angle, the μ-pillars were subjected to defocussed laser scans imme-
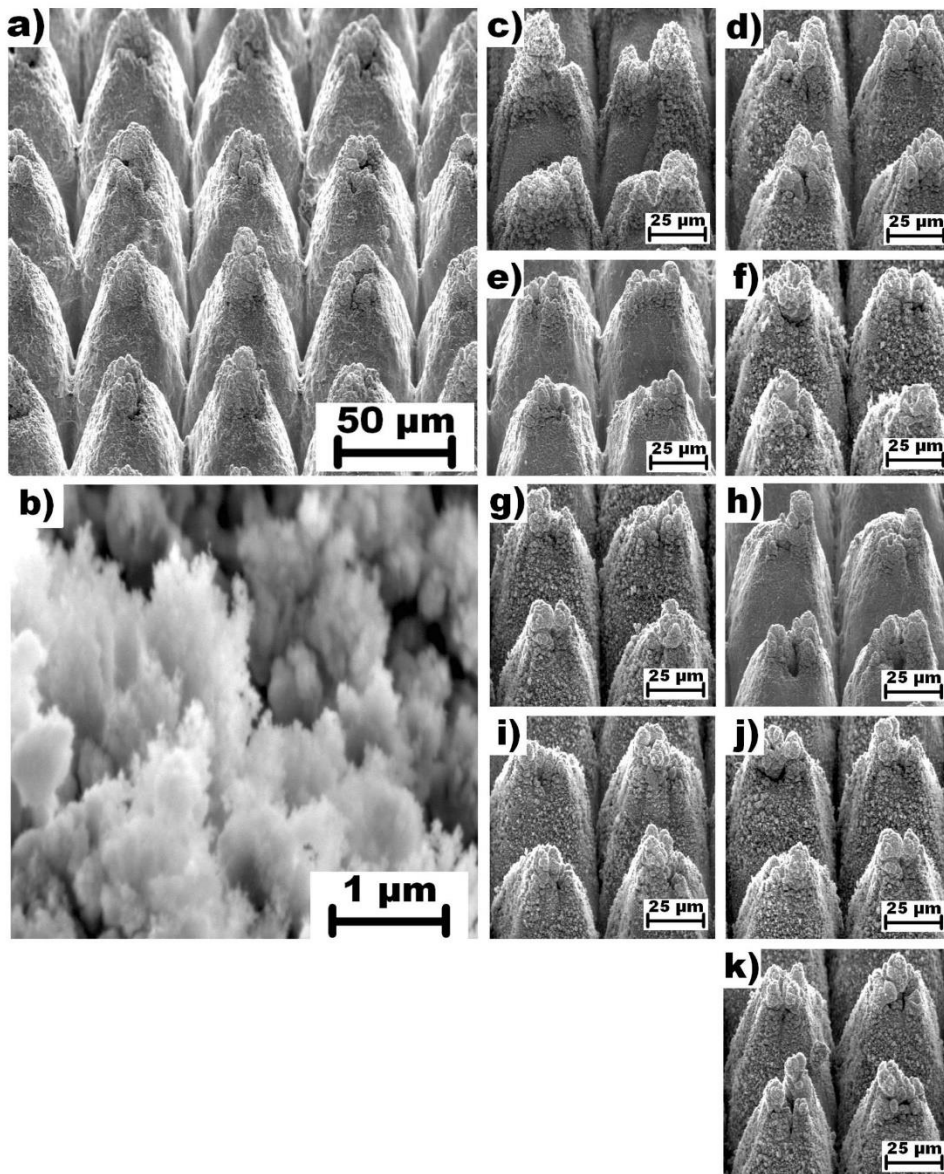
Fig. 1. Fabricated structure geometries before (a) and after (b-k) second fabrication step with defocused beam. b) high magnification image of the foam-like nanostructures. The second step parameters: c) d = 1 mm, HD = 1 μm, N = 1; d) d = 2 mm, HD = 1 μm, N = 1; e) d = 3 mm, HD = 1 μm, N = 14; f) d = 2 mm, HD = 0.5 μm, N = 1; g) d = 2 mm, HD = 5 μm, N = 1; h) d = 2 mm, HD = 20 μm, N = 1; i) d = 2 mm, HD = 1 μm, N = 2, j) d = 2 mm, HD = 1 μm, N = 10; k) d = 2 mm, HD = 1 μm, N = 40.

diately after their fabrication. In this case, beam was defocused to a distance (d) within the range of 1–3 mm from the focal point of the sample. The defocused scans introduce a layer of nanoscale protrusions on the top μ-pillars as can be observed in Fig. 1b. The growth of these foam-like nanoscale protrusions was analysed with respect to d, N and HD.

It can be clearly distinguished that defocusing distance and hatch distance has the major effect on the amount of nanoscale protrusions. As can be observed from the Fig. 1c-e, higher amount of melting occurs on the top of micropillars for 1 mm defocusing distance. Moreover, the top surface of micropillars is covered with nanoscale protrusions. For higher defocusing distance (d = 2 mm), nanoscale protrusions are homogeneously distributed over the whole micropillars surface, as can be noticed in Fig. 1d. Contrarily, if the defocusing distance is ≥3 mm, the second fabrication step has no effect on the topography and no melting or nanostructures are observed (Fig. 1e). These observations are directly connected with wettability results shown in Fig. 2, where the contact angle is increasing with defocusing distance up to the maximum of 170° for d = 2 mm and then it falls sharply down to the contact angle of 154° for d = 3 mm, which is still slightly above the value for sample surface before defocusing in the second fabrication step. Moreover, by introducing the nanoscale features on the top of micropillars, roll-of-angle was significantly reduced from strongly pinned down rose petal state to highly water-repellent lotus effect with sliding angle as small as 1° (d = 1.4 mm).

By changing the hatch distance, the amount of nanoscale features can be changed significantly. The higher density of nanoscale protrusions is observed for the lowest hatch distance of 0.5 μm

(Fig. 1f). This surface reaches the maximum contact angle of 175° together with sliding angle of 2°. The nanoscale features start disappearing with increasing hatch distance, and they are not visible for HD over 20 μm (Fig. 1h). In addition, contact angle is decreasing down to 162° for 20 μm hatch distance, which is high above the value for sample surface before the defocusing. Comparing Fig. 1i–k, different number of overscans have minimal effect on surface topography. However, contact angle is increasing rapidly up to 10 overscans and then it saturates on the value around 174°.

When contact angle is increasing due to higher amount of nanoscale features, sliding angle decreases resulting in the lotus effect. In all cases, it was possible to reach sliding angles below 2°. The wetting property analysis suggests that, the pressure resistance offered by the nanostructures for liquid penetration is much higher than the microstructures [8].

The importance of vacuum processing for wettability results can be elucidated by the surface chemistry analysis. As explained by Jagdheesh [7], the dominant presence of non-polar hydrocarbons together with convenient geometry is responsible for superhydrophobic behaviour of aluminium sample stored in high vacuum conditions after laser treatment. Therefore, deconvolution of XPS photoelectron spectra was confined to hydrocarbon peaks (C–C, C–H), as depicted in Fig. 3.

As can be clearly noticed, the amount of hydrocarbons is directly connected with wettability results. The lowest at% of hydrocarbons have the samples measured 2 h after laser treatment which are hydrophilic, followed by sample exposed to atmospheric conditions for 30 days. The highest contact angle and amount of hydrocarbons, forming the low surface energy layer, have the vac-
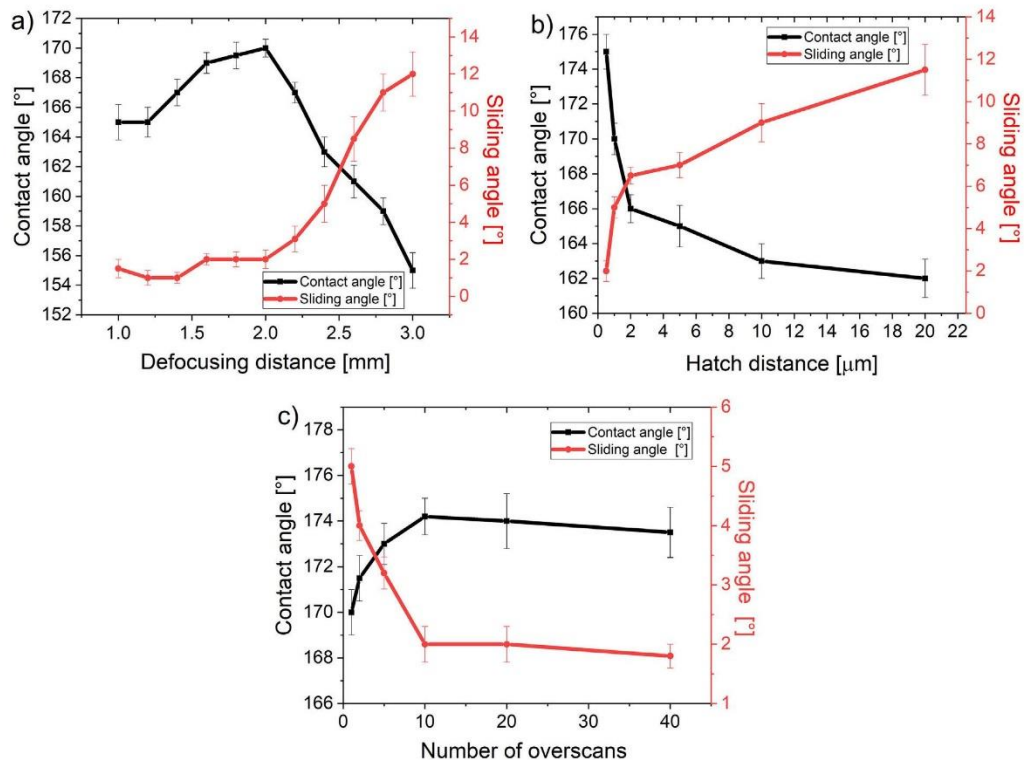

Fig. 2. Wettability results for two-step laser processed vacuum stored samples in a dependence on: (a) defocusing distance d for HD = 1 μm, N = 1; (b) Hatch distance HD for d = 1 mm. N = 1; (c) Number of overscans N for d = 1 mm, HD = 1 μm.
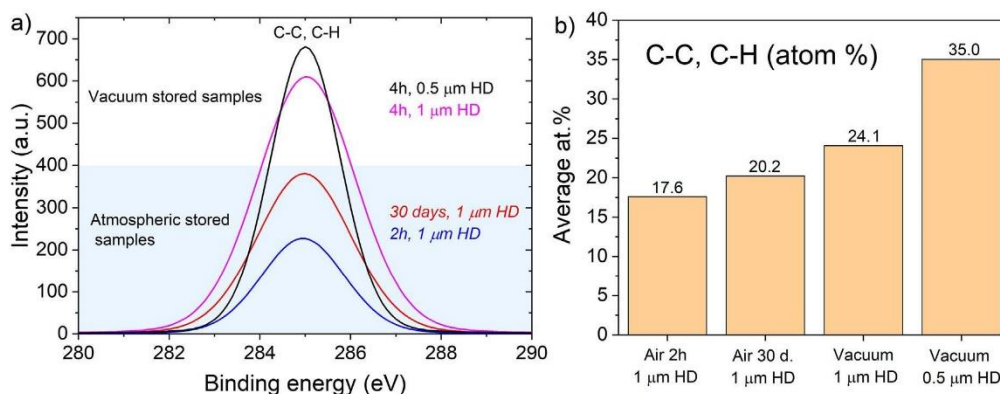
Fig. 3. Photoelectron spectra of laser treated samples (d = 1 mm, N = 1 mm) stored in the atmospheric conditions and vacuum conditions (a). Corresponding average at% of C–C and C–H (b).

uum stored samples with the maximum of 35 at% for the sample processed with HD of 0.5 μm in the second fabrication step with defocused beam.

4. Conclusion

Two-step fabrication process with nanosecond laser source followed by vacuum processing can significantly enhance water repellence in short interval of time compared to aging in atmospheric conditions. The introduction of layer of nanoscale structures improves the wetting state from rose petal to lotus effect with high static contact angle and low roll off angle. The amount of nanoscale protrusions and the hydrocarbon contamination is directly connected with the wettability results. The wetting states can be manipulated by the defocusing distance of beam, hatch distance and number of overscans.

Declaration of Competing Interest

The authors declare that they have no known competing financial interests or personal relationships that could have appeared to influence the work reported in this paper.

Acknowledgements

References

[1] K. Liu, X. Yao, L. Jiang, Recent developments in bio-inspired special wettability, Chem. Soc. Rev. 39 (8) (2010) 3240–3255.
[2] B. Bhushan, Y.C. Jung, K. Koch, Micro-, nano-and hierarchical structures for superhydrophobicity, self-cleaning and low adhesion, Philos. Trans. Royal Soc. A 367 (1894) (2009) 1631–1672.
[3] R. Jagdheesh, M. Diaz, S. Marimuthu, J.L. Ocana, Robust fabrication of μ-patterns with tunable and durable wetting properties: hydrophilic to ultrahydrophobic via a vacuum process, J. Mater. Chem. A 5 (15) (2017) 7125–7136.
[4] F.H. Rajab, Z. Liu, L. Li, Long term superhydrophobic and hybrid superhydrophobic/superhydrophilic surfaces produced by laser surface micro/nano surface structuring, Appl. Surf. Sci. (2018).
[5] A.-M. Kietzig, S.G. Hatzikiriakos, P. Englezos, Patterned superhydrophobic metallic surfaces, Langmuir 25 (8) (2009) 4821–4827.
[6] T. Dursun, C. Soutis, Recent developments in advanced aircraft aluminium alloys, Mater. Des. 56 (2014) 862–871.
[7] R. Jagdheesh, P. Hauschwitz, J. Mužík, J. Brajer, D. Rostohar, P. Jiříček, J. Houdkova, J. Kopeček, T. Mocek, Non-fluorinated superhydrophobic Al7075 aerospace alloy by ps laser processing, Appl. Surf. Sci. (2019).
[8] R. Hensel, C. Neinhuis, C. Werner, The springtail cuticle as a blueprint for omniphobic surfaces, Chem. Soc. Rev. 45 (2) (2016) 323–341.

5.3 Journal article C. Fabrication of Functional Superhydrophobic Surfaces on Carbon Fibre Reinforced Plastics by IR and UV Direct Laser Interference Patterning

Carbon fibre reinforced composites are lightweight materials of the future for many industrial applications, but also difficult to process. This joint publication with Fraunhofer Institute for Material and Beam Technology demonstrates the capability of interference patterning for rapid large-scale microstructuring and surface functionalization of CFRP for the first time in literature.

In this journal paper, an interference processing technique has been applied in order to produce hierarchical microstructures in a single step with the use of commercial nanosecond laser systems, despite vastly different optical and thermal properties of matrix and carbon fibres. The analysis of surface geometry and wettability concludes that DLIP is a suitable tool for fast functionalization of CFRP.

Author contribution
In work related to the production of this journal paper, P. Hauschwitz planned, designed and carried out all experiments with the help and supervision of S. Alamri and T. Kunze. P. Hauschwitz also analysed SEM data with J. Kopeček and interpreted data with the help of R. Jagdheesh. P. Hauschwitz was responsible for drafting the manuscript and communication with the journal. Detail authors individual contributions are listed in table 3.

Term	Authors' individual contributions
Conceptualization	P. Hauschwitz, S. Alamri, D. Rostohar, T. Kunze
Methodology	P. Hauschwitz, S. Alamri, T. Kunze
Software	P. Hauschwitz,
Validation	S. Alamri, P. Hauschwitz, R. Jagdheesh, T. Kunze
Investigation	P. Hauschwitz
Resources	T. Kunze, J. Kopeček, P. Jiříček
Writing - Original Draft	P. Hauschwitz
Writing - Review & Editing	R. Jagdheesh, P. Hauschwitz, S. Alamri, D. Rostohar, T. Kunze, J. Brajer
Funding acquisition	T. Mocek

Table 3: Credit author statement - Fabrication of Functional Superhydrophobic Surfaces on Carbon Fibre Reinforced Plastics by IR and UV Direct Laser Interference Patterning

Full Length Article

Fabrication of functional superhydrophobic surfaces on carbon fibre reinforced plastics by IR and UV direct laser interference patterning

P. Hauschwitz[a,d,*], R. Jagdheesh[a], S. Alamri[c], D. Rostohar[a], T. Kunze[c], J. Brajer[a], J. Kopeček[b], T. Mocek[a]

[a] Hilase Centre, Institute of Physics, Academy of Sciences of the Czech Republic, Za Radnici 828, Dolni Brezany 25241, Czech Republic
[b] Institute of Physics of the Czech Academy of Sciences, Na Slovance 2, Prague, Czech Republic
[c] Fraunhofer-Institut für Werkstoff- und Strahltechnik IWS, Winterbergstraße 28, 01277 Dresden, Germany
[d] Faculty of Nuclear Sciences and Physical Engineering, Czech Technical University in Prague Brehova 7, 115 19 Prague, Czech Republic

ARTICLE INFO

ABSTRACT

The fabrication of functional microstructures on surfaces by laser enables unique material properties and is presently a leading research topic. This work addresses the production of functional hierarchical microstructures on carbon fibre reinforced polymer composites in order to control the wettability properties of the material. Two-beam Direct Laser Interference Patterning using either ultraviolet (263 nm) or infrared (1053 nm) nanosecond laser source is employed to produce melt-free and well-defined hierarchical microstructures on carbon fibre reinforced plastics. The resulting water contact angles after thin film deposition of 1H,1H,2H,2H-Perflorodecyl-triethoxysilane were analysed with respect to structure depth and quality. The maximum static contact angle of 171° is demonstrated for dual hierarchical microstructures composed of 11 μm deep large-scale pillars, covered by 1.7 μm pillars, both fabricated in a single step.

1. Introduction

Composite materials, made by the combination of two or more synergic micro-constituents, have been used in a wide range of applications in space and aviation, automotive, maritime and manufacturing of sports equipment. Carbon fibre reinforced plastics (CFRP), in which carbon fibres are used as the reinforced element in a polymer matrix, have been used for production of various aircraft components involving both small components such as doors and clips as well as wing flaps and the main body [1]. The use in such demanding applications is correlated with the CFRP superior characteristics such as high strength and stiffness, low weight and high fatigue resistance [2]. Nevertheless, the CFRP application in many cases is limited by the machinability, while the conventional machining can result in fibre rapture, resin fibre debonding, micro-crack formation and tool wear. Additionally, to the demanding quality criterions, high processing rates are necessary to meet industrial requirements [3].

Besides the numerous research activities which focus on replacing metals with CFRP in production of critical components for weight reduction in aircraft applications, additional challenges such of anti-icing of surfaces and de-icing are still unsolved [4]. Consequently, there is a strong need for efficient anti-icing strategies, which exhibit the

potential to be applied on large-areas and with high processing speeds. One of the most promising ways is surface functionalisation by means of surface micro-texturing [5–9].

A large number of fabrication methods for surface functionalisation have been used including microreplication [10], lithography [11], electrodeposition [12], sol-gel [13], chemical etching [14] and thermal embossing [15]. Among these techniques, laser beam micro-machining, and in particular Direct Laser Writing (DLW), has been recognized as an excellent option for the processing of materials including CFRP [3] especially when short and ultra-short laser pulses are used. DLW allows the fabrication of complex surface structures in a single-step process through a non-contact, automatable and eco-friendly approach. Although the fabrication of functional surfaces has been demonstrated on different materials [16–22], the main drawback of the traditional DLW technology is the long processing time with machining speeds in the range of minutes per square centimetre [6,20,23]. Multiple solutions are available for scaling-up the fabrication speed of DLW including the use of polygonal scanners [24] and multi-beam approaches [25]. However, the achievable feature sizes of DLW are typically limited to 5–15 μm [26–28].

In recent years, Direct Laser Interference Patterning (DLIP) has become a fast and efficient way for laser micro-processing [29,30]. In this

method, the interference pattern created by the coherent overlap of two or more laser beams is directly imposed on the material. The geometry of the interference pattern can be controlled by the number of laser beams and their incidence angle as well as by wavelength, polarization, intensity and phase difference of these beams [31]. For two-beam interference, the spatial period Λ is given by $\Lambda = \lambda/2\sin\Theta$, where λ is the wavelength of the used laser light and Θ is the half angle between the two incident beams. The intensity distribution of the generated interference pattern follows the intensity distribution of the main laser beam which, in the case of laser emitting a TEM00 mode, results in a sinusoidal wave modulated by a Gaussian envelope. If properly controlled, this non-uniform intensity distribution in the interference area allows fabricating complex surface structures, as demonstrated by Alamri et al. [32]. Even though DLIP has been effectively implemented for polymer micro-machining [33–36], in the case of CFRP, the fabrication of functional microstructures presents more challenges, due to its heterogeneous composition with the vastly different optical and thermal properties of its micro-constituents. So far, there is no solution for laser microtexturing of functional superhydrophobic surfaces on CFRP, which would be the first step for anti-icing CFRP surface. Moreover, DLIP technique provides the operational window to create surface geometries with spatial periods of few microns, which effectively reduces the fractional area of contact between the solid and liquid phases by trapping more volume of air inside the micro voids.

In this work, carbon fibre reinforced composite samples with a polyether ether ketone matrix were employed due to their superior properties and broad applications in the aerospace, aircraft and automobile industry [37]. The DLIP technology has been selected as the most efficient laser-based method for achieving optimized wettability properties by the realization of functional hierarchical microstructures [30]. After the DLIP-processing, the surfaces have been coated with 1H,1H,2H,2H-Perflorodecyl-triethoxysilane in order to decrease the surface energy and enhance the water repellence effect. The wetting properties are investigated by static water contact angle measurements, taking into account the geometry and quality of the fabricated microstructures.

2. Experimental

2.1. Material

C-PEEK samples consisting of polyether ether ketone matrix and unidirectional carbon fibres T700 by TenCate with standard modulus and volume of 59% were cleaned with ethanol and used as received for the laser patterning experiments. The CFRP samples have unidirectional fibres and therefore the interference pattern with respect to the sample orientation was carefully considered. All samples were processed in the perpendicular direction to the carbon fibres, which allows to produce micro-pillars without rotating the sample.

2.2. DLIP and post process treatments

All the samples were processed with nanosecond DPSS lasers, namely a TECH-1053 Basic (λ = 1053 nm) and TECH-263 Advanced (λ = 263 nm) by Laser-export Co. Ltd (Russia). For the DLIP setup, a compact optical module (developed at Fraunhofer IWS Dresden) was used which is capable to fabricate line-like interference patterns with varying spatial periods. The main laser beam is divided into two sub-beams by a diffractive beam-splitting element. The two sub-beams are collimated by a prism and then overlapped by a lens onto the sample surface resulting in a line-like interference pattern in a well-defined interference area (denoted as DLIP pixel), as depicted in Fig. 1. By changing the distance between the beam-splitting element and the prism, the interference period Λ can be selectively changed in a range of 2–8.5 μm for the IR and 1.5–11 μm for the UV module. The size of the DLIP-pixels in the working position is around 70 μm and 25 μm for the
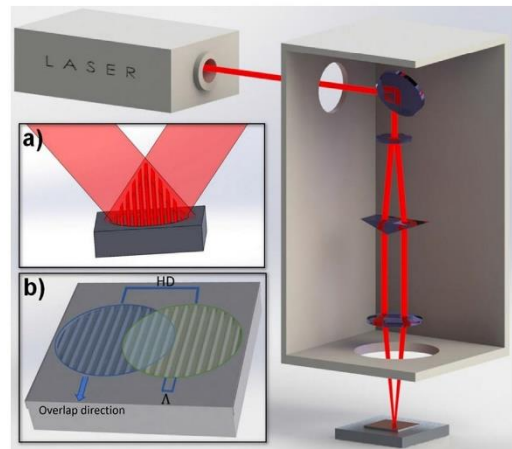

Fig. 1. Schematic of interference processing head at Fraunhofer IWS with inserts of: (a) schematic illustration of the interference pattern of two overlapping laser beams, (b) illustration of hatch distance (HD), overlap direction and interference period Λ on two interference spots.

IR and UV laser, respectively. Precision positioning stages AEROTECH PRO115 were used for displacing the sample and distributing the interference pattern over a larger area both in the parallel and perpendicular direction to the interference pattern, as highlighted in Fig. 1. It is worth mentioning that the Hatch Distance (HD) value have been adjusted for the employed spatial period, in order to match a distance equal to an entire multiple of the period. The detailed process parameters are listed in Table 1.

By taking into account that C-PEEK sample contains fibres in the surface-near layer, as well as very different optical and thermal properties of the fibres and polymer matrix, the fabrication of structures in micrometre range with ns pulses lasers was only possible by removing the top-most polymer layer and subsequent structuring of the fibres underneath. This technique can be applied even for IR radiation where most of the polymers are transparent for ns-laser treatments [38]. After DLIP treatment, the structured samples were kept in an oven for 1 h to introduce a thin layer of 1H,1H,2H,2H-Perflorodecyl-triethoxysilane by chemical vapour deposition (CVD) in order to decrease surface energy and enhance water repellency.

2.3. Measurement of surface wetting properties

The wettability of samples was evaluated by optical contact angle measurement device OCA 15EC (Data Physics Instruments) as an average of 5 measurements on different areas of the laser-treated samples using sessile drop technique and deionized water with a droplet size of 8 μl. Wettability measurements were performed prior to

Table 1
Laser and processing parameters.

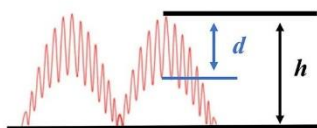|	IR	UV
Wavelength [nm]	1053	263
Pulse duration [ns]	15	4
Repetition rate [kHz]	1	1
Power [mW]	54, 110	10
Fluence [J/cm²]	1.4, 2.9	2.0
Interference area [μm]	70	25
Overlap [%]	> 98	> 90
Number of pulses per unit area	200–1200	10–200
Hatch distance [μm]	~60	~17

Fig. 2. Illustration of double-scale hierarchical structure composed of small-scale micropillars (depth *d*), generated by DLIP processing on the top of large-scale micropillars (depth *h*), produced by the Gaussian modulation of each DLIP pixel.

microscopy analysis to minimize the risk of spoiling the sample surface during sample handling and analysis.

2.4. Surface morphology and depth measurements

The surface morphology and depth of microstructures were investigated with a scanning electron microscope (SEM) Tescan FERA 3 at electron energy of 0.5 kV and laser scanning confocal microscope (LSCM) Olympus OLS5000. The depth of hierarchical structures (Fig. 2) is averaged over more than 30 individual measurements at different locations in the patterned area.

3. Results and discussion

3.1. IR-DLIP processing

The laser ablation with pulses in the nanosecond regime is considered primarily as a photo-thermal process. Nanosecond pulses rapidly heat the carbon fibres directly due to low IR absorption of the PEEK matrix [38]. Heat is then transferred by the fibres to the surrounding area, consequently leading to melting and ultimately vaporization of the polymer matrix around the heated fibres. Therefore, in a first set of single-beam ablation experiments (without DLIP), high pulse to pulse overlaps in a combination with a very low laser power have been used in order to completely removal from the top surface layer the polymer matrix. In particular, the optimal laser fluence for a homogeneous ablation has been identified between 1.3 and 1.6 J/cm^2, corresponding to a laser power of 50 – 60 mW. For laser fluences above 1.6 J/cm^2, cracking of the fibres was observed (results not shown). These fibres then protrude above the surface, decreasing surface flatness and homogeneity and shielding the surface underneath from laser radiation. Below 1.43 J/cm^2, the polymer top surface layer cannot be completely removed from the target area. As a consequence of the first set of single-beam ablation experiments, samples have been pre-processed with IR-radiation with a fluence of 1.43 J/cm^2 (with a single laser beam) in order to assure the complete polymer removal without affecting the fibre structure.

After the pre-processing, the surfaces have been treated by 2-beam interference with IR radiation and microstructures with spatial periods between 2.0 and 8.5 μm could be generated directly on the fibres using different laser fluences. By aligning the DLIP pattern perpendicular to the unidirectional fibres, selective ablation occurs which ultimately lead to surface microstructures with pillar-like shapes, as depicted in Fig. 3a–c. The depths *d* of the microstructures range between 0.5 and 7 μm, mostly depending on the employed spatial period and number of pulses per unit area at the used laser fluence of 1.4 J/cm^2, as shown in Fig. 4. The largest structure depths of about 7 μm can be produced using the higher spatial period of 8.5 μm and a large number of pulses per unit area which results in microstructures with aspect ratios of 0.8. Note that the aspect ratio is calculated by structure depth over spatial period.

As described in Section 1, the employed laser sources emits a TEM$_{00}$ beam profile (Gaussian shape), thus the intensity in the middle of the beam distribution is higher than at its edge. Together with an interference pattern, this "Gaussian modulation" is impressed on the ablated

material, reproducing this profile within the DLIP-pixel. Such modulation is more pronounced for the small spatial periods and has not been observed for larger periods of 4.3 μm and 8.5 μm.

However, a higher number of pulses lead to larger heat input which result in structure cracking and damage, as shown in Fig. 3d–f.

To further tune the surface structures, a different fluence regime between 2.6 and 2.9 J/cm^2 was considered. Since the centre of the DLIP pixel has a higher power density, the Gaussian-shaped modulation can be enhanced and double-scale hierarchical structures could be obtained on the fibres, having large pillars (generated by the size of the DLIP pixel) and small-scale pillars (generated by the interference lines), using a hatch distance of 60 μm and orienting the interference lines perpendicular to the fibres orientation, as depicted in Fig. 5.

The modulation of the interference pattern with a Gaussian distribution is visible for all the periods and pulses per unit area. Stair-like structures are formed for the 8.5 μm period, as shown in Fig. 5f. The average width of the larger micropillars is 44 ± 10 μm in the direction of the fibres and 40 ± 7 μm in perpendicular direction, while the smaller micropillars are always determined by the fibre diameter of 5 μm in one direction and by the spatial period in the direction perpendicular to the fibre axis. By decreasing, the spatial period to 4.3 μm, the unselective ablation is accentuated, forming deep channels between the pillar-on-pillar structures shown in Fig. 5e. The measured average width for these structures is 42 ± 13 μm in the fibre direction and 36 ± 5 μm in the perpendicular direction, both covered with 4.3 μm micropillars. Note that the topography for the 2 μm period is very similar to the low power case, as described above. Their average width is 33 ± 5 μm and 40 ± 4 μm in the fibre and the perpendicular direction, respectively, and are covered with more cracks for a higher number of pulses per unit area compared to the low power treatment. The different dimensions of produced structures in one direction and in the perpendicular one can be assigned to fiber bunches distribution, different fiber depth and direction within a layer.

Fig. 6 shows the variation of the microstructure depth *h* (generated by the DLIP pixel) as a function of the number of pulses per unit area for a fluence of 2.86 J/cm^2. As it can be seen, the trend is almost linear and large-scale micropillars with depths *h* over 30 μm could be generated for the periods of 4.3 μm and 8.5 μm, while for the spatial period of 2 μm it is sensibly lower. This effect can be ascribed to the increased projection of the interference volume for a period of 2 μm: in fact the interference angle generating a period of 2 μm is 14.6°, which is sensibly higher than the ones for 4.3 μm and 8.5 μm (7° and 3.6°, respectively). Therefore, the projection of the DLIP pixel increases and the Gaussian intensity is projected over a larger area, thus decreasing the local fluence.

It is important to mention that the depths *d* of the small-scale interference-generated micropillars are the same as it is in the low power case (shown in Fig. 4). Due to the high power employed, the protruding fibres are chopped into fragments by the central part of the interference area, which can be removed using compressed air. However, higher applied laser fluences result in cracking and damage of the small-scale micropillars, especially when higher number of pulses are applied, as can be observed comparing Fig. 5c and f.

3.2. UV-DLIP processing

Contrary to the IR-DLIP processing, no cracking or damaging thermal effects were observed during UV-DLIP processing in the available laser power range, hence the maximum achievable laser fluence of 2.0 J/cm^2 was used. Due to the high absorption of the polymer at the used wavelength, a lower number of pulses per unit area were required for structuring. Note that an additional pre-treatment like in the IR-DLIP case aimed to remove the first polymer layer was in this case not needed.

Due to a higher absorption of the UV radiation in PEEK, ablation of the polymer matrix and fibres was observed, as shown in Fig. 7a–c.
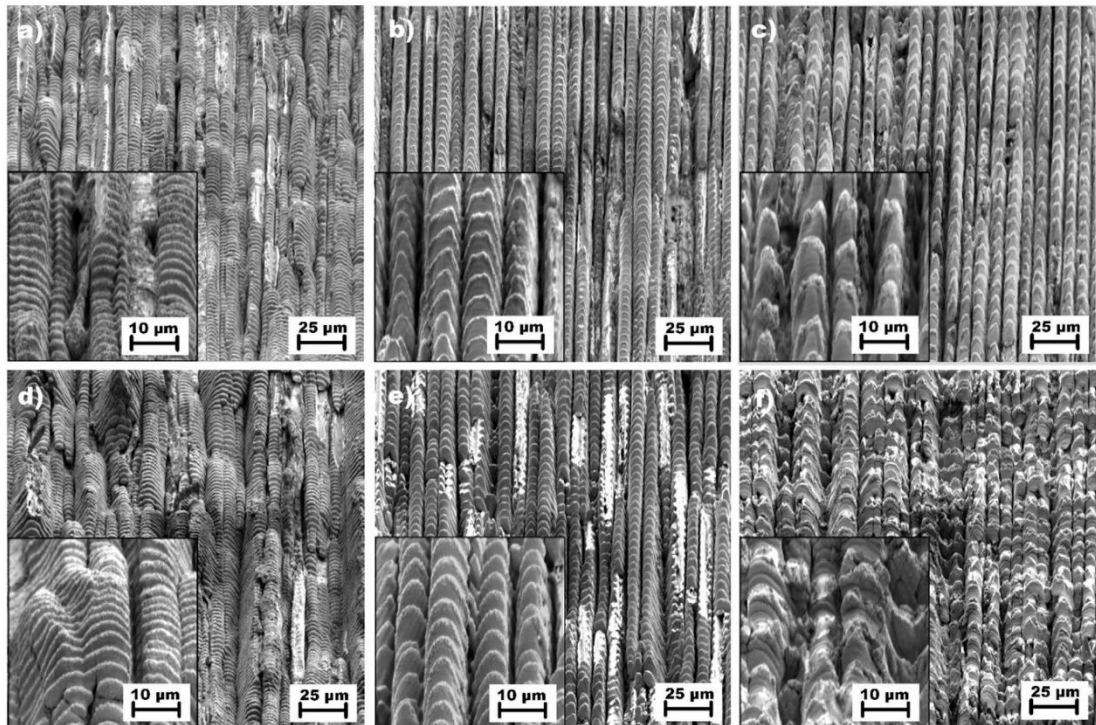
Fig. 3. SEM analysis of surface structures fabricated with IR radiation with increasing number of pulses per unit area N, spatial period Λ and laser fluence of 1.4 J/cm^2 and corresponding inserts with higher magnification. To observe surface geometry, sample was tilted for 55°. (a) Λ = 2 μm, N = 200, (b) Λ = 4.3 μm, N = 200, (c) Λ = 8.5 μm, N = 200, (d) Λ = 2 μm, N = 1200, (e) Λ = 4.3 μm, N = 1200, (f) Λ = 8.5 μm, N = 1200.
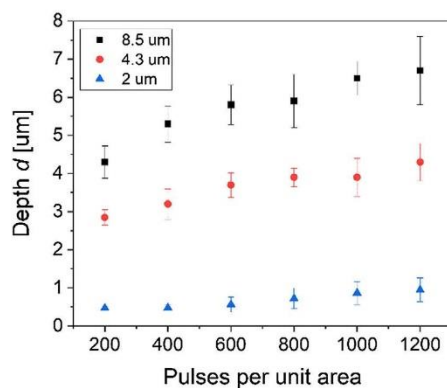
Fig. 4. Small-scale micropillar depth evolution (2-beam DLIP treatments with IR radiation) with increasing number of pulses per unit area for different spatial periods Λ and a laser fluence of 1.4 J/cm^2.

With an increasing number of pulses per unit area, the polymer matrix is vaporized due to the heat input from fibres in a similar way as described for the IR treatment. Nevertheless, the microstructures show no visible cracking, as shown in Fig. 7d–f.

The formation of hierarchical structures was observed only for the spatial period of 1.5 μm and a pulse overlap exceeding 99%. An example of these structures is shown in Fig. 8, where the higher period is generated by hatch distance (17 μm) and the smaller one by the interference pattern, independently on the orientation of the fibres with

respect to the interference lines.

The evolution of the structure depth d and depth h (in the case of 1.5 μm spatial period) is shown in Fig. 9. As it can be noticed, the dependencies are exhibit a linear trend. Higher depth d is reached for larger spatial periods with the maximum of 6.14 μm for a spatial period of 8.5 μm. The exception is 1.5 μm period where hierarchical structures are formed with the depth h of large-scale pillars (Fig. 8 b) reaching 11 μm, with the depth d of small-scale interference-made pillars comparable with 2 μm interference period, as shown in a graph in Fig. 9. This effect, opposite to the one noted for Fig. 6, can be instead ascribed to the increased unselective material removal rate for small period and UV radiation, as described by Alamri et al. [32].

3.3. Wettability change

Static contact angle (WCA) measurements were performed to evaluate the wettability performance of the structured surfaces. The unpatterned surface (reference) is slightly hydrophilic with a WCA value of 77°. The WCA measurements performed after DLIP treatment were found to show both, Cassie-Baxter- [39] and Wenzel-like [40] states with WCA values of 30° and 140° for repeated measurements at same spot as well as for surfaces processed with same laser parameters. This implicates strong pinning down effects of droplets to patterned region due to presence of high surface energy materials on the surface. This behaviour is demonstrated in Fig. 10 (red dots), for the surface processed with a spatial period of 4.3 μm.

To decrease surface energy, CVD treatments using 1H,1H,2H,2H-Perflorodecyl-triethoxysilane was applied, forming a nanometer-thick coating on the surface [41], which does not affect surface topography. After the CVD treatment, contact angles between 140 and 170° are
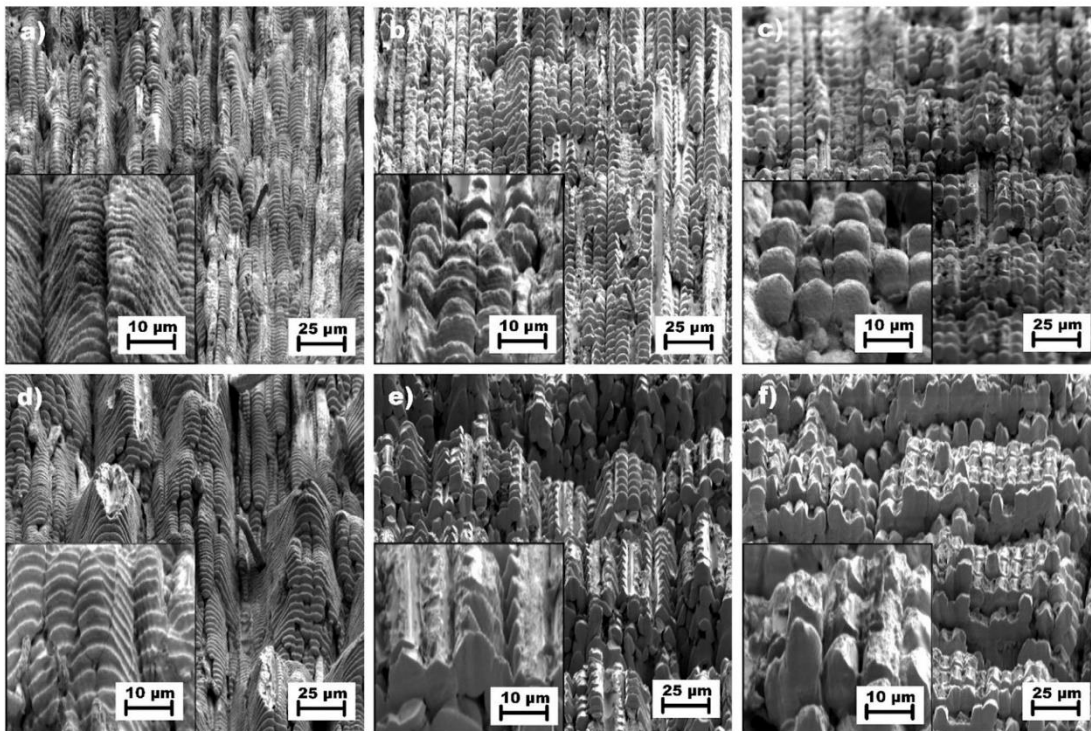
Fig. 5. SEM analysis of surface structures fabricated with IR radiation with increasing number of pulses per unit area N, spatial period Λ and laser fluence of 2.86 J/cm² with inserts of higher magnification images. To observe surface geometry, sample was tilted for 55°. (a) Λ = 2 μm, N = 200, (b) Λ = 4.3 μm, N = 200, (c) Λ = 8.5 μm, N = 200, (d) Λ = 2 μm, N = 1200, (e) Λ = 4.3 μm, N = 1200, (f) Λ = 8.5 μm, N = 1200.
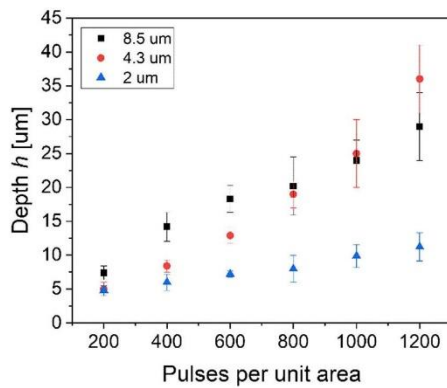

Fig. 6. Large-scale micropillars depth evolution of large-scale pillars with increasing number of pulses per unit area for different spatial periods Λ and laser fluence of 2.86 J/cm².

achieved in dependence on the structure depth d. Note that the contact angles stabilize at 160° for structure depths of 3.0 μm and above. This highlights that a transition from a partially wetted to the Cassie-Baxter state took place. The low surface energy introduced by the coating in conjunction with the well-defined surface roughness introduced by DLIP assures stable air pockets between the structure peaks. Consequently, water is not able to penetrate the cavities, regardless of the actual structure depth, as observed for surfaces with comparable dimensions in a superhydrophobic state [42]. The static WCA increased

from 77° to 110° for the un-patterned surface and the majority of laser-patterned surface exhibited severe water repellence with the maximum value of contact angle reaching 171°, as depicted in Fig. 11.

In general, it is observed that smaller spatial periods result in higher WCA values after CVD treatment which indicates a Wenzel-to-Cassie-Baxter transition. However, the evolution of the WCA with structure depths (d and h) for the same period is changing for different processing parameters. The depth and uniformity of the structures plays a significant role in the WCA evolution. For example, the samples irradiated with 2.86 J/cm² using IR-DLIP lead to hierarchical structures with high overall structure depth h and several cracks and imperfections which finally result in a reduced WCA. These imperfections are more pronounced with high number of pulses per unit area (see Fig. 6), allowing water to penetrate between these imperfections and resulting in a decrease of the WCA. When the laser fluence is decreased to 1.4 J/cm², the surface uniformity is improved (see Fig. 4) which leads to an increased WCA with the depth d up to a threshold of pulses per unit area (400 pulses for 4.3 μm period and 600 pulses for 8 μm period) when structure imperfections start to play a major role.

The wettability analysis of the UV-DLIP treated surfaces highlights that the WCA performance correlates well with the achieved structure depth. Moreover, the best quality structures were fabricated with the UV-DLIP processing. The highest CA of 171°, with a sliding angle of only 2°, was achieved for the deepest structures fabricated with the 1.5 μm interference period (see Fig. 11).

3.4. Summary and discussion

The DLIP processing of C-PEEK was possible with both, IR and UV laser sources. It was found that the line-like interference pattern has to
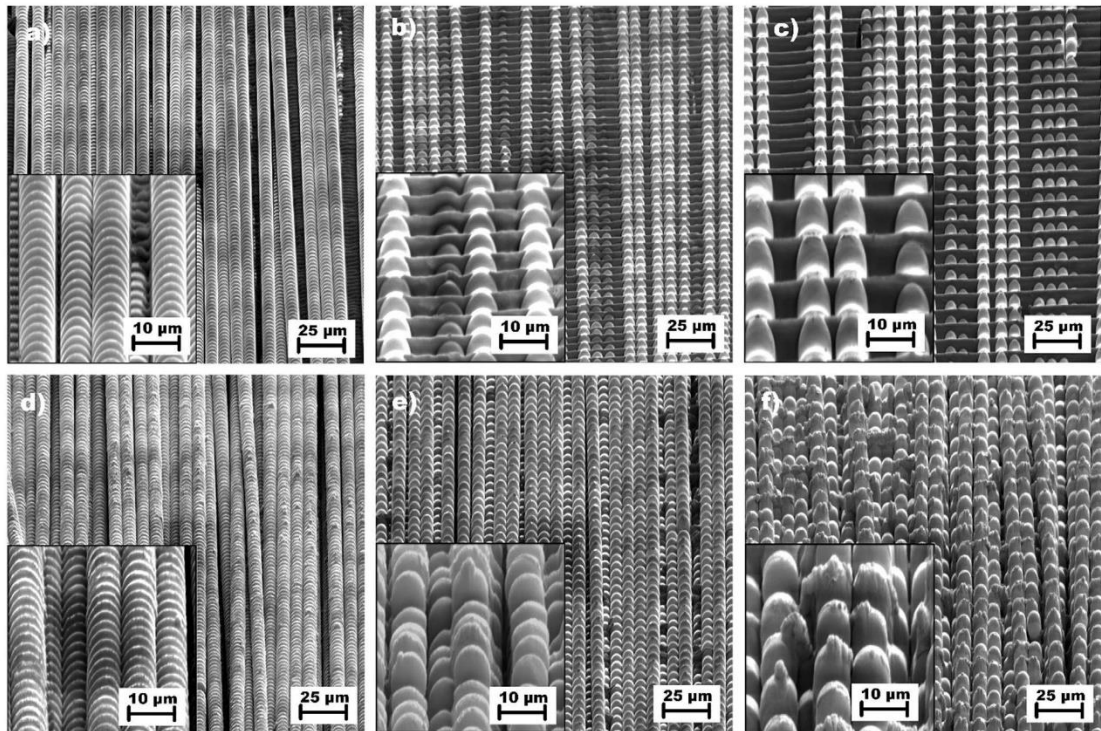
Fig. 7. SEM analysis of surface structures fabricated with UV radiation with increasing number of pulses per unit area N, spatial period Λ and laser fluence of 2 J/cm^2 with inserts of higher magnification images. To observe surface geometry, sample was tilted for 55° for SEM analysis. (a) Λ = 2 μm, N = 10, (b) Λ = 4.3 μm, N = 10, (c) Λ = 8.5 μm, N = 10, (d) Λ = 2 μm, N = 200, (e) Λ = 4.3 μm, N = 200, (f) Λ = 8.5 μm, N = 200.

be oriented perpendicularly to the fibre direction in order to fabricate pillar-like multi-scale microstructures on the processed surfaces, in a single step process.

The results revealed that the fibres are not necessarily evenly distributed within the polymer matrix. The fibre direction and depth are not homogenous in a layer, as can be clearly observed from Fig. 7. As a result, structure dimensions are different in a direction of fiber axis and in the perpendicular direction. For a low number of laser pulses, only

the top surface fibres are uncovered and it was found that the polymer matrix can be vaporized with increasing laser fluence (heat input) on the incorporated fibres (namely in the case of IR-DLIP treatments).

Two irradiation conditions were observed during structuring affecting the shape and depth of produced structures. The interference pattern was homogeneously distributed over the sample when low power (e.g. 1.4 J/cm^2, IR DLIP) and period > 2 μm were applied. However, for higher power levels in case of IR DLIP or very small
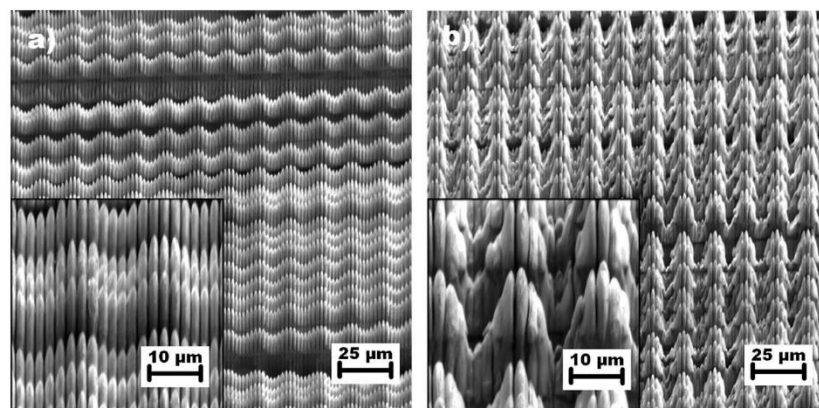

Fig. 8. Hierarchical structures fabricated with UV irradiation with 2 J/cm^2, 1.5 μm spatial period, (a) 70 and (b) 200 pulses per unit area. Small inserts show the structure under higher magnification. To observe surface geometry, sample was tiled for 55° for SEM analysis.
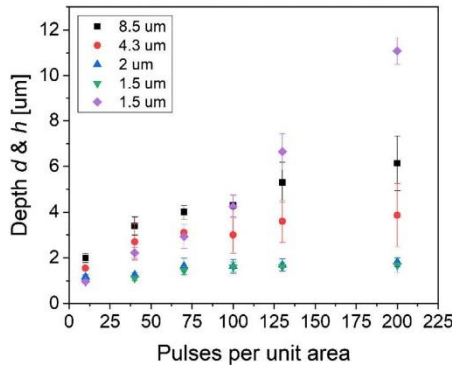
6

Fig. 9. Structure depth (*d* and *h*) evolution with increasing number of pulses per unit area for different spatial periods Λ and laser fluence of 2 J/cm². Hierarchical structures were fabricated with 1.5 μm period: small-scale micropillars are marked with the green triangle and large-scale micropillars formed due to Gaussian modulation of the intensity are marked with the violet rectangle.
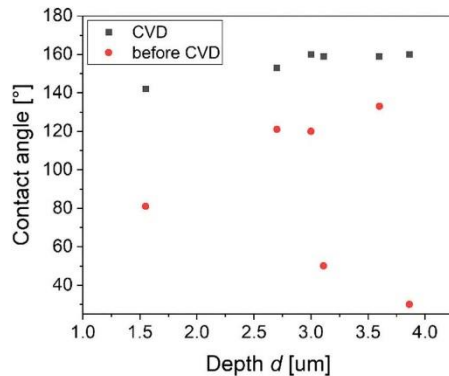

Fig. 10. Single measurements (not averaged) of static contact angle of laser processed sample with 4.3 μm period, using 2 J/cm² and UV laser source, before (red) and after (black) CVD treatment, demonstrating the inconsistency of results for the surface before CVD treatment caused by switching between Wenzel and Cassie-Baxter state.

periods (1.5 μm) in case of UV DLIP, the gaussian modulation inside DLIP pixel can be observed (Fig. 8b). In this case, interference lines in the middle of DLIP pixel have higher intensity which is exponentially decreasing towards the edges of the pixel. As a result, a much deeper hierarchical structures with large-scale micropillars (result of the gaussian modulation) covered with small-scale micropillars (result of two-beam interference pattern) were produced, both fabricated in the single step.

Different quality and geometry were achieved under IR and UV irradiation. The main reason for that is different ablation mechanism and absorption of PEEK matrix in IR and UV wavelength. As shown in Ref. [38], at 266 nm absorption is close to 100% due to the p-p* transition of the aromatic ring which is photochemically inactive, thus results in a photothermal process at this wavelength [35,43]. On the other hand, absorption at 1053 nm is only ~65% [38]. Low absorption in polymer matrix together with higher absorption and melting point of carbon fibres [44] leads to melting and vaporization of polymer due to heat transferred from carbon fibers. In this case pure heating results in mechanical breakdown of polymer [45], which may lead to crack formation between different fibre layers, especially when higher fluence

and number of pulses are applied. The broken fibres loosely attached to the crater could be removed by an ultrasonic cleaning. The UV laser source is therefore much more suitable for structures with high quality and uniformity.

The fabrication speed to produce structures with a spatial period of 2 μm (as shown in Fig. 8a) reaches 39 min/cm², which is comparable to state of the art direct laser writing [46] (e.g. 55 min/cm² to obtain CA over 140° on stainless steel [20]). Moreover, considering the used laser power in this work (10 mW, 1 kHz for UV laser), the fabrication speed can be easily scaled by several orders of magnitude, especially in connection with scanner-based DLIP approaches [47].

Plethora surface geometry can be achieved by changing the spatial period. The most uniform micropillars were fabricated with special period of 4.3 μm, since it is very close to fiber diameter (5 μm). The anisotropy in a shape of micropillar is most visible for small periods bellow 2 μm (Fig. 7a, d). In this case, different contact angles in parallel and perpendicular direction to the fibre axis were expected. However, measured WCA are comparable with a deviation of ± 4° for both directions. The wettability is therefore found to be in a Cassie-Baxter state, with lower fractional area of contact between liquid and solid occurred due to air pockets formed between pillars. Consequently, with the same depth and quality of produced structures, spatial period can be used for controlling the wettability, as demonstrated in Fig. 11c. Smaller the period, higher the density of produced microstructures and higher the WCA. Therefore, according to Cassie-Baxter theory, the contact area between water and solid surface is also decreasing with spatial period.

Except spatial period, the wettability performance of the fabricated microstructures is after CVD treatment mainly dependent on their depth and uniformity. Generally, higher structure depth (*d* or *h*) leads to higher WCA and it can be well-controlled by increasing the number of laser pulses per DLIP pixel. However, the surface quality and uniformity of the fabricated structures is decreasing with a higher number of laser pulses. Therefore, there is a balance between micropillar depth and quality in the view of WCA that can be clearly observed for samples processed with 1.4 J/cm² in IR and a spatial period of 4.3 μm (Fig. 11a). In this case, the WCA increases with the achieved structure depth *d* by applying up to 400 pulses per unit area, and then starts decreasing due to high thermal input resulting in a formation of cracks and imperfections on a surface. The quality suffers the most when the surface is irradiated with IR laser source and a laser fluence of 2.86 J/cm². In this case, the WCA is decreasing with the number of pulses per unit area, even though the depth *h* is significantly increased. Consequently, the reduction of the WCA is particularly observed for IR-DLIP processing, contrary to a significantly reduced amount of cracks and imperfections in the case of UV-DLIP treatment.

4. Conclusion

Fabrication of well-defined and melt-free periodic structures on carbon fiber reinforced PEEK composite material using nanosecond DLIP has been demonstrated. By increasing the number of pulses per unit area or laser power, depth and homogeneity of the fabricated structures could be controlled. Quality and homogeneity of fabricated structures, as well as their depth, were found to be dependent also on the laser wavelength. However, several cracks and imperfections are found on a surface after high-overlap IR treatments. DLIP with UV laser source demonstrated fabrication of microstructures with high quality without cracks and inhomogeneities. Apart from the chemical modifications of the surface, depth of structures and surface uniformity plays a major role for wettability behaviour of IR-DLIP treated samples: the static WCA is increasing with the structure depth until the threshold of pulses per unit area when surface inhomogeneities starts to play a major role. This behaviour is even more pronounced for DLIP treatments at laser fluences of 2.86 J/cm². Nevertheless, a significant increase of the WCA exceeding 150° has been demonstrated for all spatial
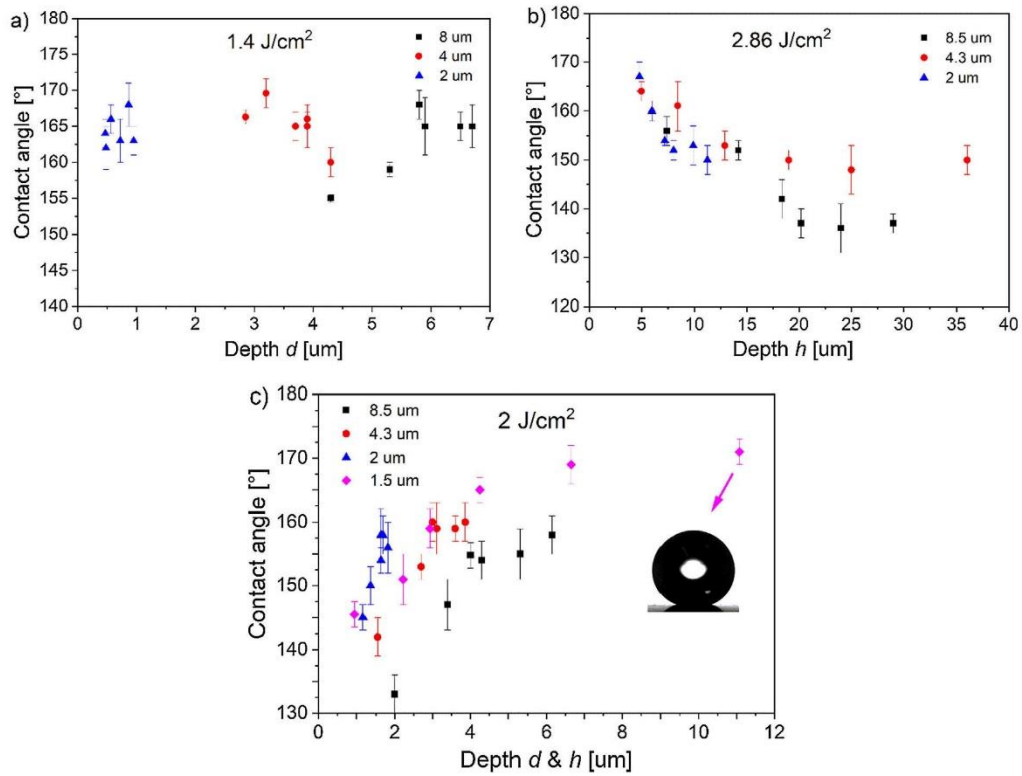
Fig. 11. Static contact angles for a different spatial periods of laser processed samples after CVD treatment, measured with 8 μl droplet size using (a) 1.4 J/cm^2 and IR laser source in a dependence on the small-scale micropillar depth d, (b) 2.86 J/cm^2 and IR laser source in a dependence on the large-scale micropillar depth h, (c) 2 J/cm^2 and UV laser source in a dependence on depth d and depth h (in the case of 1.5 μm period).

periods of 8.5, 4.3, 2, 1.5 μm and both laser sources after CVD surface energy passivation. However, the best results were reached for crack free surface, fabricated by UV-DLIP. The highest static contact angle of 171° was obtained for the deepest hierarchical structures produced with 1.5 μm spatial period under UV irradiation. Besides providing better quality of the treated surfaces, it may be also concluded that, UV processing is faster and more efficient since it requires much lower average power and number of pulses per unit area for production of microstructures with a high CA.

CRediT authorship contribution statement

P. Hauschwitz: Conceptualization, Methodology, Validation, Investigation, Writing - original draft, Writing - review & editing. **R. Jagdheesh:** Validation, Writing - review & editing. **S. Alamri:** Conceptualization, Methodology, Validation, Writing - review & editing. **D. Rostohar:** Conceptualization, Writing - review & editing. **T. Kunze:** Conceptualization, Methodology, Validation, Resources, Writing - review & editing. **J. Brajer:** Writing - review & editing. **J. Kopecek:** Resources. **T. Mocek:** Funding acquisition.

Declaration of Competing Interest

The authors declare that they have no known competing financial interests or personal relationships that could have appeared to influence the work reported in this paper.

References

[1] S. Das, J. Warren, D. West, S.M. Schexnayder, Global carbon fiber composites supply chain competitiveness analysis, Clean Energy Manufacturing Analysis Center, Golden, CO, Technical Report No. ORNL/SR-2016/100—NREL/TP-6A50-66071, 2016.

[2] P.K. Mallick, Fiber-Reinforced Composites: Materials, Manufacturing, and Design, CRC Press, 2007.

[3] M. El-Hofy, H. El-Hofy, Laser beam machining of carbon fiber reinforced composites: a review, Int. J. Adv. Manuf. Tech. 101 (2019) 2965–2975.

[4] M.B. Bragg, A.P. Broeren, L.A. Blumenthal, Iced-airfoil aerodynamics, Prog. Aerosp. Sci. 41 (2005) 323–362.

[5] S. Kulinich, M. Farzaneh, Ice adhesion on super-hydrophobic surfaces, Appl. Surf. Sci. 255 (2009) 8153–8157.

[6] D.A. del Cerro, G.R.B.E. Römer, A.J. Huis IN'T Veld, Picosecond laser machined designed patterns with anti-ice effect, in: Proceedings of the 11th International Symposium on Laser Precision Microfabrication, LPM2010, Stuttgart, Germany, June 7-10, 2010, 2010.

[7] F. Wang, C. Li, Y. Lv, F. Lv, Y. Du, Ice accretion on superhydrophobic aluminum surfaces under low-temperature conditions, Cold Reg. Sci. Technol. 62 (2010) 29–33.

[8] T.M. Schutzius, S. Jung, T. Maitra, P. Eberle, C. Antonini, C. Stamatopoulos, D. Poulikakos, Physics of icing and rational design of surfaces with extraordinary

icephobicity, Langmuir 31 (2014) 4807–4821.

[9] L. Mishchenko, B. Hatton, V. Bahadur, J.A. Taylor, T. Krupenkin, J. Aizenberg, Design of ice-free nanostructured surfaces based on repulsion of impacting water droplets, ACS Nano 4 (2010) 7699–7707.

[10] Y. Liu, G. Li, A new method for producing "Lotus Effect" on a biomimetic shark skin, J. Colloid Interface Sci. 388 (2012) 235–242.

[11] J.-Y. Shiu, C.-W. Kuo, P. Chen, C.-Y. Mou, Fabrication of tunable superhydrophobic surfaces by nanosphere lithography, Chem. Mater. 16 (2004) 561–564.

[12] Y. Liu, S. Li, Y. Wang, H. Wang, K. Gao, Z. Han, L. Ren, Superhydrophobic and superoleophobic surface by electrodeposition on magnesium alloy substrate: wettability and corrosion inhibition, J. Colloid Interface Sci. 478 (2016) 164–171.

[13] R. Lakshmi, B.J. Basu, Fabrication of superhydrophobic sol–gel composite films using hydrophobically modified colloidal zinc hydroxide, J. Colloid Interface Sci. 339 (2009) 454–460.

[14] D.E. Weibel, A.F. Michels, A.F. Feil, L.V. Amaral, S.R. Teixeira, F. Horowitz, Adjustable hydrophobicity of Al substrates by chemical surface functionalization of nano/microstructures, J. Phys. Chem. C 114 (2010) 13219–13225.

[15] S.F. Toosi, S. Moradi, M. Ebrahimi, S.G. Hatzikiriakos, Microfabrication of polymeric surfaces with extreme wettability using hot embossing, Appl. Surf. Sci. 378 (2016) 426–434.

[16] R. Jagdheesh, M. Diaz, S. Marimuthu, J. Ocana, Robust fabrication of μ-patterns with tunable and durable wetting properties: hydrophilic to ultrahydrophobic via a vacuum process, J. Mater. Chem. A 5 (2017) 7125–7136.

[17] J. Long, M. Zhong, H. Zhang, P. Fan, Superhydrophilicity to superhydrophobicity transition of picosecond laser microstructured aluminum in ambient air, J. Colloid Interface Sci. 441 (2015) 1–9.

[18] M.V. Rukosuyev, J. Lee, S.J. Cho, G. Lim, M.B. Jun, One-step fabrication of superhydrophobic hierarchical structures by femtosecond laser ablation, Appl. Surf. Sci. 313 (2014) 411–417.

[19] J. Song, D. Wang, L. Hu, X. Huang, Y. Chen, Superhydrophobic surface fabricated by nanosecond laser and perhydropolysilazane, Appl. Surf. Sci. (2018).

[20] B. Wu, M. Zhou, J. Li, X. Ye, G. Li, L. Cai, Superhydrophobic surfaces fabricated by microstructuring of stainless steel using a femtosecond laser, Appl. Surf. Sci. 256 (2009) 61–66.

[21] P. Hauschwitz, R. Jagdheesh, D. Rostohar, J. Brajer, J. Kopeček, P. Jiříček, J. Houdková, T. Mocek, Nanostructure fabrication on the top of laser-made micropillars for enhancement of water repellence of aluminium alloy, Mater. Lett. 126601 (2019).

[22] R. Jagdheesh, P. Hauschwitz, J. Mužík, J. Brajer, D. Rostohar, P. Jiříček, J. Houdkova, J. Kopeček, T. Mocek, Non-fluorinated superhydrophobic Al7075 aerospace alloy by ps laser processing, Appl. Surf. Sci. (2019).

[23] J. Long, P. Fan, D. Gong, D. Jiang, H. Zhang, L. Li, M. Zhong, Superhydrophobic surfaces fabricated by femtosecond laser with tunable water adhesion: from lotus leaf to rose petal, ACS Appl. Mater. Interfaces 7 (2015) 9858–9865.

[24] R. De Loor, Polygon scanner system for ultra short pulsed laser micro-machining applications, Phys. Proc. 41 (2013) 544–551.

[25] Z. Kuang, D. Liu, W. Perrie, S. Edwardson, M. Sharp, E. Fearon, G. Dearden, K. Watkins, Fast parallel diffractive multi-beam femtosecond laser surface microstructuring, Appl. Surf. Sci. 255 (2009) 6582–6588.

[26] E. Gu, C. Jeon, H. Choi, G. Rice, M. Dawson, E. Illy, M. Knowles, Micromachining and dicing of sapphire, gallium nitride and micro LED devices with UV copper vapour laser, Thin Solid Films 453 (2004) 462–466.

[27] T. Otani, L. Herbst, M. Heglin, S. Govorkov, A. Wiessner, Microdrilling and micromachining with diode-pumped solid-state lasers, Appl. Phys. A 79 (2004) 1335–1339.

[28] X. Liu, D. Du, G. Mourou, Laser ablation and micromachining with ultrashort laser pulses, IEEE J. Quantum Electron. 33 (1997) 1706–1716.

[29] M.M. Burns, J.-M. Fournier, J.A. Golovchenko, Optical matter: crystallization and binding in intense optical fields, Science 249 (1990) 749–754.

[30] A. Lasagni, T. Roch, J. Berger, T. Kunze, V. Lang, E. Beyer, To use or not to use (direct laser interference patterning), that is the question, in: Laser-based Micro-and Nanoprocessing IX, International Society for Optics and Photonics, 2015, pp. 935115.

[31] B. Voisiat, M. Gedvilas, S. Indrišiūnas, G. Račiukaitis, Picosecond-laser 4-beam-interference ablation as a flexible tool for thin film microstructuring, Phys. Proc. 12 (2011) 116–124.

[32] S. Alamri, A.F. Lasagni, Development of a general model for direct laser interference patterning of polymers, Opt. Expr. 25 (2017) 9603–9616.

[33] J. Valle, S. Burgui, D. Langheinrich, C. Gil, C. Solano, A. Toledo-Arana, R. Helbig, A. Lasagni, I. Lasa, Evaluation of surface microtopography engineered by direct laser interference for bacterial anti-biofouling, Macromol. Biosci. 15 (2015) 1060–1069.

[34] S. Alamri, A.I. Aguilar-Morales, A.F. Lasagni, Controlling the wettability of polycarbonate substrates by producing hierarchical structures using direct laser interference patterning, Eur. Polym. J. 99 (2018) 27–37.

[35] A.F. Lasagni, D.F. Acevedo, C.A. Barbero, F. Mücklich, One-step production of organized surface architectures on polymeric materials by direct laser interference patterning, Adv. Eng. Mater. 9 (2007) 99–103.

[36] F. Roessler, A.F. Lasagni, Protecting sub-micrometer surface features in polymers from mechanical damage using hierarchical patterns, J. Laser Micro Nanoen. 13 (2018) 68–75.

[37] P. Mangalgiri, Composite materials for aerospace applications, Bull. Mater. Sci. 22 (1999) 657–664.

[38] L. Romoli, F. Fischer, R. Kling, A study on UV laser drilling of PEEK reinforced with carbon fibers, Opt. Lasers Eng. 50 (2012) 449–457.

[39] A. Cassie, S. Baxter, Wettability of porous surfaces, Trans. Faraday Soc. 40 (1944) 546–551.

[40] R.N. Wenzel, Resistance of solid surfaces to wetting by water, Ind. Eng. Chem. Prod. Res. Dev. 28 (1936) 988–994.

[41] A. Hozumi, K. Ushiyama, H. Sugimura, O. Takai, Fluoroalkylsilane monolayers formed by chemical vapor surface modification on hydroxylated oxide surfaces, Langmuir 15 (1999) 7600–7604.

[42] C. Lv, X. Zhang, F. Niu, F. He, P. Hao, From initial nucleation to cassie-baxter state of condensed droplets on nanotextured superhydrophobic surfaces, Sci. Reports 7 (2017) 42752.

[43] R.M. Silverstein, G.C. Bassler, Spectrometric identification of organic compounds, J. Chem. Educat. 39 (1962) 546.

[44] J. Hu, H. Xu, C. Li, Laser absorption of carbon fiber reinforced polymer with randomly distributed carbon fibers, Laser Phys. 28 (2018) 036002.

[45] T. Lippert, UV laser ablation of polymers: from structuring to thin film deposition, in: Laser-Surface Interactions for New Materials Production, Springer, 2010, pp. 141–175.

[46] A.I. Aguilar-Morales, S. Alamri, A.F. Lasagni, Micro-fabrication of high aspect ratio periodic structures on stainless steel by picosecond direct laser interference patterning, J. Mater. Process. Technol. 252 (2018) 313–321.

[47] T. Kunze, C. Zwahr, B. Krupop, S. Alamri, F. Rößler, A.F. Lasagni, Development of a scanner-based direct laser interference patterning optical head: new surface structuring opportunities, in: Laser-based Micro-and Nanoprocessing XI, International Society for Optics and Photonics, 2017, pp. 1009214.

9

5.4 Journal article D. Towards Rapid Large-Scale LIPSS Fabrication by 4-beam ps DLIP

In this journal paper a newly developed interference setup, designed and built by the author, has been used to produce LIPSS-structured microcraters inside each of 4-beam interference maxima. A unique combination of ultrashort high-energy pulsed HiLASE laser source with a novel large-beam DLIP technique resulted in the fabrication of ~1016 LIPSS-structured microcraters in 5 ms (203 200 spot/s). The functional properties of the structured surface were demonstrated showing superhydrophobic behaviour and a change in structural colour, thus showing great potential for rapid large-scale production of LIPSS-based functional surfaces.

Author contribution

In work related to the production of this journal paper, P. Hauschwitz designed and build interference processing station, planned, designed and carried out all experiments with the help of D. Jochcová. P. Hauschwitz also analysed SEM data with J. Kopeček and interpreted results. P. Hauschwitz was responsible for drafting the manuscript and communication with the journal. Detail authors individual contributions are listed in table 4.

Term	Authors' individual contributions
Conceptualization	P. Hauschwitz, D. Jochcová
Methodology	P. Hauschwitz
Software	D. Jochcová
Validation	P. Hauschwitz
Formal analysis	P. Hauschwitz
Investigation	P. Hauschwitz, D. Jochcová
Resources	T. Mocek, J. Brajer, J. Kopeček, M. Cimrman
Writing - Original Draft	P. Hauschwitz
Writing - Review & Editing	P. Hauschwitz, D. Rostohar, J. Radhakrishnan, D. Jochcova
Visualization	P. Hauschwitz
Supervision	J. Radhakrishnan, D. Rostohar, J. Brajer, T. Mocek
Project administration	P. Hauschwitz, J. Brajer
Funding acquisition	T. Mocek, M. Smrž, A. Luccianetti

Table 4: Credit author statement - Towards Rapid Large-Scale LIPSS Fabrication by 4-beam ps DLIP
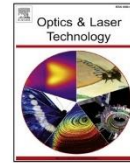
Full length article

Towards rapid large-scale LIPSS fabrication by 4-beam ps DLIP

P. Hauschwitz[a,c,*], D. Jochcová[a,c], R. Jagdheesh[a], D. Rostohar[a], J. Brajer[a], J. Kopeček[b],
M. Cimrman[a,c], M. Smrž[a], T. Mocek[a], Antonio Lucianetti[a]

[a] Hilase Centre, Institute of Physics, Academy of Sciences of the Czech Republic, Za Radnici 828, Dolni Brezany 25241, Czech Republic
[b] Institute of Physics of the Czech Academy of Sciences, Na Slovance 2, Prague, Czech Republic
[c] Faculty of Nuclear Sciences and Physical Engineering, Czech Technical University in Prague, Brehova 7, 115 19 Prague, Czech Republic

HIGHLIGHTS

- Interference area is increased up to 1 mm in diameter to reach higher throughputs.
- Parameters for fabrication of LIPSS-structured microcraters are investigated.
- Throughputs up to 30 400 LSFL spots/s and 203 200 HSFL spots/s are achieved.
- Superhydrophobicity and structural colours are demonstrated on selected surfaces.

ARTICLE INFO

ABSTRACT

Using four beam direct laser interference patterning (DLIP) Laser Induced Periodic Surface Structures (LIPSS, ripples) are simultaneously generated on surface of AISI 316L steel in more than thousands of spots at once. Both low-spatial frequency LIPSS (LSFL) and high-spatial frequency LIPSS (HFSL) are possible to fabricate with optimized parameters of 1030 nm, 1.7 ps PERLA laser system, developed and operated at HiLASE center. A novel large-beam DLIP technique applied for the redistribution of initial laser energy per pulse results in fabrication of ~1520 spots with LSFL in 50 ms and ~1016 spots with HSFL in 5 ms, thus significantly improving the productivity in comparison with the single beam approach. Efficient production of LIPSS structures over large area, required for applications such as a production of security diffractive elements and surfaces with superhydrophobic properties is also demonstrated. Possible steps for further increase of processing speed are discussed.

1. Introduction

Direct laser ablation processing using ultrashort pulsed laser systems is an attractive method to produce Laser-Induced Periodic Surface Structures (LIPSS) due to its simplicity, flexibility and variability of produced structures [1]. LIPSS can be generated in single step process, allowing surface nanostructuring for tailoring tribological, optical, mechanical and chemical surface properties. They can be classified by their period to low-spatial frequency LIPSS (LSFL) when periodicity of structures is close to laser wavelength and high-spatial frequency LIPSS (HSFL) characterized by period much smaller than laser wavelength. Such structures can impose new properties to metals, dielectrics, polymers or composite materials [2] including fabrication of diffractive structures for goods protection [1], superhydrophobicity and self-cleaning [3], control of friction [4], anti-reflection [5], anti-bacteria [6]

or decoration [7] leading to increasing attractivity of LIPSS in scientific community and industry in the past decade.

However, the processing speed is a limiting factor for industrial use of LIPSS. Common single beam approaches allow fabrication speeds only up to tens of cm² per minute [1]. Moreover, with emerging high power ultrashort laser systems [8] the LIPSS production becomes very inefficient since LIPSS production requires processing close to ablation threshold [9] thus using only a small percentage of available power. Therefore, new fabrication approaches are necessary to efficiently use high power laser sources to scale up the fabrication speed. These may include ultrafast beam scanning [10] or multi-beam and interference approaches [11].

Direct laser interference patterning (DLIP) became fast and efficient way for laser micro-processing in recent years [12,13]. It is a technique when two or more coherent laser beams overlap on a material surface in

order to directly impose periodic interference pattern. The geometry of the interference pattern can be controlled by the number of laser beams and their incidence angle as well as by wavelength, polarization, intensity and phase difference of these beams [14].

In this work, a novel technique for increasing the interference area to efficiently use high-energy pulse laser system is introduced. Moreover, a combination of DLIP and LIPSS is used to increase the throughputs of micron and sub-micron sized periodical structures at the same time. Selection of proper processing parameters enables the formation of LIPSS structures inside each of the four beam interference maxima and consequently allows upscaling of the fabrication speed of LIPSS based diffractive and superhydrophobic surfaces in orders of magnitude.

2. Materials and methods

Common use of AISI 316L steel in industrial contexts includes production of medical implants, precision mechanics, marine applications or food handling and surface functionalization can bring many potential benefits to those products. Flat samples were treated in air with 1030 nm HiLASE Perla B laser system operated at 1 kHz repetition rate. Pulse duration of 1.7 ps and pulse energy up to 3 mJ were used during the experiment. The initial laser beam was split to four sub-beams, which were collimated by a prism and finally overlapped by a lens with 300 mm focal length creating dot-like interference pattern on the sample surface, as depicted in Fig. 1a-c. Prism position was set to create an interference pattern with the periodicity of 25 μm. Linear stages were used to displace the pattern over larger area of the sample. Prior to wettability measurements, processed samples were placed into high vacuum conditions (10^{-7} Pa) to significantly decrease transition time to superhydrophobic state [15].

2.1. Multiple-beam interference

In order to evaluate shape, dimensions and periodicity of an interference pattern as well as to explore potential of the proposed DLIP multi-beam approach for efficient surface structuring, the fundamental principles of the interference patterning are explained.

General formula for the intensity of n beams is expressed by equation [13]:

$$I(\vec{r}) \approx \sum_{i=1}^{n} |\vec{E}_{0i}|^2 + 2\sum_{j<i}^{n}\sum_{i=1}^{n} \vec{E}_{0i}. \vec{E}_{0j}\cos(\vec{k}_i. \vec{r} - \vec{k}_j. \vec{r} + \varphi_i - \varphi_j) \quad (1)$$

According to Eq. (1), it is possible to conclude that the shape and dimensions of an interference pattern depends on number of beams, polarization of each beam, relative phase shift and mutual position of beams in space. Using the Eq. (1) for the case of four symmetrically arranged linear polarized beams with relative phase shift equal to zero, the intensity function can be evaluated as follows:

$$I(x, y) \approx 4 + 2\cos Ay + 2\frac{b^2 - a^2}{a^2 + b^2}\cos Ax + \frac{8b}{\sqrt{a^2+b^2}}\cos\frac{A}{2}y\cos\frac{A}{2}x, \quad (2)$$

where a, b are real constants whose values are determined by the angle of incidence θ between beams $\tan\frac{\theta}{2} = a/b$ and $A = \frac{4\pi}{\lambda}\frac{a}{\sqrt{a^2+b^2}}$, where λ is the wavelength. However, this relation can only be used if all four polarization vectors are coplanar. In the case of a small angle of incidence θ, $a \ll b$ and $\frac{b^2-a^2}{a^2+b^2} \approx 1$, the intensity is distributed equally among interference maxima in both x and y direction i.e. dotted pattern is symmetrical.

The periodicity of the interference pattern can be than calculated using Eq. (3):

$$P = \frac{\lambda}{\sqrt{2}\sin(\theta/2)} \quad (3)$$

Excellent agreement between the simulation of interference pattern calculated according to Eq. (2) (Fig. 1b) and the fabricated pattern on the sample surface (Fig. 1c) confirms that the interference theory can be successfully applied to calculate the geometry of pattern prior to laser irradiation.

To reach higher throughputs, the interference plane (the intersection of the interference volume and sample surface) should be as high as possible. The area of interference plane is dependent on the beam size on the sample, spatial coherence and pulse duration [16]. The area of interference plane can be increased by shifting the interference plane away from the focal plane, as illustrated in Fig. 1d. Thus, the area can be well above the diffraction limit. This can be done either by proper combination of DOE separation angle and prism compensation angle or
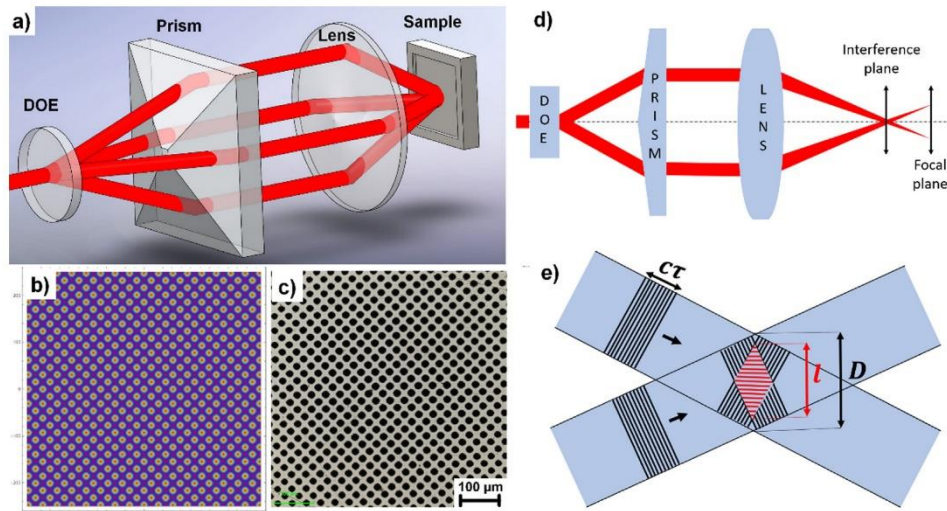

Fig. 1. (a) Four beam DLIP setup; (b) Comparison of calculated interference pattern according to Eq. (4) and the pattern fabricated on the sample surface (c); (d) Illustration of shifted focal and interference plane to reach larger interference area and higher throughputs; (e) Illustration of interference region with marked overlapped beam diameter D and diameter of interference area l.

by convergent or divergent input beam. It is worth to mention that the periodicity is not affected by increased beam size or beam divergence as long as the angle between overlapping beams remains the same. However, the pulse duration and spatial coherence may limit the maximal reachable interference area inside the overlapped beam region [17], as illustrated in Fig. 1d for simplified 2 beam example. Excellent beam quality of HiLASE Perla laser with $M^2 < 1.2$ indicates minimal aberration in the wavefront from an ideal gaussian beam with perfect spherical wavefront thus having a good spatial quality. In addition, double-slit experiment reveals a coherence area in order of a few millimeters. However, a direct wavefront fluctuations measurements are yet to be done in the near future. As illustrated in the Fig. 1d the diameter of interference area l is dependent on pulse duration. In optimal situation, the diameter of interference area should be the same or larger than overlapped beam diameter. For two beams overlapping at an angle θ, the size of interference area influenced by pulse duration can be estimated by formula (4) [17]:

$$l \approx \frac{ct}{\sin(\theta/2)} \tag{4}$$

where c is the speed of light and t is the pulse duration. Therefore, for the angle $\theta = 3.3°$, which gives periodicity of 25 μm, pulses can overlap on 20.6 mm distance.

In our experiments the setup was adjusted to reach approximately 1 mm in diameter (depending on applied pulse energy, number of pulses and material threshold), which is in the boundaries set by spatial coherence and pulse duration. It allows us to use reasonable pulse energies up to 3 mJ and process material much faster compared to common DLIP spot size, which is rarely above 200 μm in diameter [2,18,19].

2.2. Sample characterization

Samples were cleaned in ultrasonic bath with ethanol after the laser treatment. The surface morphology of treated samples was analyzed with a scanning electron microscope, Tescan FERA 3, at electron energy of 5 kV and scanning laser confocal microscope, Olympus OLS5000. Optical contact angle measuring device (OCA 15EC, Data Physics Instruments) was used to evaluate wettability of the treated surfaces by analyzing static contact angle under 8 μl deionized water droplets.

3. Results and discussion

Fig. 2a depicts the four beam interference pattern with a periodicity of 25 μm fabricated on AISI 316L stainless steel during exposition with 1000 pulses and pulse energy of 1 mJ. The size of interference area is dependent on the pulse energy and applied number of pulses as depicted in Fig. 2b.

The treated area increase is significant for the first 100 pulses and then saturates reaching up to 1.5 mm in diameter for 1000 pulses and 3 mJ, containing ~2800 individual spots fabricated in 100 ms (28,000 spots/s). The evolution of LIPSS formation with pulse energies of 1, 2 and 3 mJ (corresponding to a fluence of 0.10, 0.14, 0.17 J/cm^2, respectively) and a different number of pulses is depicted in Fig. 2c–m. From this figure, periodic surface structures with perpendicular orientation to the polarization of the laser beam and periodicity of 0.9 μm were produced for a number of pulses between 10 and 100 for all energy levels used in the experiment. Considering characteristic size and orientation of these structures and their periodicity (comparable with the laser source wavelength of 1030 nm), these structures can be identified as LSFL [9]. The ripple structures are deeper and more pronounced with the increase in a number of pulses, reaching maximum depth of 12 μm for 100 pulses and 3 mJ. However, for a higher number of pulses (close to 100), the heat accumulation leads to melting and ripples starts to break in the highest intensity regions in the center part of interference maxima positions. It can be observed especially in the

case of higher applied pulse energy, as depicted in Fig. 2m. During the first pulses, ripple structure oriented perpendicularly to LSFL and with periodicity of ~470 nm, which is approximately the half of LSFL can be observed in Fig. 2f, and j. This ripple structure can be referred as HSFL [9]. For pulse energy of 1 mJ, first pulses were below ablation threshold and therefore HSFL were fabricated only for more than 10 applied laser pulses in a combination with LSFL, as shown in Fig. 2c. No structures were observed for a lower number of pulses or lower pulse energies. Therefore, 1 mJ and 10 pulses can be considered as a threshold for LSFL and HSFL, as both can be observed in Fig. 2c.

In the following experimental step, interference patterns were stitched over large area to produce surfaces containing HSFL and LSFL. The LSFL example is depicted in Fig. 3.

LSFL were produced with 2 mJ and 50 pulses in the interference patterned area of 1.1 mm in diameter containing ~1520 spots fabricated in 50 ms and HSFL with 3 mJ and 5 pulses on the area of 0.9 mm containing ~1016 spots fabricated in 5 ms. The crater diameter was 21 μm and 17 μm with the ripple depth of 2.4 μm and 0.2 μm for LSFL and HSFL, respectively. In both cases, 30% overlap between interference areas was found to be the best for seamless and homogeneous stitching, resulting in a fabrication speed of 10 cm^2/min for LSFL and 68 cm^2/min for HSFL. To further increase the processing speed, the 1 kHz laser system will be replaced by 50 kHz HiLASE Perla laser maintaining the same pulse energy. In such case, the processing speed may be upscaled to 0.05 m^2/min and 0.34 m^2/min for LSFL and HSFL, respectively, which is comparable with the world-record in nanosecond DLIP structuring of stainless steel [20]. In addition, the indisputable advantage of this large-beam interference processing technique is the scalability. The interference area diameter can be further increased to reach higher throughputs, if there is a sufficient laser power available.

Wettability measurements of all laser treated samples showed superhydrophilic behaviour with CA below 5° (CA of plane untreated surface is (82 ± 3)°). In the following step, laser treated samples were placed in high vacuum (10^{-7} Pa) for 4 h to promote favourable chemical changes [21]. Both LSFL and HSFL surfaces were found to be superhydrophobic after the vacuum treatment with CA of (164 ± 3)° and (155 ± 3)°, respectively. These results are in line with our previous findings [21,22] - The hydrophilicity of freshly laser processed samples is the outcome of high temperature oxides formed during the laser treatment. On the other hand, high contact angles are the result of the dominant presence of non-polar hydrocarbons together with convenient geometry of hierarchical microstructures (microcraters and ripples), which are especially suitable for stable superhydrophobic surfaces [22,23]. The difference in contact angle for HSFL and LSFL can be explained by Casse-Baxter model [24]. According to this model, hydrophobic character can be increased with the surface roughness due to surface microstructures which can act as micro-reservoirs able to keep air pockets when a droplet is deposited on the surface. In case of shallow HSFL water can partially penetrate air trapped between the structures resulting in lower apparent contact angle, especially for larger droplets with volume above 4 μl [21].

In addition, the structure size is small enough to act a diffraction grating, as depicted in the inset of Fig. 3. Therefore, this technique demonstrates the potential for rapid laser fabrication of superhydrophobic surfaces or security diffractive elements.

4. Conclusion

A combination of optimized laser parameters and four beam interference allow to produce LIPSS-structured microcraters simultaneously. By shifting the interference and focal plane, the interference area can be increased well above the diffraction limit and thus significantly improve the fabrication speed of LIPSS-based functional surfaces. Stitching interference areas over larger surfaces was demonstrated with parameters suitable for HSFL and LSFL. HSFL were produced by only 5 consecutive laser pulses in area of 0.9 mm in diameter at once resulting
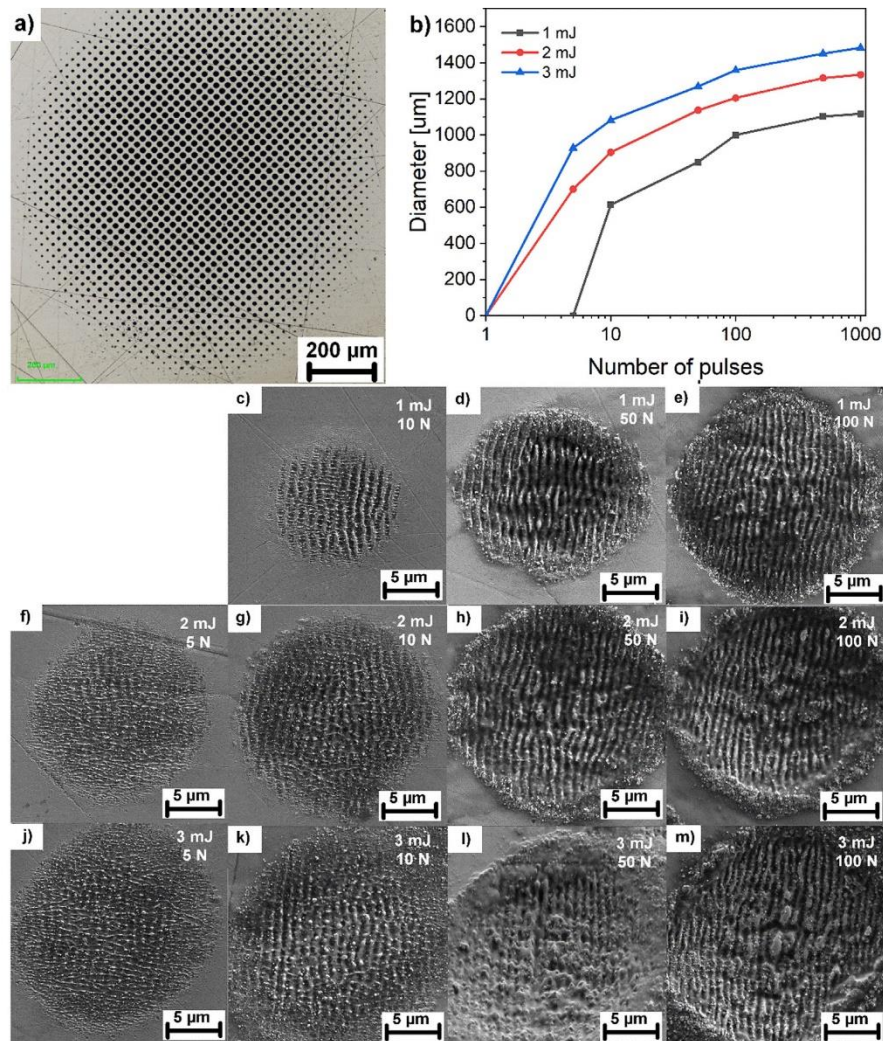
3

Fig. 2. (a) Overview of the four beam interference pattern after exposition to 100 consecutive pulses with pulse energy of 1 mJ. (b) Dependence of interference area diameter on the applied number of pulses N. (c-m) evolution of LIPSS formation for pulse energies in a rage of 1–3 mJ and number of pulses N in between 5 and 100.

in 1016 HSFL spots with the separation distance of 25 μm fabricated in 5 ms (203 200 spot/s). LSFL were obtained for number of pulses between 10 and 100 in an area up to 1.5 mm in diameter with the same separation distance of 25 μm. 30 400 LSFL spot/s were demonstrated with 2 mJ and 50 consecutive pulses. This resulted in a fabrication speed of 10 and 68 cm^2/min for LSFL and HSFL, respectively, showing a good potential in the production of security diffractive elements and superhydrophobic surfaces with CA of $(155 \pm 3)°$ (HSFL) and $(164 \pm 3)°$ (LSFL). The future upgrade of laser system repetition rate was also suggested to improve the fabrication speed up to 0.34 m^2/min for HSFL thus allowing ultra-fast fabrication of LIPSS-based functional surfaces.

CRediT authorship contribution statement

P. Hauschwitz: Conceptualization, Methodology, Validation, Formal analysis, Investigation, Writing - original draft, Writing - review & editing, Visualization, Project administration. **D. Jochcová:** Conceptualization, Software, Investigation, Writing - review & editing. **R. Jagdheesh:** Writing - review & editing, Supervision. **D. Rostohar:** Writing - review & editing, Supervision. **J. Brajer:** Resources, Supervision, Project administration. **J. Kopeček:** Resources. **M. Cimrman:** Resources. **M. Smrž:** Funding acquisition. **T. Mocek:** Resources, Supervision, Funding acquisition. **Antonio Lucianetti:** Funding acquisition.

Declaration of Competing Interest

The authors declare that they have no known competing financial interests or personal relationships that could have appeared to influence the work reported in this paper.
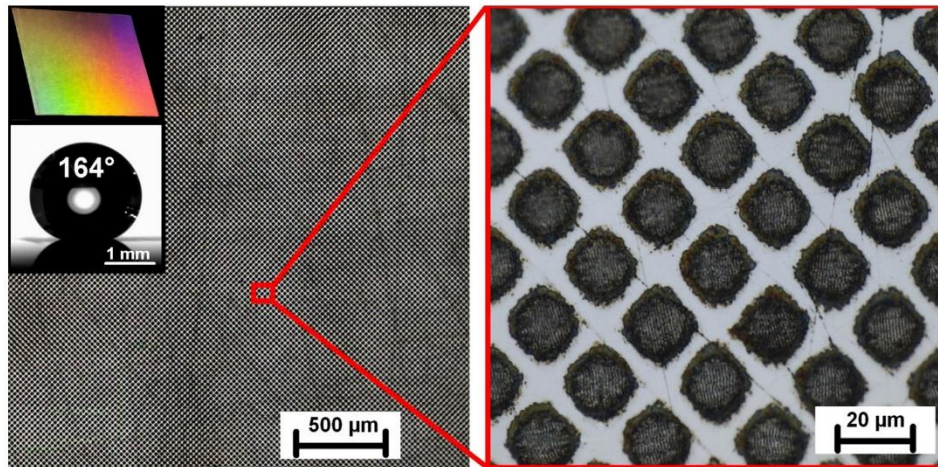
4

Fig. 3. Example of stitched four beam interference pattern over larger area with insets of diffracted light and 8 μl droplet deposited on the surface. Sample was irradiated with 2 mJ pulse energy and 50 pulses per each interference area to be stitched.

Acknowledgements

References

[1] J. Bonse, S.V. Kirner, S. Höhm, N. Epperlein, et al., Applications of laser-induced periodic surface structures (LIPSS), Laser-based Micro-and Nanoprocessing XI. International Society for Optics and Photonics, vol. 10092, 2017, p. 100920N.

[2] P. Hauschwitz, R. Jagdheesh, S. Alamri, D. Rostohar, et al., Fabrication of functional superhydrophobic surfaces on carbon fibre reinforced plastics by IR and UV direct laser interference patterning, Appl. Surf. Sci. (2019) 144817.

[3] T. Baldacchini, J.E. Carey, M. Zhou, E. Mazur, Superhydrophobic surfaces prepared by microstructuring of silicon using a femtosecond laser, Langmuir 22 (11) (2006) 4917–4919.

[4] J. Eichstädt, G. Römer, A. Huis, Towards friction control using laser-induced periodic surface structures, Phys. Procedia 12 (2011) 7–15.

[5] A. Vorobyev, C. Guo, Antireflection effect of femtosecond laser-induced periodic surface structures on silicon, Opt. Express 19 (105) (2011) A1031–A1036.

[6] A.H. Lutey, L. Gemini, L. Romoli, G. Lazzini, et al., Towards laser-textured antibacterial surfaces, Sci. Rep. 8 (1) (2018) 10112.

[7] A.Y. Vorobyev, C. Guo, Colorizing metals with femtosecond laser pulses, Appl. Phys. Lett. 92 (4) (2008) 041914.

[8] M. Smrž, O. Novák, J. Mužík, H. Turčičová, et al., Advances in high-power, ultra-short pulse DPSSL technologies at HiLASE, Appl. Sci. 7 (10) (2017) 1016.

[9] J. Bonse, J. Krüger, S. Höhm, A. Rosenfeld, Femtosecond laser-induced periodic surface structures, J. Laser Appl. 24 (4) (2012) 042006.

[10] G. Lazzini, L. Gemini, A. Lutey, R. Kling, et al., Surface Morphologies in Ultra-short Pulsed Laser Processing of Stainless-Steel at High Repetition Rate, Int. J. Precis. Eng. Manuf. (2019) 1–10.

[11] A. Lasagni, A. Manzoni, F. Mücklich, Micro/Nano Fabrication of Periodic Hierarchical Structures by Multi-Pulsed Laser Interference Structuring, Adv. Eng. Mater. 9 (10) (2007) 872–875.

[12] A.F. Lasagni, C. Gachot, K.E. Trinh, M. Hans, et al., Direct laser interference patterning, 20 years of development: from the basics to industrial applications, Laser-based micro-and nanoprocessing XI. International Society for Optics and Photonics, vol. 10092, 2017, p. 1009211.

[13] A. Rosenkranz, M. Hans, C. Gachot, A. Thome, et al., Direct laser interference patterning: tailoring of contact area for frictional and antibacterial properties, Lubricants 4 (1) (2016) 2.

[14] B. Voisiat, M. Gedvilas, S. Indrišiūnas, G. Račiukaitis, Picosecond-laser 4-beam-interference ablation as a flexible tool for thin film microstructuring, Phys. Procedia 12 (2011) 116–124.

[15] P. Hauschwitz, R. Jagdheesh, D. Rostohar, J. Brajer, et al., Nanostructure fabrication on the top of laser-made micropillars for enhancement of water repellence of aluminium alloy, Mater. Lett. (2019) 126601.

[16] J.W. Goodman, Statistical optics, Edtion ed., John Wiley & Sons, 2015.

[17] A. Maznev, T. Crimmins, K. Nelson, How to make femtosecond pulses overlap, Opt. Lett. 23 (17) (1998) 1378–1380.

[18] A.I. Aguilar-Morales, S. Alamri, A.F. Lasagni, Micro-fabrication of high aspect ratio periodic structures on stainless steel by picosecond direct laser interference patterning, J. Mater. Process. Technol. 252 (2018) 313–321.

[19] S. Alamri, A.F. Lasagni, Development of a general model for direct laser interference patterning of polymers, Opt. Express 25 (9) (2017) 9603–9616.

[20] V. Lang, T. Roch, A.F. Lasagni, World record in high speed laser surface microstructuring of polymer and steel using direct laser interference patterning, Laser-based Micro-and Nanoprocessing X. International Society for Optics and Photonics, vol. 9736, 2016, p. 97360Z.

[21] P. Hauschwitz, R. Jagdheesh, D. Rostohar, J. Brajer, et al., Hydrophilic to ultrahydrophobic transition of Al 7075 by affordable ns fiber laser and vacuum processing, Appl. Surf. Sci. 505 (2020) 144523.

[22] R. Jagdheesh, et al., Robust fabrication of μ-patterns with tunable and durable wetting properties: hydrophilic to ultrahydrophobic via a vacuum process, J. Mater. Chem. A 5 (15) (2017) 7125–7136.

[23] K. Liu, L. Jiang, Bio-inspired design of multiscale structures for function integration, Nano Today 6 (2) (2011) 155–175.

[24] A. Cassie, S. Baxter, Wettability of porous surfaces, Trans. Faraday Soc. 40 (1944) 546–551.

5

5.5 Journal article E. Large-beam picosecond interference patterning of metallic substrates

In this paper, the author introduces a method for efficient use of high-energy 1.7 ps HiLASE Perla laser system for two beam interference patterning. The new method permits the production of micron and sub-micron sized features on a treated surface with increased processing throughputs by enlarging the overlapped beam area. The formation of a variety of functional surface micro and nanostructures and their combination are reported on stainless steel, invar and tungsten with the maximum fabrication speed of 206 cm^2/min.

Author contribution

In a work related to the production of this journal paper, P. Hauschwitz designed and build interference processing station, planned, designed and carried out all experiments with the help of D. Jochcová. P. Hauschwitz also analysed SEM data with J. Kopeček and interpreted results. P. Hauschwitz was responsible for drafting the manuscript and communication with the journal. Detail authors individual contributions are listed in table 5.

Term	Authors' individual contributions
Conceptualization	P. Hauschwitz, D. Jochcová
Methodology	P. Hauschwitz
Software	D. Jochcová
Validation	P. Hauschwitz
Formal analysis	P. Hauschwitz
Investigation	P. Hauschwitz, D. Jochcová
Resources	T. Mocek, J. Brajer, J. Kopeček, M. Cimrman
Writing - Original Draft	P. Hauschwitz
Writing - Review & Editing	P. Hauschwitz, D. Rostohar, J. Radhakrishnan, D. Jochcova, J. Kopeček, M. Cimrman, M. Smrž, A. Lucianetti
Visualization	P. Hauschwitz
Supervision	J. Radhakrishnan, D. Rostohar, J. Brajer, J. Kopeček, M. Cimrman, M. Smrž, A. Lucianetti, T. Mocek
Project administration	P. Hauschwitz, J. Brajer
Funding acquisition	T. Mocek, M. Smrž, A. Luccianetti

Table 5: Credit author statement - Large-beam interference micro and nanostructuring of metallic substrates

Large-Beam Picosecond Interference Patterning of Metallic Substrates

Petr Hauschwitz [1,2,*], **Dominika Jochcová** [1,2], **Radhakrishnan Jagdheesh** [1], **Martin Cimrman** [1,2], **Jan Brajer** [1], **Danijela Rostohar** [1], **Tomáš Mocek** [1], **Jaromír Kopeček** [3], **Antonio Lucianetti** [1] and **Martin Smrž** [1]

[1] HiLASE Centre, Institute of Physics, Czech Academy of Sciences, Za Radnici 828,
    25241 Dolni Brezany, Czech Republic; dominika.jochcova@hilase.cz (D.J.); r.jagdheesh@hilase.cz (R.J.);
    martin.cimrman@hilase.cz (M.C.); jan.brajer@Hilase.cz (J.B.); danijela.rostohar@hilase.cz (D.R.);
    tomas.mocek@hilase.cz (T.M.); antonio.lucianetti@hilase.cz (A.L.); martin.smrz@hilase.cz (M.S.)
[2] Faculty of Nuclear Sciences and Physical Engineering, Czech Technical University in Prague, Brehova 7,
    115 19 Prague, Czech Republic
[3] Institute of Physics of the Czech Academy of Sciences, Na Slovance 2, 182 21 Prague, Czech Republic;
    kopecek@fzu.cz
* Correspondence: petr.hauschwitz@hilase.cz

Abstract: In this paper, we introduce a method to efficiently use a high-energy pulsed 1.7 ps HiLASE Perla laser system for two beam interference patterning. The newly developed method of large-beam interference patterning permits the production of micro and sub-micron sized features on a treated surface with increased processing throughputs by enlarging the interference area. The limits for beam enlarging are explained and calculated for the used laser source. The formation of a variety of surface micro and nanostructures and their combinations are reported on stainless steel, invar, and tungsten with the maximum fabrication speed of 206 cm²/min. The wettability of selected hierarchical structures combining interference patterns with 2.6 μm periodicity and the nanoscale surface structures on top were analyzed showing superhydrophobic behavior with contact angles of 164°, 156°, and 150° in the case of stainless steel, invar, and tungsten, respectively.

Keywords: Perla laser; interference patterning; LIPSS; superhydrophobicity

1. Introduction

Fabrication of a functional surface with micro and nanostructures is a popular topic in science and industry. The surface functional performance often originates in hierarchical structures composed of micro and nanoscale features assembled into complex structures [1]. Their advantageous structure–property–performance relations have inspired extensive efforts for the study and development of methods for their effective replication. Among different type of structures, strategies for the fabrication of multi-scale structures have been the most extensively developed. Such structures can enhance or completely modify the original surface properties to achieve anti-icing [2], anti-corrosion [3], anti-bacteria [4], or superhydrophobic [5,6] properties.

Among a large variety of techniques for replicating naturally occurring microstructures, including chemical vapor deposition [7], chemical etching [8], sol-gel [9], plasma treatments [10], lithography [11], or electrodeposition [12], laser surface texturing provides a flexible, fast, and environmentally friendly approach for the high precision fabrication of desired micro and nanogeometries [13,14]. However, commonly used direct laser writing techniques, utilizing only one laser beam in a combination with a galvo scanner, may not satisfy the high industry demands for the treatment of large area in a short time. This is especially difficult to fulfil in the case of high-resolution

micron scale structuring. Additionally, the increase in the average power of the ultrashort laser systems in recent years [15] were not reflected in the effectiveness of micro and nanoprocessing, as only a small percentage of the available laser power is used for processing to maintain high quality and avoid melting and thermal effects.

Direct laser interference patterning (DLIP) provides a solution to these issues by overlapping two or more coherent laser beams on the surface to directly imprint an interference pattern. If enough pulse energy is used, a large variety of materials can be processed at interference maxima positions, including metals [16–18], dielectrics [19,20], and even composite materials [21]. This allows the patterning of an area on the order of several tens of μm in diameter in a single irradiation step and with resolutions below the diffraction limit of the initial beam. The interference pattern can be controlled by the polarization, number of laser beams, and their incidence angle as well as by the wavelength, intensity, and phase difference. However, micron-sized pattern periodicity requires lenses with a short focal length to reach a high enough angle between overlapping beams. Consequently, potential throughputs are limited by the diameter of interference area, which is often on the order of a few tens of microns [16,21,22].

The choice of a laser system and its pulse duration plays an important role. Nanosecond systems are often used due to the less demanding DLIP setup precision and more flexibility in the setup design in general. The interference area can be larger compared to ultrashort pulses [23]. However, a lower temporal energetic density and the melting and thermal effects connected with nanosecond pulses limits the minimal achievable structure size and quality [16,24]. In addition, high beam quality and spatial coherence are also important parameters for high-quality DLIP structuring.

In line with that, this research presents a simple method that can increase the interference area diameter and preserve the high-resolution structures at the same time without any change in the optical setup. In particular, the high beam quality, ultrashort pulse duration below 2 ps, and high pulse energy of a HiLASE Perla laser in a combination with a novel technique of enlarging the interference area within the boundaries of the laser system parameters are novel aspects compared to the more commonly applied two beam configurations [16,21,24]. By utilizing this method, high throughput fabrication of micron and sub-micron sized features is demonstrated on several metallic materials, including stainless steel, commonly used in industrial contexts, such as medical implants, precision mechanics, marine applications, and food handling; tungsten, with applications in the production of hard materials and coatings; and invar, used in electronics and precision mechanical systems where a high degree of dimensional stability is required under a wide range of temperatures.

2. Principles of Interference Patterning

In order to predict the energy distribution inside the interference area, as well as the effective overlapped beam size for interference, basic simulation was performed using the following equations.

Considering the wave approximation, the total complex amplitude of the electric field in a position $\vec{r}$ is given by a superposition of contributions of individual beams i.e., plane waves.

$$I(\vec{r}) \propto \left(\sum_{i=1}^{N} \vec{E}_i(\vec{r}) \right)^2 \tag{1}$$

where $\vec{r}$ is the coordinate vector, t is the time, i is the index of interfering beams, N is the number of beams, and $\vec{E}_i$ is the electrical field of i beam, which can be expressed as follows:

$$\vec{E}_i = \vec{E}_{0i} \cos(\vec{k}_i \cdot \vec{r} - \omega t + \varphi_i) \tag{2}$$

where $|\vec{E}_{0i}|$ is the amplitude of i wave, $|\vec{k}_i| = 2\pi/\lambda$ is the wave vector of the i wave, λ is the laser wavelength, ω is the frequency of radiation, and φ_i is the phase of the i wave.

The total intensity in a position $\vec{r}$ is proportional to the squared module of the complex intensity vector

$$I(\vec{r}) \approx \left| \vec{E}(\vec{r}) \right|^2. \tag{3}$$

In the case that all interfering beams have the same frequency, periodical intensity field is formed, and the equations can be simplified to [25]:

$$I(\vec{r}) \propto \frac{1}{2} \sum_{i=1}^{N} \left| \vec{E}_{0i} \right|^2 + \sum_{j<1}^{N} \sum_{i=1}^{N} \vec{E}_{0i} \cdot \vec{E}_{0j} \cos \left(\vec{k}_i \cdot \vec{r} - \vec{k}_j \cdot \vec{r} + \varphi_i - \varphi_j \right). \tag{4}$$

As observed from Equation (4), the interference period depends on the incident angle between the beams and on the wavelength. Therefore, the lateral dimensions of the interference pattern (spatial period Λ) can be controlled by the angle θ between incident laser beams [26]. For two beams, the spatial period Λ can be calculated using Equation (5):

$$\Lambda = \frac{1}{2} \frac{\lambda}{\sin(\theta/2)}. \tag{5}$$

Thus, structures with micro and sub-micrometer periodicity can be reached with common laser systems emitting at ~1 μm without any special objectives.

Good agreement between simulations (Equation (4)) and the pattern fabricated on a stainless-steel surface is demonstrated in Figure 1.
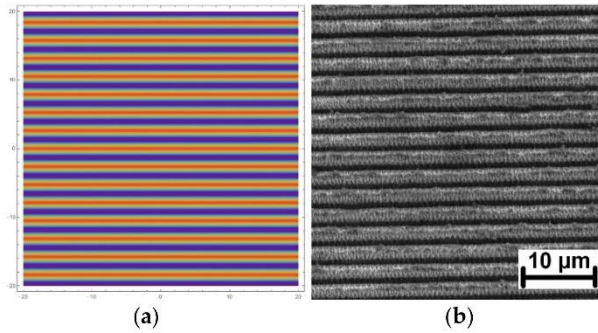

Figure 1. (**a**) Calculated pattern for two beam interference with a periodicity of 2.64 μm; (**b**) SEM image of the pattern fabricated on stainless steel with the same periodicity.

Higher throughputs can be reached with a larger beam diameter. However, the maximal reach of the interference area inside the overlapped beam region is limited by the pulse duration. For two beams overlapping at angle θ, the diameter of the interference area influenced by the pulse duration can be estimated by Equation (6) [23]:

$$d \approx \frac{c\tau}{\sin(\theta/2)} \tag{6}$$

where c is the speed of light, and τ is the pulse duration.

Another important aspect of the pulse duration relates to the heat diffusion length l_H, which limits the minimal achievable structure size due to melting [16]:

$$l_H = \sqrt{\frac{K \cdot \tau}{\rho \cdot c_p}} \tag{7}$$

where K is the thermal conductivity, ρ is the material density, and c_p is the specific heat capacity. These material constants are shown in Table 1 for the materials used in this research.

Therefore, there is a tradeoff between the interference area and heat diffusion length. The shorter the pulse duration, the finer the structures that can be produced, but, at the same time, the smaller the area of interference. According to Equation (7), the heat diffusion length for tungsten is 2.6 μm for a 100 ns pulse duration and only 3 nm in the case 100 fs. The corresponding diameter of the interference area d is 153 m and 154 μm for 100 ns and 100 fs pulses (θ = 22.5°), respectively.

Table 1. Material constants provided by the supplier (Goodfellow GmbH) and heat diffusion lengths calculated for 100 ns and 100 fs pulse durations.

Material Constant	Stainless Steel	Invar	Tungsten
K [W m^{-1}K^{-1}]	16.3	13	173
ρ [Kg m^3]	7960	8000	19300
c_p [Kg K]	502	515	133
$l_{H\,\tau=100\,ns}$ [nm]	639	562	2596
$l_{H\,\tau=100\,fs}$ [nm]	1	1	3

3. Materials and Methods

Different metallic materials, including stainless steel 316L, tungsten, and invar (FeNi36), provided by Goodfellow GmbH, were used for interference patterning. The sample thickness was 5 mm in the case of stainless steel and 0.2 mm in the case of invar and tungsten. A ytterbium-based diode pumped solid state laser system Perla from HiLASE emitting ultrashort pulses with a pulse duration of 1.7 ps and M² of 1.2 at 1030 nm wavelength was used for DLIP processing. The incident laser beam was split into two beams by a diffractive optical element (DOE) with a separation angle of 3.97° (Holo/Or Ltd.). In the next step, the beams were parallelized by a prism and focused on a sample using a lens with a 60 mm focal length. The prism position was adjusted to reach the periodicity of 2.64 μm (θ = 22.5°). The illustration of the experimental setup is shown in Figure 2.
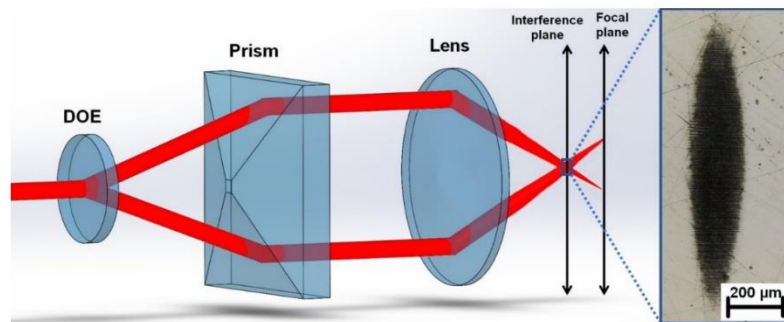

Figure 2. Illustration of the experimental setup with a marked shift between the interference and focal plane and with an inset of the elongated spot shape fabricated on a stainless-steel sample.

The pulse duration of 1.7 ps implies a large enough area for interference with diameter of 2.6 mm together with a heat diffusion length below 12 nm for all selected materials. Another advantage of pulse duration below ~10 ps is the possibility to produce laser induced periodic surface structures (LIPSS) on top of DLIP geometry and further enhance the functional properties of the structured surface.

To increase the throughput, the divergence of the initial laser beam was modified by telescope causing a shift between the interference plane and the focal plane, thus, elongating the interference area and reshaping it into an elliptical area due to the high angle θ (Figure 2). The divergence was tuned with the goal of reaching a major ellipse diameter of ~1 mm, which is well below the calculated limit of 2.6 mm and allows the use of reasonable pulse energies. Pulse energy up to 3 mJ and a 1 kHz repetition rate were used for this research.

Immediately after patterning, the samples were stored in a high vacuum (10^{-7} Pa) for 4 h to promote favorable chemical changes and decrease the transition time to reach a superhydrophobic state. The surface morphology was investigated using a scanning electron microscope, Tescan FERA 3 at electron energy of 5 kV, and a laser scanning confocal microscope, Olympus OLS5000 (Olympus Corporation, Tokyo, Japan). The wettability was evaluated by means of static contact angle measurements of 8 μL sessile droplets using the optical contact angle measuring device OCA 15EC (Data Physics Instruments, Filderstadt, Germany).

4. Results and Discussion

Figure 3 presents the evolution of the major ellipse diameter with the applied pulse energy for 1000 consecutive laser pulses. As can be observed, a higher amount of accumulated energy resulted in a larger diameter for all materials and, thus, potentially improves the fabrication speed. Variations of the major ellipse diameter for the same applied laser parameters but different materials were caused by the different ablation thresholds of each material. The largest major diameter of 1.40 mm was achieved for invar irradiated with 3 mJ (2.44 J/cm²) and 1000 consecutive laser pulses. With the same laser parameters, the major diameters of stainless steel and tungsten were 1.28 mm and 1.15 mm, respectively.
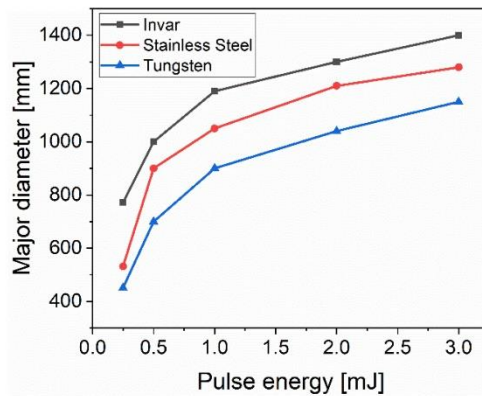

Figure 3. The major diameter of the elliptical interference area with a dependence on pulse energy.

However, the morphology of the produced structures also changed with the increase in pulse energy. Three different types of structures were identified at energy levels between 0.5 mJ (0.41 J/cm²) and 3 mJ (2.44 J/cm²) for samples irradiated with 1000 consecutive laser pulses, as depicted in Figure 4 for stainless steel.

For pulse energies below 1 mJ (0.81 J/cm²), a periodic pattern in the form of lines separated by 2.64 μm were fabricated with a groove depth of approximately 1 μm (Figure 4a). In addition, the whole surface was covered with nanoscale protrusions originating from melting and melt ejections on the top surface layers (Figure 4d), thus, generating dual-scale hierarchical structures. At pulse energies close to 1 mJ, the grooves began to break (Figure 4b). The amount of nanoscale protrusions decreased. The highest applied pulse energy of 3 mJ resulted in a formation of ~4 μm wide micropillars with a significantly reduced number of nanoscale protrusions. The appearance of micropillars can be explained by altering the energy distribution of incoming laser pulse on broken groove structures. Broken grooves may act as precursor sites, scattering the incoming light, thus, activating the preferential valley ablation between precursor sites. In the following step, conical-shaped micropillars were formed and grew with incoming laser pulses due to melt flow from the valleys towards the micropillar peaks. The melt flow is driven by thermal gradients caused by inhomogeneous energy distribution induced by the surface geometry. This can be evidenced by smooth micropillar walls with a minimum amount of nanostructures indicating the melt flow on the surface (Figure 4f). Similar structures were observed on nickel irradiated by a femtosecond laser system [27].

As presented in Figure 5, it was possible to manufacture similar surface structures on invar (Figure 5a–c) and tungsten (Figure 5d–f) by slightly adjusting the pulse energy in the rage of 0.3 mJ (0.24 J/cm²) to 2 mJ (1.62 J/cm²) for invar and 0.5 mJ (0.41 J/cm²) to 3 mJ (2.44 J/cm²) for tungsten. Comparing the structure evolution, the morphology of invar structures followed the same trend as stainless-steel structures. The exception is the distinctive pulse energy levels, which were lower for invar. Contrarily, the amount of nanoscale protrusions covering the top surface was significantly lower in the case of tungsten. Conical shaped micropillar structures were not achieved on tungsten.

With increasing pulse energy, the periodical structures start to break, however, further increases lead to melting and structure collapse instead of the formation of micropillars. In addition, the surface is covered with splashed and resolidified melt material in the case of the highest applied pulse energy.
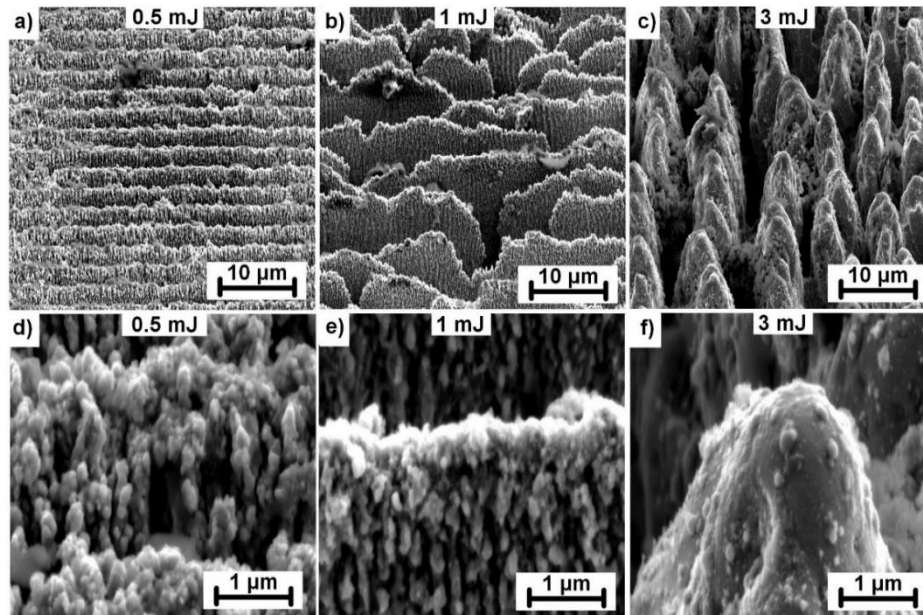

Figure 4. Structure evolution on a stainless-steel surface with increased pulse energy and 1000 consecutive laser pulses. Detail images with higher magnification are shown in the second row with the corresponding pulse energy. All images were captured with the sample tilted 55°.
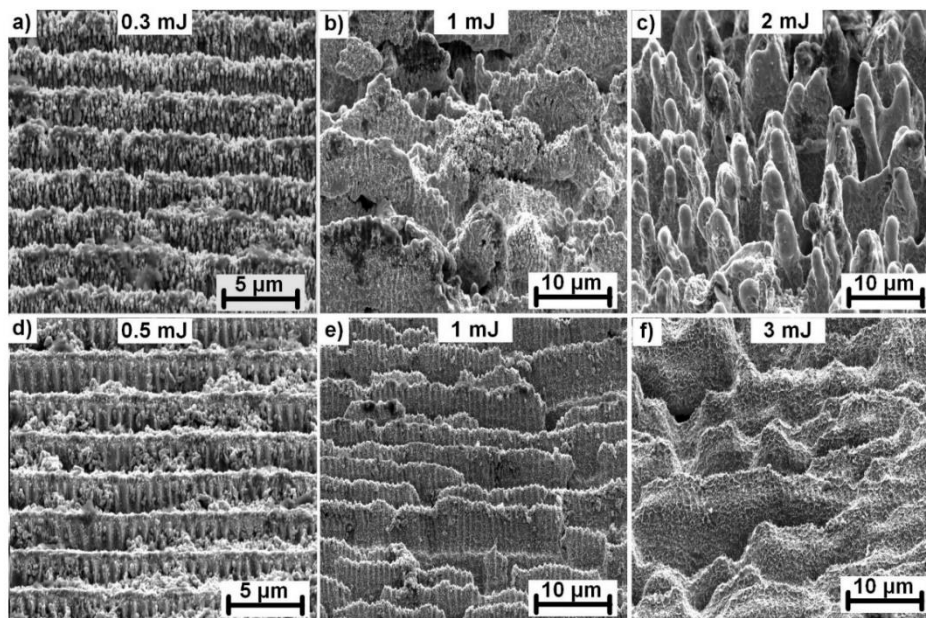

Figure 5. Structure evolution in Invar (**a–c**) and tungsten (**d–f**) with increasing pulse energy. The surface was irradiated with 1000 consecutive laser pulses. All images were captured with the sample tilted 55°.

Based on these results, a detailed analysis of the structure morphology was carried out by changing the number of pulses as well as the pulse energy. Consequently, new surface morphologies were observed as depicted in Figure 6.
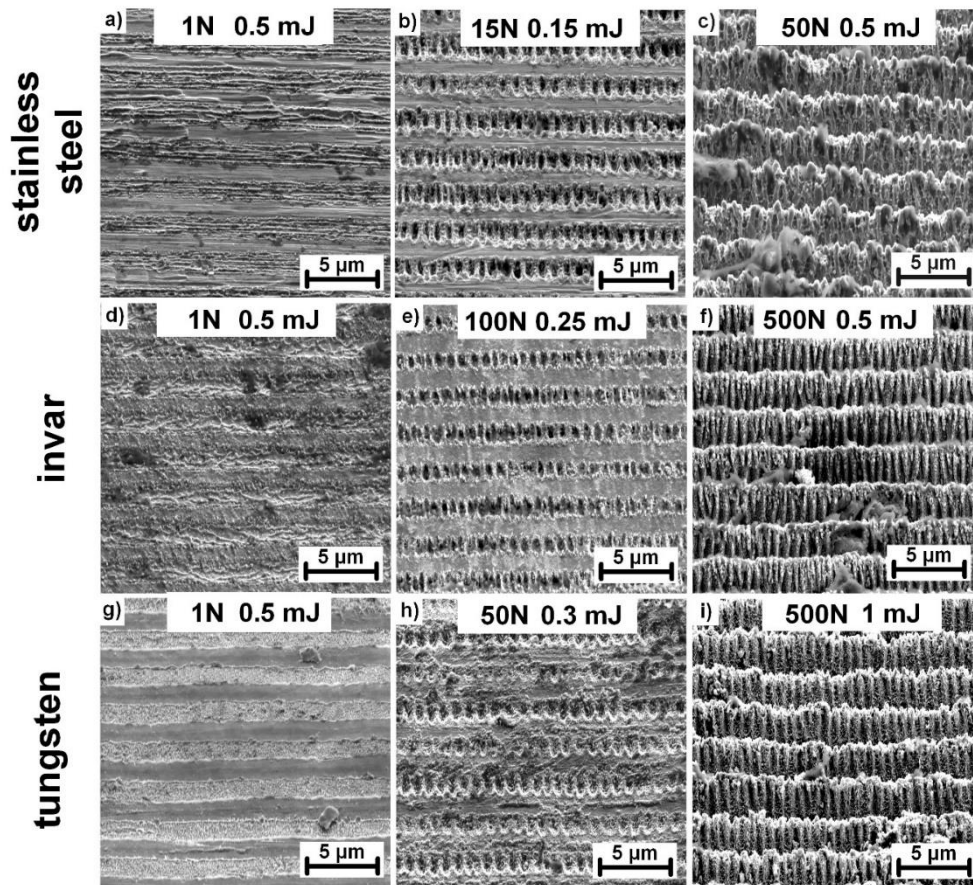

Figure 6. Different surface morphologies achieved by variations in the pulse energy and number of pulses (N) on invar (**a–c**), stainless steel (**d–f**), and tungsten (**g–i**). All images were captured with the sample tilted 55°.

For a single pulse treatment, periodically arranged lines with lateral spacing of ~400 nm were observed with the orientation parallel to the polarization of the laser beam. Considering the characteristic size and orientation of these structures and parameters of the laser source (1030 nm, 1.7 ps), these structures can be identified as high spatial frequency LIPSS (HSFL) [28]. They are produced only at the interference maxima positions, thus, with an adjustable separation distance following the interference period, HSFL were observed in the case of invar and stainless steel, as depicted in Figure 6a,d. HSFL were more pronounced in the case of invar for pulse energies in a range of 0.25 mJ (0.2 J/cm²) to 0.5 mJ (0.41 J/cm²) with a lower amount of melting. In the case of stainless steel, substantial melting at the interference maxima disrupted the straight lines. Contrarily, melting and melt ejections were the main mechanisms observed for the single pulse treatment of tungsten, which prevented the formation of HSFL, however, showing promise for melt induced nanostructure fabrication. Therefore, a more detailed look at the melt evolution is presented in Figure 7.

A higher number of applied pulses resulted in another set of periodical arrays formed at the interference maxima positions. These can be referred to as low spatial frequency LIPSS (LSFL) due to the perpendicular orientation of the laser beam polarization and periodicity of ~870 nm, which is

comparable with the used wavelength [28]. LSFL can be observed for all treated materials with 50 and more consecutive pulses at pulse energies of 0.15 mJ (0.12 J/cm²) for invar and 0.25 mJ (0.2 J/cm²) and 0.3 mJ (0.24 J/cm²) for stainless steel and tungsten, respectively.
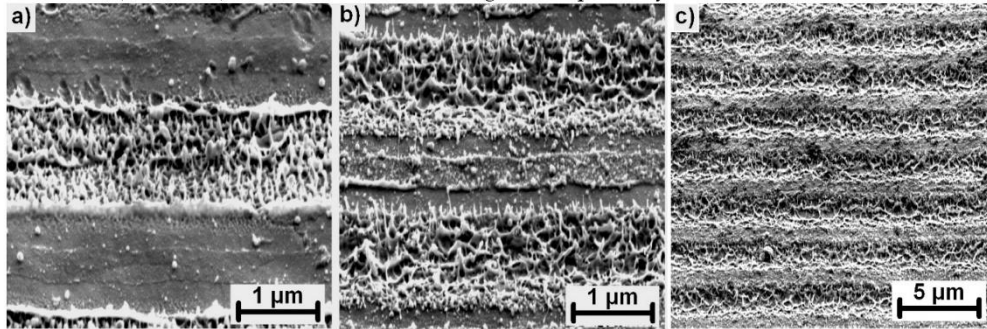

Figure 7. High magnification images of a tungsten surface irradiated with 1 mJ (0.81 J/cm²) and a single pulse (**a**), 5 pulses (**b**), and 10 pulses (**c**). All images are captured with the sample tilted 55°.

As observed in Figure 7, a detailed look at the surface morphology on tungsten during the first few pulses revealed a different structure evolution. HSFL were not produced during the single pulse irradiation. The material appeared to be melted with random nanostructures originating from rapid melting and melt ejections toward the laser source, followed by quick resolidification forming randomly organized nanopillars with dimensions below 100 nm (Figure 7a). The following pulses caused remelting and merging of these nanostructures (Figure 7b). With the increased number of pulses, these structures were agglomerated and flattened until they covered the whole surface as shown in Figure 7c or Figure 5f.

To demonstrate the potential as a functional surface, the wettability of selected surfaces was tested. Tests were performed on all materials covered by similar structures composed of interference pattern with 2.6 μm periodicity covered with nanoscale protrusions on top with the same parameters as shown in Figure 4a for stainless steel, in Figure 5a for invar, and in Figure 5d for tungsten. All processed samples were placed for 4 hours into a vacuum chamber with the high vacuum of (10^{-7} Pa) to promote favorable chemical changes that may significantly decrease the transition time required to reach a superhydrophobic state. More details about the vacuum processing technique can be found elsewhere [29]. After that, the wettability was measured using the sessile drop technique with a droplet volume of 8 μL.

All samples were found to be superhydrophobic with contact angles of 164°, 156°, and 150° for stainless steel, invar, and tungsten, respectively, as shown in Figure 8. Therefore, hierarchical structures combining micro and nanoscale surface features exhibited excellent water resistance compared to untreated surfaces with a contact angle of 90°. This phenomenon can be explained by the Cassie–Baxter model [30] describing a rough surface that is able to trap air between surface features when a droplet is deposited on the surface. As a result, air trapped in between surface features prevents the water droplet from penetrating inside the valleys. Consequently, the water droplet is suspended only on the top of the microscale features, keeping the valleys dry and, thus, enhancing the water repellency.

Figure 8. The wettability measurements of laser processed samples after vacuum treatment.

The fabrication speed of introduced large-beam interference patterning technique reached 0.34 cm^2/min (1000 consecutive pulses) and 206 cm^2/min (single pulse). To reach a homogeneous pattern distribution, 30% pulse-to-pulse overlap (the spot center distance dived by the spot diameter) was experimentally found to be the best for seamless stitching over larger areas. Considering the 1 kHz repetition rate of the used laser system, these throughputs can be scaled up in orders of magnitude together with the repetition rate. For example, HiLASE Perla C [15] operated at 100 kHz and a 3 mJ pulse energy may theoretically speed up those fabrication speeds toward 34 cm^2/min and 2.06 m^2/min. The important benefit of this large-beam interference approach is the scalability. With enough laser power available, the area of interference can be further increased to reach higher throughputs. Thus, this technique shows promise for future applications of rapid large-scale surface functionalization.

5. Conclusions

A technique for increasing the throughput and efficiency of DLIP was introduced. By changing the beam divergence, the elliptical interference area with a major diameter above 1 mm and interference maxima in a form of lines oriented perpendicular to the major diameter was demonstrated. In addition, we used the basic principles of interference and performed calculations to determine the limits of the interference area and its dependence on laser parameters. A simple change in the laser parameters, including the pulse energy and number of pulses led to the fabrication of a variety of micro and nanostructures and their combinations produced in a single step on several metallic substrates.

Pulse energies around 0.5 mJ with 1000 consecutive laser pulses resulted in a periodical groove structure covered by nanoscale protrusions, began to break at around 1 mJ of applied pulse energy and formed conical micropillar structures when the pulse energy increased above this level. Further examination revealed the parameters for the fabrication of HSFL, LSFL, and melt-induced nanostructures formed at the interference maxima positions, with an adjustable separation distance following the interference period. The fabrication speed of micro and nanostructured surfaces reached up to 206 cm^2/min showing promises for the future rapid large-scale fabrication of functional surfaces by high-power laser systems. In addition, surfaces covered by DLIP-induced groove structures combined with nanoscale protrusions exhibited superhydrophobic properties after vacuum treatment with contact angles of 164°, 156°, and 150° in the case of stainless steel, invar, and tungsten, respectively.

References

1. Liu, K.; Jiang, L. Bio-inspired design of multiscale structures for function integration. *Nano Today* **2011**, *6*, 155–175.
2. Guo, P.; Zheng, Y.; Wen, M.; Song, C.; Lin, Y.; Jiang, L. Icephobic/Anti-Icing Properties of Micro/Nanostructured Surfaces. *Adv. Mater.* **2012**, *24*, 2642–2648.
3. Zhang, F.; Liu, H.; Suebka, C.; Liu, Y.; Liu, Z.; Guo, W.; Cheng, Y.; Zhang, S.; Li, L. Corrosion behaviour of laser-cleaned AA7024 aluminium alloy. *Appl. Surf. Sci.* **2018**, *435*, 452–461.

4. Lutey, A.H.A.; Gemini, L.; Romoli, L.; Lazzini, G.; Fuso, F.; Faucon, M.; Kling, R. Towards laser-textured antibacterial surfaces. *Sci. Rep.* **2018**, *8*, 10112.

5. Hauschwitz, P.; Jagdheesh, R.; Rostohar, D.; Brajer, J.; Kopeček, J.; Jiřícek, P.; Houdková, J.; Mocek, T. Hydrophilic to ultrahydrophobic transition of Al 7075 by affordable ns fiber laser and vacuum processing. *Appl. Surf. Sci.* **2020**, *505*, 144523.

6. Hauschwitz, P.; Jagdheesh, R.; Rostohar, D.; Brajer, J.; Kopeček, J.; Jiříček, P.; Houdková, J.; Mocek, T. Nanostructure fabrication on the top of laser-made micropillars for enhancement of water repellence of aluminium alloy. *Mater. Lett.* **2019**, *256*, 126601.

7. Kamal, S.A.A.; Ritikos, R.; Rahman, S.A. Wetting behaviour of carbon nitride nanostructures grown by plasma enhanced chemical vapour deposition technique. *Appl. Surf. Sci.* **2015**, *328*, 146–153.

8. Cremaldi, J.; Bhushan, B. Fabrication of bioinspired, self-cleaning superliquiphilic/phobic stainless steel using different pathways. *J. Colloid Interface Sci.* **2018**, *518*, 284–297.

9. Lakshmi, R.V.; Basu, B.J. Fabrication of superhydrophobic sol–gel composite films using hydrophobically modified colloidal zinc hydroxide. *J. Colloid Interface Sci.* **2009**, *339*, 454–460.

10. Schröder, K.; Meyer-Plath, A.; Keller, D.; Besch, W.; Babucke, G.; Ohl, A. Plasma-induced surface functionalization of polymeric biomaterials in ammonia plasma. *Contrib. Plasma Phys.* **2001**, *41*, 562–572.

11. Shiu, J.Y.; Kuo, C.W.; Chen, P.; Mou, C.Y. MOU Fabrication of tunable superhydrophobic surfaces by nanosphere lithography. *Chem. Mater.* **2004**, *16*, 561–564.

12. Liu, Y.; Li, S.; Wang, Y.; Wang, H.; Gao, K.; Han, Z.; Ren, L. Superhydrophobic and superoleophobic surface by electrodeposition on magnesium alloy substrate: wettability and corrosion inhibition. *J. Colloid Interface Sci.* **2016**, *478*, 164–171.

13. Liu, X.; Du, D.; Mourou, G. Laser ablation and micromachining with ultrashort laser pulses. *IEEE J. Quantum Electron.* **1997**, *33*, 1706–1716.

14. Vorobyev, A.Y.; Guo, C. Direct femtosecond laser surface nano/microstructuring and its applications. *Laser Photonics Rev.* **2013**, *7*, 385–407.

15. Smrž, M.; Novák, O.; Mužík, J.; TurČiČová, H.; Chyla, M.; Nagisetty, S.S.; Vyvlečka, M.; Roškot, L.; Miura, T.; Černohorská, J.; et al. Advances in high-power, ultrashort pulse DPSSL technologies at HiLASE. *Appl. Sci.* **2017**, *7*, 1016.

16. Aguilar-Morales, A.I.; Alamri, S.; Lasagni, A.F. Micro-fabrication of high aspect ratio periodic structures on stainless steel by picosecond direct laser interference patterning. *J. Mater. Process. Technol.* **2018**, *252*, 313–321.

17. Vercillo, V.; Tonnicchia, S.; Romano, J.; García-Girón, A.; Aguilar-Morales, A.I.; Alamri, S.; Dimov, S.S.; Kunze, T.; Lasagni, A.F.; Bonaccurso, E. Design Rules for Laser-Treated Icephobic Metallic Surfaces for Aeronautic Applications. *Adv. Funct. Mater.* **2020**, *30*, 1910268.

18. Milles, S.; Soldera, M.; Kuntze, T.; Lasagni, A.F. Characterization of self-cleaning properties on superhydrophobic aluminum surfaces fabricated by direct laser writing and direct laser interference patterning. *Appl. Surf. Sci.* **2020**, *525*, 146518.

19. Alamri, S.; Aguilar-Morales, A.I.; Lasagni, A.F. Controlling the wettability of polycarbonate substrates by producing hierarchical structures using direct laser interference patterning. *Eur. Polym. J.* **2018**, *99*, 27–37.

20. Rößler, F.; Kunze, T.; Lasagni, A.F. Fabrication of diffraction based security elements using direct laser interference patterning. *Opt. Express* **2017**, *25*, 22959–22970.

21. Hauschwitz, P.; Jagdheesh, R.; Alamri, S.; Rostohar, D.; Kunze, T.; Brajer, J.; Kopecek, J.; Mocek, T. Fabrication of functional superhydrophobic surfaces on carbon fibre reinforced plastics by IR and UV direct laser interference patterning. *Appl. Surf. Sci.* **2019**, *508*. 144817.

22. Alamri, S.; Lasagni, A.F. Development of a general model for direct laser interference patterning of polymers. *Opt. Express* **2017**, *25*, 9603–9616.

23. Maznev, A.A.; Crimmins, T.F.; Nelson, K.A. How to make femtosecond pulses overlap. *Opt. Lett.* **1998**, *23*, 1378–1380.

24. Furlan, V.; Biondi, M.; Demir, A.G.; Previtali, B.; Pariani, G.; Bianco, A. Two-beam interference patterning of biodegradable magnesium alloy: Influence of number of passes and spots overlap. *J. Vac. Sci. Technol. B Nanotechnol. Microelectron. Mater. Process. Meas. Phenom.* **2018**, *36*, 01A102.

25. Hecht, E. Optics (Addision Wesley, San Francisco). *Chap* **2002**, *10*, 500.

26. Malý, P. *Optika*; Karolinum: Prague, Czech Republic, 2013; ISBN 8024622467.

27. Zuhlke, C.A.; Anderson, T.P.; Alexander, D.R. Formation of multiscale surface structures on nickel via above surface growth and below surface growth mechanisms using femtosecond laser pulses. *Opt. Express* **2013**, *21*, 8460–8473.

28. Bonse, J.; Krüger, J.; Höhm, S.; Rosenfeld, A. Femtosecond laser-induced periodic surface structures. *J. Laser Appl.* **2012**, *24*, 042006.

29. Jagdheesh, R.; Diaz, M.; Marimuthu, S.; Ocana, J.L. Robust fabrication of μ-patterns with tunable and durable wetting properties: hydrophilic to ultrahydrophobic via a vacuum process. *J. Mater. Chem. A* **2017**, *5*, 7125–7136.

30. Cassie AB, D.; Baxter, S. Wettability of porous surfaces. *Trans. Faraday Soc.* **1944**, *40*, 546–551.

5.6 Journal letter F. Micromachining of invar with 784 beams using 1.3 ps laser source at 515 nm

This journal paper is aimed to establish a novel cost-efficient technology of multi-beam micromachining of invar capable to produce microstructures in a cost-efficient way by parallel microdrilling and microcutting with several hundred beamlets at the same time. DOE beamsplitting approach was investigated over well-established interference approach due to requirements of the exact number of beamlets, perfect pattern homogeneity and a combination with galvo scanner.

Author contribution

In work related to the production of this journal paper, P. Hauschwitz designed and build multi-beam processing setup, incorporating optical module from company Meopta, galvo scanning head and positioning system. He executed all laser processing experiments, drafted the manuscript with scientific interpretation with the help of co-authors. He holds the major contribution as primary and corresponding author responsible for communication and convincing the reviewers and editors for the successful publication of the article. Detail authors individual contributions are listed in table 6.

Term	Authors' individual contributions
Conceptualization	B. Stoklasa, M. Písařík
Methodology	B. Stoklasa, M. Písařík, P. Hauschwitz
Validation	B. Stoklasa, M. Písařík, P. Hauschwitz, J. Brajer
Formal analysis	B. Stoklasa, J. Kuchařík
Investigation	P. Hauschwitz, B. Stoklasa, H. Turčičová, M. Písařík, J. Kuchařík
Resources	B. Stoklasa, H. Turčičová, M. Duda
Writing - Original Draft	P. Hauschwitz
Writing - Review & Editing	P. Hauschwitz, J. Kuchařík, D. Rostohar, A. Lucianetti
Visualization	P. Hauschwitz
Supervision	B. Stoklasa, J. Brajer, M. Písařík, T. Mocek
Project administration	J. Brajer, B. Stoklasa
Funding acquisition	B. Stoklasa, M. Písařík, J. Brajer, T. Mocek

Table 6: Credit author statement - Micromachining of invar with 784 beams using 1.3 ps laser source at 515 nm

materials

Micromachining of Invar with 784 Beams Using 1.3 ps Laser Source at 515 nm

Petr Hauschwitz [1,2,*] [iD], **Bohumil Stoklasa** [3], **Jiří Kuchařík** [3], **Hana Turčičová** [1], **Michael Písařík** [1], **Jan Brajer** [1], **Danijela Rostohar** [1], **Tomáš Mocek** [1], **Martin Duda** [1,2] and **Antonio Lucianetti** [1]

[1]   HiLASE Centre, Institute of Physics, Czech Academy of Sciences, Za Radnici 828, 25241 Dolni Brezany, Czech Republic; hana.turcicova@hilase.cz (H.T.); Michael.Pisarik@Hilase.cz (M.P.); jan.brajer@Hilase.cz (J.B.); danijela.rostohar@hilase.cz (D.R.); tomas.mocek@hilase.cz (T.M.); martin.duda@hilase.cz (M.D.); antonio.lucianetti@hilase.cz (A.L.)

[2]   Faculty of Nuclear Sciences and Physical Engineering, Czech Technical University in Prague, Brehova 7, 115 19 Prague, Czech Republic

[3]   Meopta-optika, s.r.o., Kabelikova 1, 750 02 Prerov, Czech Republic; bohumil.stoklasa@meopta.com (B.S.); Jiri.Kucharik@meopta.com (J.K.)

*   Correspondence: petr.hauschwitz@hilase.cz

Abstract: To fulfil the requirements for high-resolution organic light-emitting diode (OLED) displays, precise and high-quality micrometer-scale patterns have to be fabricated inside metal shadow masks. Invar has been selected for this application due to its unique properties, especially a low coefficient of thermal expansion. In this study, a novel cost-efficient method of multi-beam micromachining of invar will be introduced. The combination of a Meopta beam splitting, focusing and monitoring module with a galvanometer scanner and HiLASE high-energy pulse laser system emitting ultrashort pulses at 515 nm allows drilling and cutting of invar foil with 784 beams at once with high precision and almost no thermal effects and heat-affected zone, thus significantly improving the throughput and efficiency.

Keywords: multi-beam micromachining; beam splitting; invar; shadow masks; OLED

---

1. Introduction

Invar is a Fe–Ni class alloy with unique properties such as excellent strength, impact toughness, processability and a low coefficient of thermal expansion [1]. Those properties are making invar very attractive for various industrial applications including bi-metal applications, storage tanks of liquified natural gas, and shadow masks for production of organic light-emitting diodes (OLED) [2]. High-resolution shadow masks are crucial in red, green and blue evaporation process of organic luminous materials during the production of OLED displays [3]. The geometry, size and overall quality of holes in shadow mask are directly connected with OLED pixel quality [4]. Chemical etching is nowadays a common microfabrication method for production of OLED shadow mask [2]. However, it is a complicated multi-step process generally composed of coating, cleaning, exposure and an etching process with no control over the taper angle. Moreover, it is difficult to fabricate a pattern smaller than the material thickness due to isotropic manner of chemical etching and thus reach the high resolution required for future virtual reality displays [5,6].

As an alternative, laser micromachining provides high-quality, single-step and environmentally friendly approach without the use of chemicals. Laser microfabrication of shadow masks was investigated with several laser systems demonstrating 85 μm channels fabricated in polymethyl methacrylate with a CO_2 laser [7], 250 μm wide channels in wax using a CO_2 laser [8], 250 μm wide

lines in plastics and glass with the use of a Nd:YAG laser at the fundamental wavelength of 1064 nm [9], or 140 μm lines fabricated in a steel shadow mask using the third harmonics of a Nd:YAG laser [10]. However, to produce high-resolution shadow masks with small features in a range of a few tens of microns, ultrashort pulsed lasers have to be deployed [8,11–13]. Invar drilling with ultrashort laser systems was investigated, demonstrating 200 μm diameter in invar utilizing a 785 nm Ti:shappire laser [4] and hole dimensions below 30 μm with excellent quality and minimal heat-affected zone [6].

However, the main drawback of ultrashort pulse laser micromachining is the processing speed which limits the widespread use in industry, especially in the case of a common single-beam direct laser writing approach. Moreover, with the emerging high-power ultrashort laser systems [14], high-quality invar micromachining becomes very inefficient as most of the laser power cannot be used. This is due to the necessity of processing close to the damage threshold to maintain high quality and minimal heat affected zone. Therefore, new techniques for rapid large-scale processing are required. The most promising rapid large-scale techniques include polygonal scanning systems [15,16], direct laser interference patterning [17,18] and multi-beam scanning approaches [19].

Beam splitting using a diffractive optical element (DOE) in a combination with galvanometer scanner and high-power ultrashort laser systems is a promising way to meet industry standards in high speed processing of large areas. DOE beam-splitter distributes the incident laser beam intensity into the desired far-field pattern which is usually an 1D or 2D array of beams. Each beam has the same characteristics as the original beam, except for pulse energy and angle of propagation [20]. Multibeam systems providing high throughputs due to beam splitting into 10–100 beamlets have recently become commercially available on the market able to drill holes in the range of 20 μm in diameter into 20 μm thick metal foils [21,22].

Consequently, this study aims to demonstrate a technology capable of producing microstructures in a cost-efficient way by introducing a prototype of a Meopta beam splitting, focusing and monitoring module. The module divides an initial high-quality beam into more than 700 beamlets for parallel processing of a thin invar foil. By utilizing the module in a combination with HiLASE high-energy pulse ultrashort laser system and a galvanometer scanner, it was possible to freely adjust the dimensions and geometry of produced microholes suitable for the production of OLED displays.

2. Materials and Methods

Invar (FeNi36) foils provided by Goodfellow GmbH (Friedberg, Germany) with a thickness of 20 μm and dimensions of 50 × 50 mm were used as received (Ra~0.07 μm). The foils were treated by Perla laser system from HiLASE (Dolni Brezany, Czech Republic), equipped with second harmonic generation module emitting at wavelength of 515 nm, with pulse duration of 1.3 ps, beam quality factor M^2 better than 1.5, repetition rate of 1 kHz and pulse energy up to 10 mJ [14,23]. The generated beam (Figure 1c) was guided through the galvanometer scanner without F-theta lens into the optical module developed by Meopta-optika, s.r.o., consisting of a DOE beamsplitter, 100 mm focusing lens and a polarizing beamsplitter for pattern observation on the sample surface. The module is responsible for focusing and splitting the initial beam by means of diffractive optics into a matrix of 28 × 28 beamlets with homogeneous distribution across the whole pattern and suppression of zero order diffraction. The module allows the separation distance between beamlets to be adjusted by changing the distance between the DOE and focusing lens. Beam splitter and camera allows to monitor the intensity, shape and focal position of each beamlet. The beamsplitter passes linearly polarized beam on to the sample surface. The reflected light from the sample with random polarization is then able to reach the camera. The separation distance between each beamlet on the sample plane was 150 μm. The sample was placed vertically on to the vacuum holder with an optional connection to the cooling water circuit. The whole setup is depicted in Figure 1.
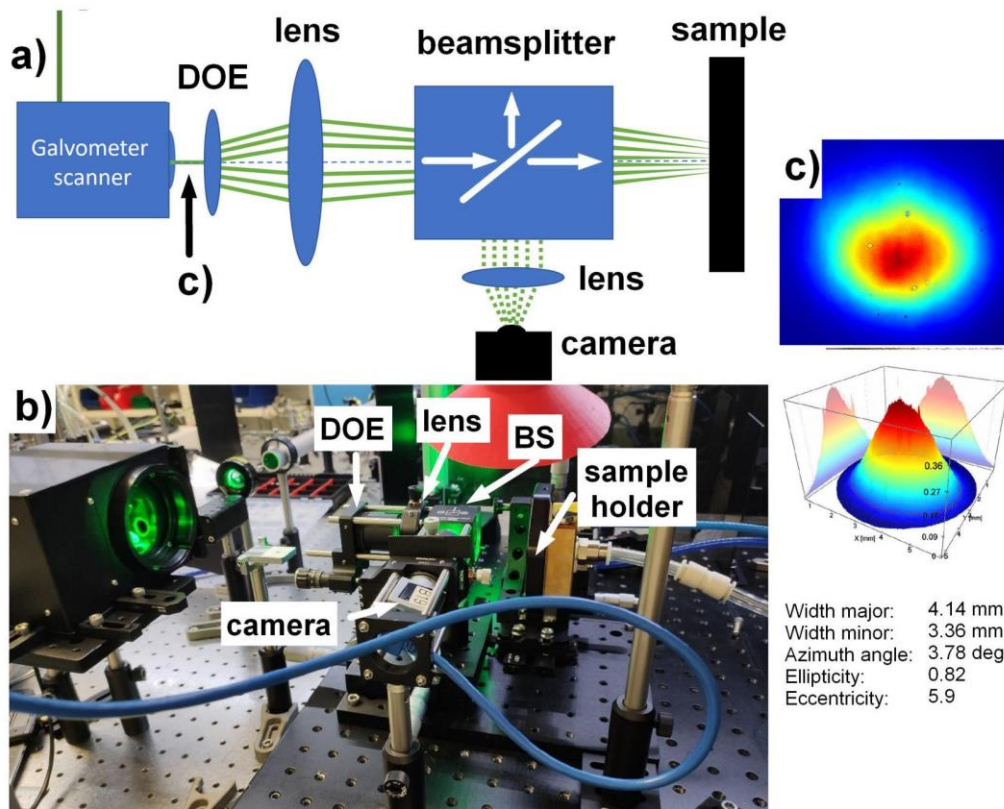
Figure 1. Schematics (**a**) and photo (**b**) of the experimental setup with a detail of input beam (**c**).

Topography of selected surfaces was analyzed with a laser scanning confocal microscope Olympus OLS 5000. The pattern shape and beamlets intensity distribution were captured by a Basler ace acA4024-29um camera with pixel size of 1.85 μm.

3. Results and Discussion

The impact of the experimental setup misalignments on the resulting multi-spot pattern homogeneity, the tolerance of deviation angles during beam deflections affecting the pattern shape, as well as the laser and processing parameters for high-quality cutting and drilling have been studied in a set of experiments.

First, the pattern homogeneity had to be adjusted to reach the same intensity in each beamlet by tilting the beam-splitting element. The pattern shape was observed in real-time on a camera inside the Meopta beam-splitting module during the alignment, as depicted in Figure 2.

As shown in Figure 2, the pattern shape reflected from the sample surface exhibits undesired speckles, which can be further improved by mirror polishing of the sample. In addition to pattern homogeneity, the working plane was easily found by observing the pattern on camera as the sharp beam profile of each beamlet (inset of Figure 2b) can be observed only when the sample is located exactly in the focal plane.
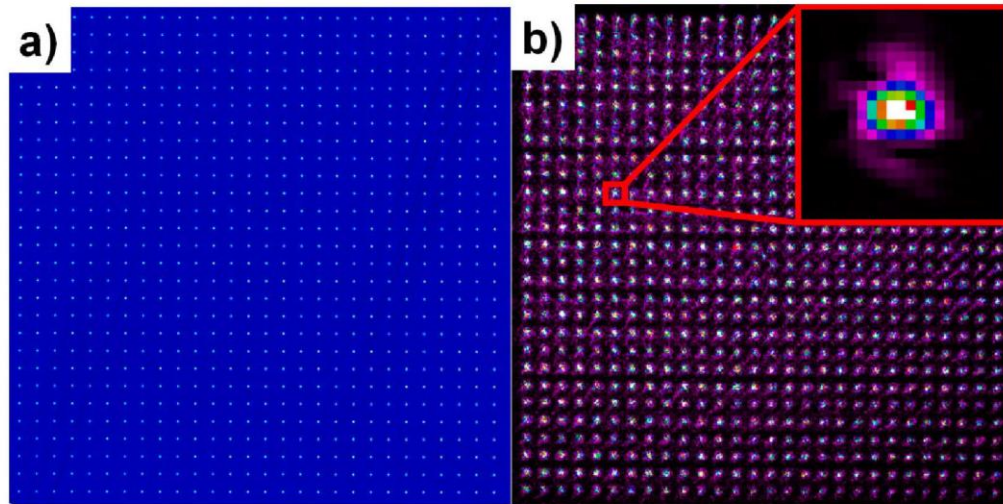
Figure 2. Final pattern shape on camera in a sample plane (**a**) and the same pattern reflected from the sample surface (**b**).

In the next step, the sample was irradiated with 100,000 consecutive laser pulses with energy of 0.6 mJ which corresponds to the fluence of 0.28 J/cm^2 for each beamlet. The first experiments revealed extensive heat accumulation connected with a large heat-affected zone and interconnection of microholes into one hole in the center of the pattern due to extensive heating and melting (Figure 3a). Consequently, the samples were placed on a water-cooled holder to minimize the effect of heat accumulation, as depicted in Figure 3b.
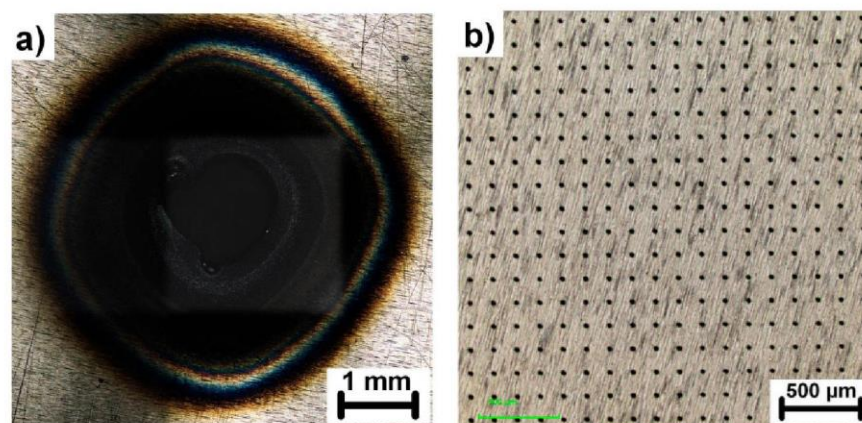

Figure 3. Overview of the heat affected zone on the sample processed without water-cooled holder (**a**) compared to the sample processed with the water-cooled holder (**b**). Both samples were processed with the same fluence of 0.28 J/cm^2 and 100,000 pulses.

To determine an optimal processing window for high-quality multi-beam drilling, different combinations of laser parameters were analyzed. First, the ablation threshold for the simultaneous drilling of 784 holes was estimated. Figure 4a presents a microhole ablated close to the ablation threshold with 100,000 pulses and pulse energy of 0.3 mJ in the initial beam (beamlet fluence of 0.15 J/cm^2). No ablation was observed for pulse energies below 0.3 mJ, hence it is considered as the ablation threshold.
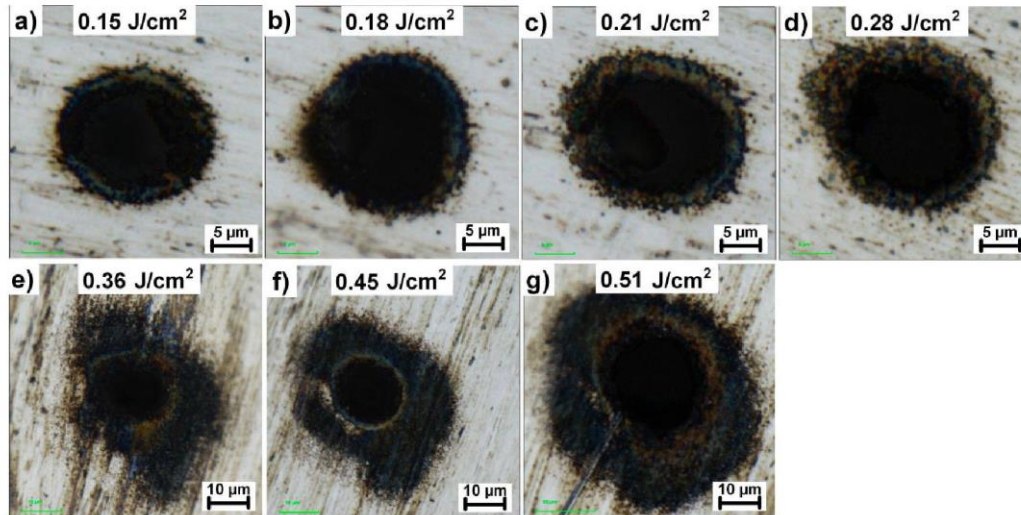
Figure 4. Evolution of microhole quality and heat affected zone with the increase in fluence. Sample is irradiated with 100,000 consecutive laser pulses. (**a–d**) gentle ablation regime, (**e–g**) high fluence regime.

The extension of the heat-affected zone and overall hole quality have been examined using different pulse energies in the range of 0.3 mJ to 1.2 mJ which correspond to the beamlet fluence of 0.15 J/cm^2 to 0.51 J/cm^2, as shown in Figure 4.

In line with the results presented in Figure 4, two ablation regimes have been identified. The highest quality microholes have been reached in a gentle ablation regime for fluences up to two-times the ablation threshold, i.e., up to 0.28 J/cm^2. In this case, the extension of the heat-affected zone was found to be less than 3 μm. By increasing the fluence over this value, the quality of microholes significantly deteriorated due to the extensive heat-affected zone. Moreover, as shown in Figure 5a, the removal rate (ablated volume per time and power) for microholes drilled in a higher fluence regime over 0.28 J/cm^2 is much smaller compared to lower fluences.

This phenomenon may be explained by the decrease in beam quality connected with high pulse energies which may overcome the tolerances of a diffractive beamsplitter and thus affect the intensity distribution within the beamlet. This issue will be further addressed in the following research.

On the other hand, the removal rate is sharply increasing with the fluence in the gentle ablation regime reaching the peak around 0.28 J/cm^2, which was identified as the optimal fluence for effective drilling.

Furthermore, the number of pulses required for piercing the sample have been determined (Figure 5b). With the threshold fluence of 0.15 J/cm^2 at least 2.5 million pulses were required to pierce through the 20 μm thick invar foil, thus removing less than 0.01 nm per pulse. By increasing the fluence above the ablation threshold, the sample was pierced with less than 700,000 pulses for fluences between 0.18 J/cm^2 and 0.28 J/cm^2. The lowest number of pulses required for piercing the foil was in the case of 0.28 J/cm^2 with only 500,000 pulses, which is in accordance with the optimal removal rate value. For the higher fluence regime, the sample was pierced only in the case of 0.36 J/cm^2 after exposition with 1 million pulses. Higher fluences did not lead to cutting through the invar foil even after 3 million pulses. Therefore, the optimal processing window for effective micromachining of invar foil has been identified as 0.18 J/cm^2 to 0.28 J/cm^2.

Additionally, the effect of laser parameters on the microhole diameter input/output aspect ratio have been studied. As demonstrated in Figure 5c, the aspect ratio decreases with higher fluences as well as with increasing number of pulses. Similarly, the shape of the exit diameter also improves with a higher number of applied pulses (Figure 6).
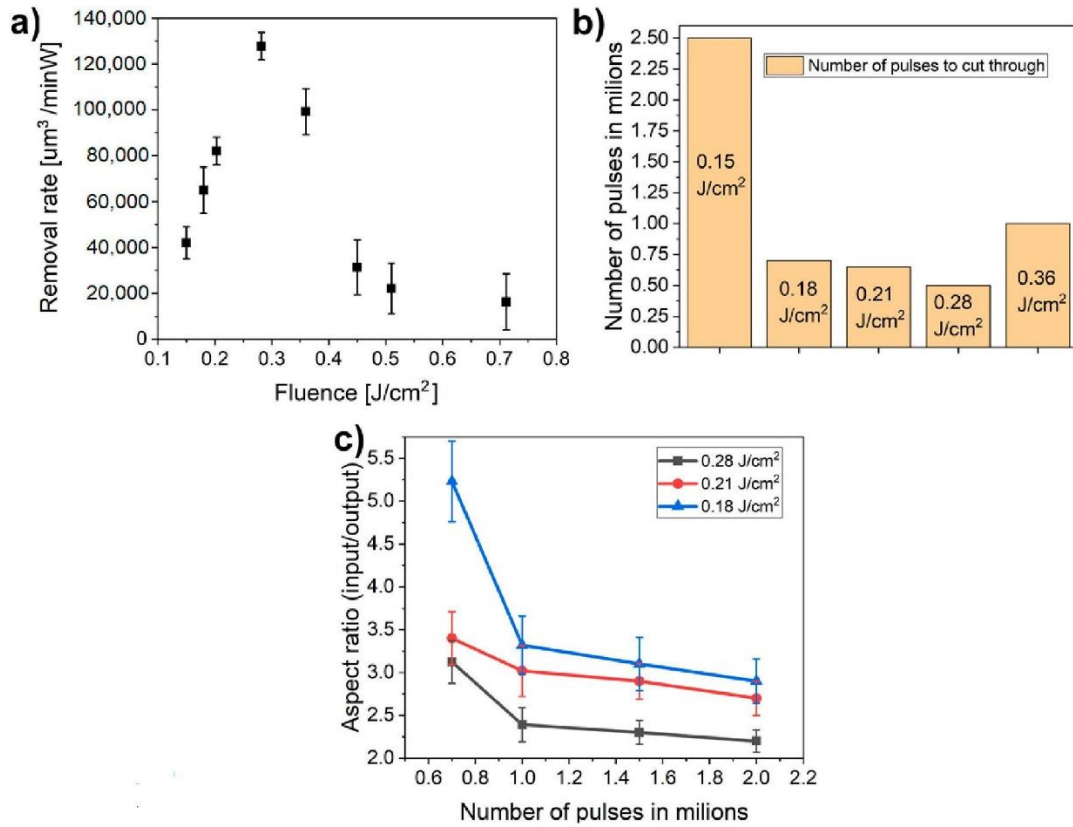
Figure 5. (**a**) Removal rate as a function of fluence; (**b**) Number of pulses necessary to cut through the whole sample; (**c**) Evolution of the aspect ratio as a function of number of pulses.
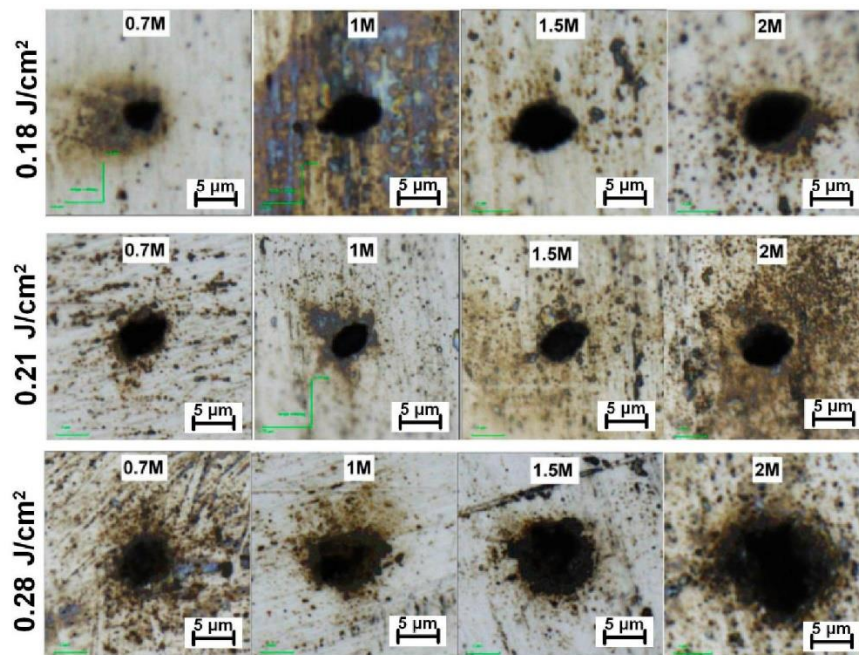

Figure 6. Geometry evolution of exit hole diameters with increasing number of pulses from 0.7 million to 2 million pulses.

Generally, the exit microhole diameter is larger and less elliptical for higher fluences and pulse counts, as demonstrated in Figure 6. The best aspect ratio and circularity were reached for the sample irradiated with 2 million pulses and 0.28 J/cm² per beamlet.

Following up on the optimal parameters, a galvanometer scanner was deployed to deflect the beam in a small area between microholes to fabricate different geometries on the invar foil. Since the separation distance between produced microholes is 150 µm, the square with a side width of 100 µm was chosen for the cutting experiment. To improve cutting efficiency, the input cut width was increased by cutting 15 squares with the same center position and decreasing diameter per 3 µm for each square. The cutting speed was adjusted to 1 mm/s to ensure high enough overlapping of ~95% with the laser repetition rate of 1 kHz. The cutting results are depicted in Figure 7.
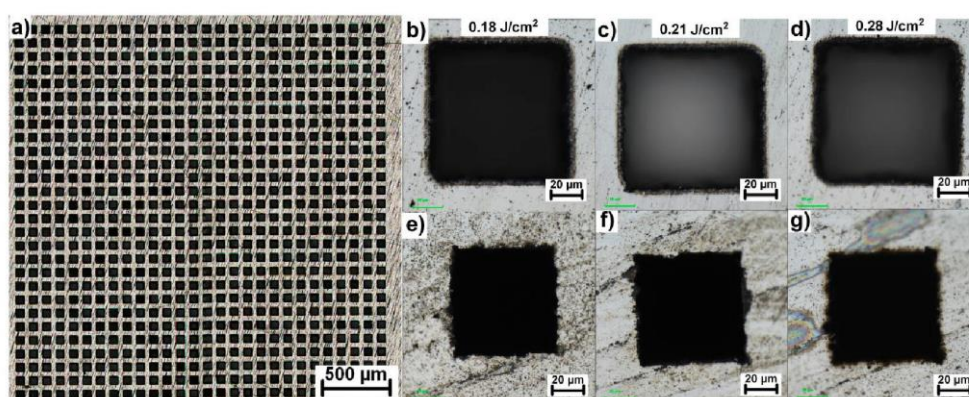

Figure 7. (**a**) Overview of a pattern cut with a combination of 28 × 28 beamsplitter and galvanometer scanner; (**b**–**d**) details of a square cuts fabricated with different fluences inside the optimal processing window and 400 overscans and their corresponding exit sides (**e**–**g**).

As demonstrated in Figure 7, it was possible to fabricate square geometries and cut through the invar foil with all 784 beams at once. The complete penetration was reached for 700, 440 and 250 overscans for the fluences of 0.18 J/cm², 0.21 J/cm², and 0.28 J/cm², respectively. In addition, the consistency of square shape and their separation distance was measured on 20 randomly selected squares across the pattern confirming the exact same parameters across the pattern with the standard deviation smaller than 3 µm in all cases.

4. Conclusions

Utilization of a Meopta beam-splitting, focusing and monitoring module in a combination with HiLASE high-energy pulse laser system emitting ultrashort pulses at 515 nm resulted in efficient cutting and drilling of invar foil simultaneously by 784 beamlets, arranged in a matrix of 28 × 28 beamlets. The features of optical module allow the setup to be aligned quickly to reach homogeneous intensity distribution across the whole pattern, as well as focus adjustment. By determining the ablation threshold, optimal fluence levels and pulse counts, the optimal processing window for effective high-quality drilling and cutting with heat affected zone below 3 µm has been identified as 0.18 J/cm² to 0.28 J/cm². The combination of galvanometer scanning head and beam-splitting module enabled multi-beam fabrication of square-shaped microholes with adjustable dimensions. With the use of this solution, the throughput can be increased 7 times compared to the state of the art commercial multi-beam systems and more than 700 times compared to the single beam approach, thus showing high potential for significant improvement in the fabrication speed and efficiency during the production of invar shadow masks.

Author Contributions: Conceptualization, B.S., M.P.; Methodology, B.S., M.P., P.H.; Validation, B.S., M.P., P.H., J.B.; Formal analysis, B.S., J.K.; Investigation, P.H., B.S., H.T., J.K.; Resources, B.S., H.T., M.D.; Writing-Original

References

1. Ono, F.; Hamatani, Y.; Mukumoto, Y.; Komatsu, S.; Ishikawa, N.; Chimi, Y.; Iwase, A.; Kambara, T.; Mueller, C.; Neumann, R. Modification of Fe–Ni Invar alloys by high-energy ion beams. *Nucl. Instrum. Methods Phys. Res. Sect. B Beam Interac. Mater. At.* **2003**, *206*, 295–298. [CrossRef]

2. Kim, C. Production of shadow-mask-improved technology. *J. Mater. Process. Technol.* **2002**, *127*, 409–418. [CrossRef]

3. Shin, H.Y.; Suh, M.C. A study on full color organic light emitting diodes with blue common layer under the patterned emission layer. *Org. Electron.* **2014**, *15*, 2932–2941. [CrossRef]

4. Chung, I.-Y.; Kim, J.-D.; Kang, K.-H. Ablation drilling of invar alloy using ultrashort pulsed laser. *Int. J. Precis. Eng. Manuf.* **2009**, *10*, 11–16. [CrossRef]

5. Kim, S.H.; Choi, S.G.; Choi, W.K.; Yang, B.Y.; Lee, E.S. Pulse electrochemical machining on Invar alloy: Optical microscopic/SEM and non-contact 3D measurement study of surface analyses. *Appl. Surf. Sci.* **2014**, *314*, 822–831. [CrossRef]

6. Choi, W.; Kim, H.Y.; Jeon, J.W.; Chang, W.S.; Cho, S.H. Vibration-assisted femtosecond Laser drilling with controllable taper angles for AMOLED fine metal mask fabrication. *Materials* **2017**, *10*, 212. [CrossRef]

7. Klank, H.; Kutter, J.P.; Geschke, O. CO_2-laser micromachining and back-end processing for rapid production of PMMA-based microfluidic systems. *Lab Chip* **2002**, *2*, 242–246. [CrossRef]

8. Fan, Y.; Li, H.; Yi, Y.; Foulds, I.G. Laser micromachined wax-covered plastic paper as both sputter deposition shadow masks and deep-ultraviolet patterning masks for polymethylmethacrylate-based microfluidic systems. *J. Micro/Nanolithogr. MEMS MOEMS* **2013**, *12*, 049701. [CrossRef]

9. Tahir, B.A.; Ahmed, R.; Ashiq, M.G.; Ahmed, A.; Saeed, M.A. Cutting of nonmetallic materials using Nd: YAG laser beam. *Chin. Phys. B* **2012**, *21*, 044201. [CrossRef]

10. Shiu, P.; Knopf, G.; Ostojic, M.; Nikumb, S. Rapid fabrication of tooling for microfluidic devices via laser micromachining and hot embossing. *J. Micromech. Microeng.* **2008**, *18*, 025012. [CrossRef]

11. Rizvi, N.H.; Apte, P. Developments in laser micro-machining techniques. *J. Mater. Process. Technol.* **2002**, *127*, 206–210. [CrossRef]

12. Kumar, A.; Gupta, A.; Kant, R.; Akhtar, S.N.; Tiwari, N.; Ramkumar, J.; Bhattacharya, S. Optimization of laser machining process for the preparation of photomasks, and its application to microsystems fabrication. *J. Micro/Nanolithogr. MEMS MOEMS* **2013**, *12*, 041203. [CrossRef]

13. Heo, J.; Min, H.; Lee, M. Laser micromachining of permalloy for fine metal mask. *Int. J. Precis. Eng. Manuf. Green Technol.* **2015**, *2*, 225–230. [CrossRef]

14. Smrž, M.; Novák, O.; Mužík, J.; Turčičová, H.; Chyla, M.; Nagisetty, S.S.; Vyvlečka, M.; Roškot, L.; Miura, T.; Černohorská, J.; et al. Advances in high-power, ultrashort pulse DPSSL technologies at HiLASE. *Appl. Sci.* **2017**, *7*, 1016. [CrossRef]

15. Mincuzzi, G.; Gemini, L.; Faucon, M.; Kling, R. Extending ultra-short pulse laser texturing over large area. *Appl. Surf. Sci.* **2016**, *386*, 65–71. [CrossRef]

16. De Loor, R. Polygon scanner system for ultra short pulsed laser micro-machining applications. *Phys. Proced.* **2013**, *41*, 544–551. [CrossRef]

17. Voisiat, B.; Gedvilas, M.; Indrišiūnas, S.; Račiukaitis, G. Picosecond-laser 4-beam-interference ablation as a flexible tool for thin film microstructuring. *Phys. Proced.* **2011**, *12*, 116–124. [CrossRef]

18. Hauschwitz, P.; Jagdheesh, R.; Alamri, S.; Rostohar, D.; Kunze, T.; Brajer, J.; Kopeček, J.; Mocek, T. Fabrication of functional superhydrophobic surfaces on carbon fibre reinforced plastics by IR and UV direct laser interference patterning. *Appl. Surf. Sci.* **2019**, *508*, 144817. [CrossRef]

19. Gillner, A.; Finger, J.; Gretzki, P.; Niessen, M.; Bartels, T.; Reininghaus, M. High power laser processing with ultrafast and multi-parallel beams. *J. Laser Micro Nanoeng.* **2019**, *14*, 129–137.

20. Katz, S.; Kaplan, N.; Grossinger, I. Using Diffractive Optical Elements: DOEs for beam shaping–fundamentals and applications. *Opt. Photonik* **2018**, *13*, 83–86. [CrossRef]

21. Holtkamp, J.; Eifel, S.; Ryll, J. Material Processing with Ultrashort-pulsed Lasers: Potentials—Requirements—Approaches. *Laser Tech. J.* **2014**, *11*, 36–39. [CrossRef]

22. Holtkamp, J. Pulsar Photonics: Innovative Beam Forming Concepts, Swissphotonics. Available online: https://swissphotonics.net/libraries.files/holtkamp (accessed on 1 July 2020).

23. Duda, M.; Novák, O.; Chyla, M.; Smrž, M.; Mocek, T. Balancing the conversion efficiency and beam quality of second harmonic generation of a two-picosecond Yb: YAG thin-disk laser. *Laser Phys.* **2020**, *30*, 025405. [CrossRef]

6 Conclusion

Surface functionalities can be tuned by suitable microstructure geometry and impose new properties like superhydrophobicity, anti-ice or anti-bacteria to common materials. Laser is a suitable tool to fabricate such microstructures on a large variety of materials ranging from metals to dielectrics and composite materials. Several laser and processing parameters have to be optimized for high-quality micro and nanostructure fabrication. The complexity of parameter combinations increases when state-of-the-art high-power laser systems are applied. To fully use the potential of these systems for the close-to-threshold fabrication of micro and nanostructures, new ultrafast scanning or multi-beam approaches have to be applied. The most promising approaches are polygon scanning systems, DOE based scanning systems, direct laser interference processing and programable SLM holographic processing coupled with galvo scanner. All approaches have their advantages and limitations depending on the final application and the laser source. Optimal solution for rapid-large scale micromachining laboratory may be a combination of two systems: SLM head combined with galvo scanner to develop optimal diffraction pattern and process parameters. Consequently, according to that final parameters, DOE can be manufactured while providing much higher LIDT to be able to efficiently use a high-power laser source. High-energy pulsed laser systems can also benefit from interference processing, which is a less expensive and more compact solution, easily scalable to structure large area in resolutions below the diffraction limit of common lenses while fully utilizing available pulse energy.

In the experimental section, methods for micro and nanofabrication of functional superhydrophobic structures have been introduced in a form of scientific papers published in international journals. Several structure geometries suitable for superhydrophobic surface have been demonstrated with the use of picosecond and nanosecond laser sources. The novel nanostructuring technique developed by the author allows to cover microstructures with nanoscale protrusions despite using the nanosecond laser source with heat diffusion length much higher than the structure size. Consequently, the wide range of structure geometries, as well as different applied laser sources, allow users to choose appropriate parameters to fit the final application. Moreover, the novel vacuum post-processing technique improves

further the water repellency of superhydrophobic structures. It also significantly decreases the transition time of the initially hydrophilic surface to reach a superhydrophobic state from several days to a few hours.

Following the findings in the theoretical section, multi-beam approaches have been employed to overcome the limits of single beam processing and to increase the fabrication speed and efficiently utilize high-power laser sources. In line with that, the author designed and developed interference processing station and demonstrated large-beam interference patterning of functional micro and nanostructures. In addition, beam-splitting by DOE combined with galvo scanner was employed for parallel micromachining of invar. The author also supervised the tendering and installation of SLM-based dynamic beam-shaping and splitting head combined with galvo scanner to complete the key technologies for rapid large-scale functionalization discussed in the theoretical section.

In conclusion, the author significantly increased his knowledge and expertise in the field of rapid large-scale surface functionalization and micromachining, gained abundant experiences, and published his results in numerous international peer-reviewed journals.

6.1 Contribution to the scientific community

The results achieved in this doctoral thesis will, according to the author's opinion, contribute to the better understanding and faster development of rapid large-scale surface functionalization and micromachining for various scientific and industrial applications.

The main outstanding results can be summarized as follows:

- Development of a wide range of micro and nanostructures for superhydrophobic surfaces fabricated by picosecond and nanosecond laser sources

- A novel technique for surface nanostructuring utilizing 3 ns fibre laser

- A new vacuum-based post-treatment method significantly reducing the transformation time of initially hydrophilic surfaces to superhydrophobic state.

- Fabrication of functional superhydrophobic microstructures on carbon fibre reinforced plastics by interference patterning for the first time in literature.

- Development of interference processing station for a novel method of large-beam interference patterning

- Novel techniques for large-scale fabrication of hierarchical structures combining interference patterning with LIPSS and nanostructuring.

- Large-scale micromachining technique with 784 beams combined with galvo scanner

Except for the scientific publications in peer-reviewed international journals, the author is also involved in the following projects:

- LM2015086 – HiLASE: New lasers for industry and research (2016-2019,MSM/LM) – supported by Ministry of Education, Youth and Sports of the Czech Republic

- CZ.02.1.01/0.0/0.0/15_006/0000674 – HiLASE Centre of Excellence (2017-2022, MSM/EF) – supported by Ministry of Education, Youth and Sports of the Czech Republic within Operational Programme Research, Development and Education

- TN01000008 NCK CEPO – New methods for laser micromachining – supported by Technology Agency of the Czech Republic within the program of National Centre of Competence

- TM01000021 Delta2 - Development of non linear absorption driven optic system and process for high throughput TGV formation – supported by Technology Agency of the Czech Republic within the program Delta 2.

Since January 2020, the author leads the Laser Micro-Machining group at HiLASE.

7 References

[1] LONG, J., P. FAN, D. GONG, D. JIANG, et al. Superhydrophobic surfaces fabricated by femtosecond laser with tunable water adhesion: from lotus leaf to rose petal. ACS applied materials & interfaces, 2015, 7(18), 9858-9865.

[2] LIU, Y. AND G. LI A new method for producing "Lotus Effect" on a biomimetic shark skin. Journal of colloid and interface science, 2012, 388(1), 235-242.

[3] MALSHE, A. P., S. BAPAT, K. P. RAJURKAR AND H. HAITJEMA Bio-inspired textures for functional applications. CIRP Annals, 2018, 67(2), 627-650.

[4] KAMAL, S. A. A., R. RITIKOS AND S. A. RAHMAN Wetting behaviour of carbon nitride nanostructures grown by plasma enhanced chemical vapour deposition technique. Applied surface science, 2015, 328, 146-153.

[5] CREMALDI, J. AND B. BHUSHAN Fabrication of bioinspired, self-cleaning superliquiphilic/phobic stainless steel using different pathways. Journal of colloid and interface science, 2018, 518, 284-297.

[6] LAKSHMI, R. AND B. J. BASU Fabrication of superhydrophobic sol–gel composite films using hydrophobically modified colloidal zinc hydroxide. Journal of colloid and interface science, 2009, 339(2), 454-460.

[7] SCHRÖDER, K., A. MEYER-PLATH, D. KELLER, W. BESCH, et al. Plasma-induced surface functionalization of polymeric biomaterials in ammonia plasma. Contributions to Plasma Physics, 2001, 41(6), 562-572.

[8] TOOSI, S. F., S. MORADI, M. EBRAHIMI AND S. G. HATZIKIRIAKOS Microfabrication of polymeric surfaces with extreme wettability using hot embossing. Applied surface science, 2016, 378, 426-434.

[9] SHIU, J.-Y., C.-W. KUO, P. CHEN AND C.-Y. MOU Fabrication of tunable superhydrophobic surfaces by nanosphere lithography. Chemistry of materials, 2004, 16(4), 561-564.

[10] LIU, Y., S. LI, Y. WANG, H. WANG, et al. Superhydrophobic and superoleophobic surface by electrodeposition on magnesium alloy substrate: wettability and corrosion inhibition. Journal of colloid and interface science, 2016, 478, 164-171.

[11] VOROBYEV, A. Y. AND C. GUO Direct femtosecond laser surface nano/microstructuring and its applications. Laser & Photonics Reviews, 2013, 7(3), 385-407.

[12] LIU, K., X. YAO AND L. JIANG Recent developments in bio-inspired special wettability. Chemical Society Reviews, 2010, 39(8), 3240-3255.

[13] LIU, K. AND L. JIANG Bio-inspired design of multiscale structures for function integration. Nano Today, 2011, 6(2), 155-175.

[14] ZHANG, C., D. A. MCADAMS AND J. C. GRUNLAN Nano/micro-manufacturing of bioinspired materials: A review of methods to mimic natural structures. Advanced materials, 2016, 28(30), 6292-6321.

[15] ZAN, G. AND Q. WU Biomimetic and bioinspired synthesis of nanomaterials/nanostructures. Advanced materials, 2016, 28(11), 2099-2147.

[16] YOSHINO, F., L. SHAH, M. FERMANN, A. ARAI, et al. Micromachining with a high repetition rate femtosecond fiber laser. J. Laser Micro. Nanoeng., 2008, 3(3), 157-162.

[17] JEEVAHAN, J., M. CHANDRASEKARAN, G. B. JOSEPH, R. DURAIRAJ, et al. Superhydrophobic surfaces: a review on fundamentals, applications, and challenges. Journal of Coatings Technology and Research, 2018, 15(2), 231-250.

[18] TENJIMBAYASHI, M., M. HIGASHI, T. YAMAZAKI, I. TAKENAKA, et al. Droplet motion control on dynamically hydrophobic patterned surfaces as multifunctional liquid manipulators. ACS applied materials & interfaces, 2017, 9(12), 10371-10377.

[19] FALDE, E. J., S. T. YOHE, Y. L. COLSON AND M. W. GRINSTAFF Superhydrophobic materials for biomedical applications. Biomaterials, 2016, 104, 87-103.

[20] ZHANG, H., W. LI AND G. FANG A new model for thermodynamic analysis on wetting behavior of superhydrophobic surfaces. Applied surface science, 2012, 258(7), 2707-2716.

[21] MAKKONEN, L. Young's equation revisited. Journal of Physics: Condensed Matter, 2016, 28(13), 135001.

[22] KONG, T., G. LUO, Y. ZHAO AND Z. LIU Bioinspired Superwettability Micro/Nanoarchitectures: Fabrications and Applications. Advanced Functional Materials, 2019, 1808012.

[23] OLIVER, J., C. HUH AND S. MASON Resistance to spreading of liquids by sharp edges. Journal of colloid and interface science, 1977, 59(3), 568-581.

[24] QUÉRÉ, D. Wetting and roughness. Annu. Rev. Mater. Res., 2008, 38, 71-99.

[25] WENZEL, R. N. Resistance of solid surfaces to wetting by water. Industrial & Engineering Chemistry, 1936, 28(8), 988-994.

[26] LAFUMA, A. AND D. QUÉRÉ Superhydrophobic states. Nature materials, 2003, 2(7), 457.

[27] GAO, X., X. YAN, X. YAO, L. XU, et al. The dry-style antifogging properties of mosquito compound eyes and artificial analogues prepared by soft lithography. Advanced materials, 2007, 19(17), 2213-2217.

[28] BARTHLOTT, W. AND C. NEINHUIS Purity of the sacred lotus, or escape from contamination in biological surfaces. Planta, 1997, 202(1), 1-8.

[29] HERMINGHAUS, S. Roughness-induced non-wetting. EPL (Europhysics Letters), 2007, 79(5), 59901.

[30] AHUJA, A., J. TAYLOR, V. LIFTON, A. SIDORENKO, et al. Nanonails: A simple geometrical approach to electrically tunable superlyophobic surfaces. Langmuir, 2008, 24(1), 9-14.

[31] TUTEJA, A., W. CHOI, M. MA, J. M. MABRY, et al. Designing superoleophobic surfaces. Science, 2007, 318(5856), 1618-1622.

[32] CHEN, W., A. Y. FADEEV, M. C. HSIEH, D. ÖNER, et al. Ultrahydrophobic and ultralyophobic surfaces: some comments and examples. Langmuir, 1999, 15(10), 3395-3399.

[33] BOBJI, M. S., S. V. KUMAR, A. ASTHANA AND R. N. GOVARDHAN Underwater sustainability of the "Cassie" state of wetting. Langmuir, 2009, 25(20), 12120-12126.

[34] ALAMRI, S., A. I. AGUILAR-MORALES AND A. F. LASAGNI Controlling the wettability of polycarbonate substrates by producing hierarchical structures using direct laser interference patterning. European Polymer Journal, 2018, 99, 27-37.

[35] RARATY, L. AND D. TABOR The adhesion and strength properties of ice. Proceedings of the Royal Society of London. Series A. Mathematical and Physical Sciences, 1958, 245(1241), 184-201.

[36] SAYWARD, J. M. Seeking low ice adhesion. 1979.

[37] THOMAS, S. K., R. P. CASSONI AND C. D. MACARTHUR Aircraft anti-icing and de-icing techniques and modeling. Journal of Aircraft, 1996, 33(5), 841-854.

[38] DEL CERRO, D. A., G. RÖMER AND A. HUIS Erosion resistant anti-ice surfaces generated by ultra short laser pulses. Physics Procedia, 2010, 5, 231-235.

[39] RÖMER, G.-W., D. A. DEL CERRO, R. C. SIPKEMA, M. GROENENDIJK, et al. Ultra short pulse laser generated surface textures for anti-ice applications in aviation. In *International Congress on Applications of Lasers & Electro-Optics.* Citeseer, 2009, vol. 2009, p. 30-37.

[40] CAO, L., A. K. JONES, V. K. SIKKA, J. WU, et al. Anti-icing superhydrophobic coatings. Langmuir, 2009, 25(21), 12444-12448.

[41] WANG, F., C. LI, Y. LV, F. LV, et al. Ice accretion on superhydrophobic aluminum surfaces under low-temperature conditions. Cold regions science and technology, 2010, 62(1), 29-33.

[42] VERCILLO, V., J. T. CARDOSO, D. HUERTA-MURILLO, S. TONNICCHIA, et al. Durability of Superhydrophobic Laser-Treated Metal Surfaces under Icing Conditions. Materials Letters: X, 2019, 100021.

[43] SCHUTZIUS, T. M., S. JUNG, T. MAITRA, P. EBERLE, et al. Physics of icing and rational design of surfaces with extraordinary icephobicity. Langmuir, 2014, 31(17), 4807-4821.

[44] EBERLE, P., M. K. TIWARI, T. MAITRA AND D. POULIKAKOS Rational nanostructuring of surfaces for extraordinary icephobicity. Nanoscale, 2014, 6(9), 4874-4881.

[45] MISHCHENKO, L., B. HATTON, V. BAHADUR, J. A. TAYLOR, et al. Design of ice-free nanostructured surfaces based on repulsion of impacting water droplets. ACS nano, 2010, 4(12), 7699-7707.

[46] VERCILLO, V., S. TONNICCHIA, J. M. ROMANO, A. GARCÍA-GIRÓN, et al. Design Rules for Laser-Treated Icephobic Metallic Surfaces for Aeronautic Applications. Advanced Functional Materials, 2020, 30(16), 1910268.

[47] CAMPOCCIA, D., L. MONTANARO AND C. R. ARCIOLA The significance of infection related to orthopedic devices and issues of antibiotic resistance. Biomaterials, 2006, 27(11), 2331-2339.

[48] DONLAN, R. M. Biofilm formation: a clinically relevant microbiological process. Clinical Infectious Diseases, 2001, 33(8), 1387-1392.

[49] TROIDLE, L. AND F. FINKELSTEIN Treatment and outcome of CPD-associated peritonitis. Annals of clinical microbiology and antimicrobials, 2006, 5(1), 6.

[50] TORTORA, G. J., B. R. FUNKE, C. L. CASE AND T. R. JOHNSON *Microbiology: an introduction*. Edtion ed.: Benjamin Cummings San Francisco, CA, 2004.

[51] PARVIZI, J., E. WICKSTROM, A. R. ZEIGER, C. S. ADAMS, et al. Frank Stinchfield Award: Titanium surface with biologic activity against infection. Clinical Orthopaedics and Related Research®, 2004, 429, 33-38.

[52] MARAMBIO-JONES, C. AND E. M. HOEK A review of the antibacterial effects of silver nanomaterials and potential implications for human health and the environment. Journal of Nanoparticle Research, 2010, 12(5), 1531-1551.

[53] FADEEVA, E., V. K. TRUONG, M. STIESCH, B. N. CHICHKOV, et al. Bacterial retention on superhydrophobic titanium surfaces fabricated by femtosecond laser ablation. Langmuir, 2011, 27(6), 3012-3019.

[54] MARTINEZ, E., E. ENGEL, J. PLANELL AND J. SAMITIER Effects of artificial micro-and nano-structured surfaces on cell behaviour. Annals of Anatomy-Anatomischer Anzeiger, 2009, 191(1), 126-135.

[55] LUTEY, A. H., L. GEMINI, L. ROMOLI, G. LAZZINI, et al. Towards laser-textured antibacterial surfaces. Scientific reports, 2018, 8(1), 10112.

[56] SCARDINO, A., J. GUENTHER AND R. DE NYS Attachment point theory revisited: the fouling response to a microtextured matrix. Biofouling, 2008, 24(1), 45-53.

[57] IVANOVA, E. P., V. K. TRUONG, H. K. WEBB, V. A. BAULIN, et al. Differential attraction and repulsion of Staphylococcus aureus and Pseudomonas aeruginosa on molecularly smooth titanium films. Scientific reports, 2011, 1, 165.

[58] OLIVEIRA, S. M., N. M. ALVES AND J. F. MANO Cell interactions with superhydrophilic and superhydrophobic surfaces. Journal of Adhesion Science and Technology, 2014, 28(8-9), 843-863.

[59] ZHENG, J., L. LI, H.-K. TSAO, Y.-J. SHENG, et al. Strong repulsive forces between protein and oligo (ethylene glycol) self-assembled monolayers: a molecular simulation study. Biophysical journal, 2005, 89(1), 158-166.

[60] ROACH, P., N. J. SHIRTCLIFFE AND M. I. NEWTON Progess in superhydrophobic surface development. Soft Matter, 2008, 4(2), 224-240.

[61] CHEN, B., J. QIU, E. SAKAI, N. KANAZAWA, et al. Robust and superhydrophobic surface modification by a "Paint+ Adhesive" method: applications in self-cleaning after oil contamination and oil–water separation. ACS applied materials & interfaces, 2016, 8(27), 17659-17667.

[62] MAHADIK, S. A., R. S. VHATKARA, D. B. MAHADIK, M. S. KAVALE, et al. Superhydrophobic silica coating by dip coating method. Applied surface science, 2013, 277, 67-72.

[63] CHENG, Q., C. HUANG AND A. P. TOMSIA Freeze casting for assembling bioinspired structural materials. Advanced materials, 2017, 29(45), 1703155.

[64] SHAO, D. AND S. CHEN Surface-plasmon-assisted nanoscale photolithography by polarized light. Applied Physics Letters, 2005, 86(25), 253107.

[65] LIU, T. AND C.-J. KIM Turning a surface superrepellent even to completely wetting liquids 2014.

[66] ROMOLI, L., F. FISCHER AND R. KLING A study on UV laser drilling of PEEK reinforced with carbon fibers. Optics and lasers in Engineering, 2012, 50(3), 449-457.

[67] BÜCHTER, E. "Cleaning with Light" Laser beam surface treatment opens up a wide range of industrial applications thanks to state-of-the-art laser technology. Laser Technik Journal, 2018, 15(2), 36-39.

[68] DUNN, M. H. AND M. EBRAHIMZADEH Parametric generation of tunable light from continuous-wave to femtosecond pulses. Science, 1999, 286(5444), 1513-1517.

[69] GAMALY, E. G. The physics of ultra-short laser interaction with solids at non-relativistic intensities. Physics Reports, 2011, 508(4-5), 91-243.

[70] ARNOLD, D. AND E. CARTIER Theory of laser-induced free-electron heating and impact ionization in wide-band-gap solids. Physical review B, 1992, 46(23), 15102.

[71] GAMALY, E. G. *Femtosecond Laser-Matter Interaction: Theory, Experiments and Applications*. Edtion ed.: CRC Press, 2011. ISBN 9814267805.

[72] TEMNOV, V., K. SOKOLOWSKI-TINTEN, P. ZHOU, A. EL-KHAMHAWY, et al. Multiphoton ionization in dielectrics: comparison of circular and linear polarization. Physical review letters, 2006, 97(23), 237403.

[73] KELDYSH, L. Ionization in the field of a strong electromagnetic wave. Sov. Phys. JETP, 1965, 20(5), 1307-1314.

[74] HOLWAY JR, L. H. AND D. FRADIN Electron avalanche breakdown by laser radiation in insulating crystals. Journal of Applied Physics, 1975, 46(1), 279-291.

[75] GRUZDEV, V. E. Laser-induced collective ionization in wide band-gap crystalline dielectrics. Ultrafast Phenomena and Physics of Superintense Laser Fields; Quantum and Atom Optics; Engineering of Quantum Information, Proc. SPIE Vol, 2006, 6256, 625602.

[76] KRÜGER, J., M. LENZNER, S. MARTIN, M. LENNER, et al. Single-and multi-pulse femtosecond laser ablation of optical filter materials. Applied surface science, 2003, 208, 233-237.

[77] KRÜGER, J. AND W. KAUTEK Ultrashort pulse laser interaction with dielectrics and polymers. polymers and light, 2004, 247-290.

[78] HAUSCHWITZ, P. Laserové mikrotexturování povrchu kovů. 2016. Bachelor thesis.

[79] MANKE II, G. C. Ultrashort pulsed laser technology development program. In *Technologies for Optical Countermeasures XI; and High-Power Lasers 2014: Technology and Systems.* International Society for Optics and Photonics, 2014, vol. 9251, p. 92510O.

[80] STOIAN, R., A. ROSENFELD, D. ASHKENASI, I. HERTEL, et al. Surface charging and impulsive ion ejection during ultrashort pulsed laser ablation. Physical review letters, 2002, 88(9), 097603.

[81] SCHLESSINGER, L. AND J. WRIGHT Inverse-bremsstrahlung absorption rate in an intense laser field. Physical Review A, 1979, 20(5), 1934.

[82] VON DER LINDE, D., K. SOKOLOWSKI-TINTEN AND J. BIALKOWSKI Laser–solid interaction in the femtosecond time regime. Applied surface science, 1997, 109, 1-10.

[83] AGUILAR-MORALES, A. I., S. ALAMRI AND A. F. LASAGNI Micro-fabrication of high aspect ratio periodic structures on stainless steel by picosecond direct laser interference patterning. Journal of materials processing technology, 2018, 252, 313-321.

[84] SCHILLE, J., R. EBERT, U. LOESCHNER, P. REGENFUSS, et al. Micro structuring with highly repetitive ultra short laser pulses. In *Proc. 9th Int'l Symp. Laser Prec. Microfab.(LMP2008).* 2008, p. 08-57.

[85] LAHAYE, N. L., S. S. HARILAL, P. K. DIWAKAR AND A. HASSANEIN The effect of laser pulse duration on ICP-MS signal intensity, elemental fractionation, and detection limits in fs-LA-ICP-MS. Journal of Analytical Atomic Spectrometry, 2013, 28(11), 1781-1787.

[86] ROBERTS, S. Canadian metalworking. (2016). The Quickening Pulse of Laser Machining. [online] Available at: http://www.canadianmetalworking.com [Accessed 25 Apr. 2018].

[87] WEBER, R., T. GRAF, P. BERGER, V. ONUSEIT, et al. Heat accumulation during pulsed laser materials processing. Optics express, 2014, 22(9), 11312-11324.

[88] RUNG, S., J. BARTH AND R. HELLMANN Characterization of laser beam shaping optics based on their ablation geometry of thin films. Micromachines, 2014, 5(4), 943-953.

[89] LOPEZ, J., K. MISHCHIK, B. CHASSAGNE, C. JAVAUX-LEGER, et al. Glass cutting using ultrashort pulsed Bessel beams. In *International Congress on Applications of Lasers & Electro-Optics.* LIA, 2015, vol. 2015, p. 60-69.

[90] DE LOOR, R. Polygon scanner system for ultra short pulsed laser micro-machining applications. Physics Procedia, 2013, 41, 544-551.

[91] JAEGGI, B., B. NEUENSCHWANDER, U. HUNZIKER, J. ZUERCHER, et al. Ultra-high-precision surface structuring by synchronizing a galvo scanner with an ultra-short-pulsed laser system in MOPA arrangement. In *Laser Applications in Microelectronic and Optoelectronic Manufacturing (LAMOM) XVII.* International Society for Optics and Photonics, 2012, vol. 8243, p. 82430K.

[92] THORLABS, I. F-Theta Lenses Tutorial
https://www.thorlabs.com/newgrouppage9.cfm?objectgroup_id=10766. PDF (Accessed: 29.10.2019).

[93] VAN DER STRAETEN, K., O. NOTTRODT, M. ZURIC, A. OLOWINSKY, et al. Polygon scanning system for high-power, high-speed microstructuring. Procedia CIRP, 2018, 74, 491-494.

[94] DEL CERRO, D. A., G. RÖMER AND A. H. IN'T VELD. Picosecond laser machined designed patterns with anti-ice effect. In *Proceedings of the 11th International Symposium on Laser Precision Microfabrication, LPM2010, Stuttgart, Germany, June 7-10, 2010.* 2010.

[95] WU, B., M. ZHOU, J. LI, X. YE, et al. Superhydrophobic surfaces fabricated by microstructuring of stainless steel using a femtosecond laser. Applied surface science, 2009, 256(1), 61-66.

[96] SMRŽ, M., O. NOVÁK, J. MUŽÍK, H. TURČIČOVÁ, et al. Advances in high-power, ultrashort pulse DPSSL technologies at HiLASE. Applied Sciences, 2017, 7(10), 1016.

[97] LIU, X., D. DU AND G. MOUROU Laser ablation and micromachining with ultrashort laser pulses. IEEE journal of quantum electronics, 1997, 33(10), 1706-1716.

[98] MINCUZZI, G., L. GEMINI, M. FAUCON AND R. KLING Extending ultra-short pulse laser texturing over large area. Applied surface science, 2016, 386, 65-71.

[99] LAZZINI, G., L. GEMINI, A. LUTEY, R. KLING, et al. Surface Morphologies in Ultra-short Pulsed Laser Processing of Stainless-Steel at High Repetition Rate. International Journal of Precision Engineering and Manufacturing, 2019, 1-10.

[100] VOISIAT, B., M. GEDVILAS, S. INDRIŠIŪNAS AND G. RAČIUKAITIS Picosecond-laser 4-beam-interference ablation as a flexible tool for thin film microstructuring. Physics Procedia, 2011, 12, 116-124.

[101] LASAGNI, A., T. ROCH, J. BERGER, T. KUNZE, et al. To use or not to use (direct laser interference patterning), that is the question. In *Laser-based Micro-and Nanoprocessing IX.* International Society for Optics and Photonics, 2015, vol. 9351, p. 935115.

[102] LANG, V., T. ROCH AND A. F. LASAGNI. World record in high speed laser surface microstructuring of polymer and steel using direct laser interference patterning. In *Laser-based Micro-and Nanoprocessing X.* International Society for Optics and Photonics, 2016, vol. 9736, p. 97360Z.

[103] KUANG, Z., W. PERRIE, J. LEACH, M. SHARP, et al. High throughput diffractive multi-beam femtosecond laser processing using a spatial light modulator. Applied surface science, 2008, 255(5), 2284-2289.

[104] TORRES-PEIRÓ, S., J. GONZÁLEZ-AUSEJO, O. MENDOZA-YERO, G. MÍNGUEZ-VEGA, et al. Parallel laser micromachining based on diffractive optical elements with dispersion compensated femtosecond pulses. Optics express, 2013, 21(26), 31830-31836.

[105] LOESCHNER, U., J. SCHILLE, A. STREEK, T. KNEBEL, et al. High-rate laser microprocessing using a polygon scanner system. J. Laser Appl, 2015, 27, S29303.

[106] DE LOOR, R., L. PENNING AND R. SLAGLE Polygon Laser Scanning: A need for speed in laser processing and micromachining. Laser Technik Journal, 2014, 11(3), 32-34.

[107] VALLE, J., S. BURGUI, D. LANGHEINRICH, C. GIL, et al. Evaluation of Surface Microtopography Engineered by Direct Laser Interference for Bacterial Anti-Biofouling. Macromolecular bioscience, 2015, 15(8), 1060-1069.

[108] LASAGNI, A. F., D. F. ACEVEDO, C. A. BARBERO AND F. MÜCKLICH One-Step Production of Organized Surface Architectures on Polymeric Materials by Direct Laser Interference Patterning. Advanced Engineering Materials, 2007, 9(1-2), 99-103.

[109] ROESSLER, F. AND A. F. LASAGNI Protecting Sub-Micrometer Surface Features in Polymers from Mechanical Damage Using Hierarchical Patterns. Journal of Laser Micro Nanoengineering, 2018, 13(2).

[110] BURNS, M. M., J.-M. FOURNIER AND J. A. GOLOVCHENKO Optical matter: crystallization and binding in intense optical fields. Science, 1990, 249(4970), 749-754.

[111] MISAWA, H. AND S. JUODKAZIS *3D laser microfabrication: principles and applications*. Edtion ed.: John Wiley & Sons, 2006. ISBN 3527608400.

[112] HECHT, E. Optics (Addision Wesley, San Francisco). Chap, 2002, 10, 500.

[113] MALÝ, P. *Optika*. Edtion ed.: Karolinum, 2013. ISBN 8024622467.

[114] MAZNEV, A., T. CRIMMINS AND K. NELSON How to make femtosecond pulses overlap. Optics letters, 1998, 23(17), 1378-1380.

[115] WANG, D., Z. WANG, Z. ZHANG, Y. YUE, et al. Direct modification of silicon surface by nanosecond laser interference lithography. Applied surface science, 2013, 282, 67-72.

[116] JOCHCOVA, D., KAUFMAN, J., HAUSCHWITZ, P., et. al. Intensity distribution modulation of multiple beam interference pattern. MM Science Journal. 2019, 2019(05), 3652-3656.

[117] ALAMRI, S. AND A. F. LASAGNI Development of a general model for direct laser interference patterning of polymers. Optics express, 2017, 25(9), 9603-9616.

[118] LASAGNI, A. F., D. YUAN, P. SHAO AND S. DAS Periodic Micropatterning of Polyethylene Glycol Diacrylate Hydrogel by Laser Interference Lithography Using Nano-and Femtosecond Pulsed Lasers. Advanced Engineering Materials, 2009, 11(3), B20-B24.

[119] ZHOU, Q., W. YANG, F. HE, R. STOIAN, et al. Femtosecond multi-beam interference lithography based on dynamic wavefront engineering. Optics express, 2013, 21(8), 9851-9861.

[120] HAUPT, O., V. SCHÜTZ AND U. STUTE. Multi-spot laser processing of crystalline solar cells. In *Laser-based Micro-and Nanopackaging and Assembly V.* International Society for Optics and Photonics, 2011, vol. 7921, p. 79210V.

[121] KATZ, S., N. KAPLAN AND I. GROSSINGER Using Diffractive Optical Elements: DOEs for beam shaping–fundamentals and applications. Optik & Photonik, 2018, 13(4), 83-86.

[122] ŠKEREŇ, M., I. RICHTER AND P. FIALA Iterative Fourier transform algorithm: comparison of various approaches. Journal of Modern Optics, 2002, 49(11), 1851-1870.

[123] NIKOLENKO, V., D. S. PETERKA, R. ARAYA, A. WOODRUFF, et al. Spatial light modulator microscopy. Cold Spring Harbor protocols, 2013, 2013(12), pdb. top079517.

[124] KUANG, Z., W. PERRIE, D. LIU, S. EDWARDSON, et al. Diffractive multi-beam surface micro-processing using 10 ps laser pulses. Applied surface science, 2009, 255(22), 9040-9044.

[125] KUANG, Z., D. LIU, W. PERRIE, S. EDWARDSON, et al. Fast parallel diffractive multi-beam femtosecond laser surface micro-structuring. Applied surface science, 2009, 255(13-14), 6582-6588.

[126] HAMAMATSU PHOTONICS, K. Opto-semiconductor handbook. Hamamatsu, Japan: Hamamatsu Photonics KK, Solid State Division, 2014.

[127] RIPOLL, O., V. KETTUNEN AND H. P. HERZIG Review of iterative Fourier-transform algorithms for beam shaping applications. Optical Engineering, 2004, 43(11), 2549-2549.

[128] KOVACHEV, M., R. ILIEVA, L. ONURAL, G. ESMER, et al. Reconstruction of computer generated holograms by spatial light modulators. In *International Workshop on Multimedia Content Representation, Classification and Security.* Springer, 2006, p. 706-713.

[129] ORTEGA, A. B., S. BUCIO-PACHECO, S. LOPEZ-HUIDOBRO, L. PEREZ-GARCIA, et al. Creation of optical speckle by randomizing a vortex-lattice. Optics express, 2019, 27(4), 4105-4115.

[130] MALAVALLI, A., M. ACKERMANN AND C. AEGERTER Structured illumination behind turbid media. Optics express, 2016, 24(20), 23018-23026.

[131] FORBES, A., A. DUDLEY AND M. MCLAREN Creation and detection of optical modes with spatial light modulators. Advances in Optics and Photonics, 2016, 8(2), 200-227.

8 Publications of the author related to the doctoral thesis

Articles in peer-reviewed journals

[A] JAGDHEESH, R., HAUSCHWITZ, P., J. MUŽÍK, et al. Non-fluorinated superhydrophobic Al7075 aerospace alloy by ps laser processing. Applied surface science, 2019, 493: 287-293.

[B] HAUSCHWITZ, P., R. JAGDHEESH, D. ROSTOHAR, et al. Nanostructure fabrication on the top of laser-made micropillars for enhancement of water repellence of aluminium alloy. Materials Letters, 2019, 256: 126601.

[C] HAUSCHWITZ, P., et al. Fabrication of functional superhydrophobic surfaces on carbon fibre reinforced plastics by IR and UV direct laser interference patterning. Applied Surface Science, 2019, 144817.

[D] HAUSCHWITZ, P., et al. Towards rapid large-scale LIPSS fabrication by 4-beam ps DLIP. Optics & Laser Technology, 133: 106532.

[E] HAUSCHWITZ, Petr, et al. Large-Beam Picosecond Interference Patterning of Metallic Substrates. Materials, 2020, 13.20: 4676.

[F] HAUSCHWITZ, Petr, et al. Micromachining of Invar with 784 Beams Using 1.3 ps Laser Source at 515 nm. Materials, 2020, 13.13: 2962.

[G] HAUSCHWITZ, P., et al. Hydrophilic to ultrahydrophobic transition of Al 7075 by affordable ns fiber laser and vacuum processing. Applied Surface Science, 2019, 144523.

[H] HAUSCHWITZ, P., et. al. Superhydrophobic staineless steel surface by two-step ns laser processing. MM Science Journal. 2019, 2019(05), 3647-3651

[I] JOCHCOVA, D., KAUFMAN, J., HAUSCHWITZ, P., et. al. Intensity distribution modulation of multiple beam interference pattern. MM Science Journal. 2019, 2019(05), 3652-3656

Conference presentations

[J] HAUSCHWITZ, et al., Laser processing of C-PPS and C-PEEK Carbon Fibre Reinforced Plastics, In: European congress and exhibition on advanced materials and processes; 2017 Sep 17-22; Thessaloniki, Greece.

[K] HAUSCHWITZ, et al., Hydrophilic to ultrahydrophobic transition of Al 7075 by affordable ns fiber laser and vacuum processing. In: International conference on applied surface sicence; 2019 June 17-20; Pisa, Italy.

[L] HAUSCHWITZ, et al., Two-step nanosecond laser processing for dual-scale micro-and nanostructure fabrication of superhydrophobic stainless steel surface. In: International Conference on Advanced Laser Technologies; 2019 Sep 15-20; Prague, Czech Republic